NASA-CR-194517

IN-32-CR

REPORT No. TRC-CAB-9308

P. 122

ANTENNA PATTERN CONTROL USING IMPEDANCE SURFACES

by

Constantine A. Balanis, Kefeng Liu and Panayiotis A. Tirkas

Final Report

September 16, 1990 – September 15, 1993

Prepared by

Telecommunications Research Center
College of Engineering and Applied Science
Arizona State University
Tempe, AZ 85287-7206

Sponsored by

Grant No. NAG-1-1183

Joint Research Program Office CECOM/NASA

National Aeronautics and Space Administration

Langley Research Center

Hampton, VA 23681-0001

(NASA-CR-194517) ANTENNA PATTERN
CONTROL USING IMPEDANCE SURFACES
Final Report, 16 Sep. 1990 - 15
Sep. 1993 (Arizona State Univ.)
122 p

N94-13799

Unclas

G3/32 0187794

REPORT No. TRC-CAB-9308

ANTENNA PATTERN CONTROL USING IMPEDANCE SURFACES

by

Constantine A. Balanis, Kefeng Liu and Panayiotis A. Tirkas

Final Report

September 16, 1990 – September 15, 1993

Prepared by
Telecommunications Research Center
Department of Electrical Engineering
Arizona State University
Tempe, Arizona 85287-7206

Sponsored by
Grant No. NAG-1-1183
Joint Research Program Office CECOM/NASA
National Aeronautics and Space Administration
Langley Research Center
Hampton, VA 23681-0001

ABSTRACT

During the period of this research project, a comprehensive study of pyramidal horn antennas was conducted. Full-wave analytical and numerical techniques have been developed to analyze horn antennas with or without impedance surfaces. Based on these full-wave analytic techniques, research was conducted on the use of impedance surfaces on the walls of the horn antennas to control the antenna radiation patterns without a substantial loss of antenna gain. It was found that the use of impedance surfaces could modify the antenna radiation patterns. In addition to the analytical and numerical models, experimental models were also constructed and they were used to validate the predictions. Excellent agreement between theoretical predictions and the measured data was obtained for pyramidal horns with perfectly conducting surfaces. Very good comparisons between numerical and experimental models were also obtained for horns with impedance surfaces.

TABLE OF CONTENTS

CHAPTER Page

APPENDIX

LIST OF TABLES

LIST OF FIGURES

Figure Page

Figure Page

CHAPTER 1

MOMENT METHOD ANALYSIS OF HORN ANTENNAS

1.1 Introduction

The horn antenna is the simplest and probably the most widely used microwave radiator. It is used as the feed for large reflectors and lens antennas in communication systems throughout the world. It is also a high gain element in phased arrays. Horn antennas are highly accurate radiating devices, and are often used as standard-gain devices for the calibration of other antennas. Applications of horn antennas have been explored for nearly a century. In addition, extensive investigations of horn antennas have been of increasing interest during the past three decades. Some of the early research papers on the horn antennas are well documented in Love's collection[1].

Besides being a high-gain and high-efficiency microwave antenna, the pyramidal horn exhibits some additional advantages. Its rectangular geometry is easy to construct, and hence the antenna is a low-cost device. The aperture size of the horn can be adjusted to achieve some specific beam characteristics with negligible changes in other properties. Furthermore, the pyramidal horn can easily be excited with conventional microwave circuit devices.

Analysis and design of the pyramidal horns was traditionally conducted using approximate aperture field distributions. Using this approach the contributions from induced currents on other parts of the horn surface are often assumed negligible. A quadratic phase term is usually assumed to account for the flaring of the horn transition [2, 3, 4]. This approximate method predicts fairly well the main-beam of the far-field radiation pattern and the gain of the antenna. Since reflections, mode couplings, and diffracted fields from the exterior surfaces are not included, the approximate aperture field method does not predict very well the sidelobes in the back region of the antenna.

In the 1960's, the Geometric Theory of Diffraction (GTD), a high-frequency method, was introduced to include edge diffracted fields. The two-dimensional GTD model presented in [5, 6] yielded an improvement in the far-field E-plane radiation pattern over the approximate aperture field method. A two-dimensional model for the E-plane pattern, was examined by Botha *et al.* in [7] using an integral equation and the Moment Method.

Although, the two-dimensional models perform well in the far-field E-plane pattern, they are not very accurate in predicting the H-plane pattern, especially in the back regions of the antenna because coupling of the diffracted fields from both the E- and H-plane edges is not included in the two-dimensional models. Finally, neither the approximate aperture field method nor GTD are well suited for calculating aperture field distribution, VSWR, and cross-polarized patterns.

Recent advances of the computational capabilities and the popularity of the pyramidal horn antennas have encouraged the development of more accurate models with improved numerical efficiencies. The integral equation formulation with a Moment Method (MM)[8] solution has become a powerful tool in modeling complex electromagnetic field problems. MM has been used to analyze an aperture on a ground plane [9, 10] and an aperture on a ground plane in the presence of a thin conducting plate[11]. In addition, the MM has been applied to pyramidal horn antennas, both with and without corrugations, mounted on a ground plane[12, 13]. The presence of a ground plane simplifies the MM analysis. However, in most applications, the horn antenna is a stand-alone radiating element and is not mounted on a ground plane. Without the presence of a ground plane, an electric current is induced on the outer surface of the horn. This current has a significant impact on the radiation pattern at wide angles and in the back region of the antenna.

Complete three-dimensional models have been developed for electrically small pyramidal horn antennas by using MM [14]. Electrically small H-plane sectoral horns and X-band standard-gain horns were also analyzed using the finite-difference time-domain method (FDTD) [15, 16]. High gain pyramidal horn antennas, are difficult to model accurately with simple extensions of existing numerical electromagnetic methods, such as those described in [14, 15, 16, 17]. To model the transition from a relatively small feeding aperture to a much larger radiating aperture, requires the use of a large number of elements. Also, the electric current density on the interior surfaces of the horn transition becomes too complex to be modeled effectively using these methods.

A full-wave stepped-waveguide model and an HFIE method to analyze both the interior flaring and the exterior current contributions was previously developed by Kühn *et al.* [18] for conical horns. Kühn's formulation is simplified due to the axial symmetry of conical horn antennas.

1.2 Analysis of Horn Antennas

This part of the report presents numerical analysis methods for horn antennas with perfectly conducting walls. An integral equation method is first presented and then applied to two-dimensional models. Then a pyramidal horn antenna mounted on an infinite ground plane is examined. This type of horn antenna mounting is often used on the surface of an aircraft or space-craft. Finally, pyramidal horn antennas radiating in free-space is examined using a three-dimensional full wave formulation.

The three-dimensional, full-wave formulation provides flexibility and includes all of the important details of a practical pyramidal horn antenna. It represents the first full-wave method to include the current densities on all the conducting surfaces of the pyramidal horn. These are necessary to obtain the fine pattern structure in the regions of low-level radiation. Based on this work, a paper was submitted and accepted for publication in the *IEEE Transactions on Antennas and Propagation* [19].

1.2.1 Two-dimensional Horn Models

A. E-plane Pattern

Botha *et al.* utilized the two-dimensional TE polarized radiation and scattering code by Richmond [20] to analyze the E-plane radiation pattern of a profiled horn [7]. The two-dimensional model can be used to simulate the principal E-plane radiation patterns of pyramidal horns.

Fig. 1.1 demonstrates the E-plane geometry of a pyramidal horn. The position of the magnetic line source d is chosen a multiple of $\frac{\lambda_g}{2}$ to achieve best robustness of the Moment Method solution. For the two-dimensional radiation problem with TE polarization, the integral equation method, such as in [20], can be applied. However, a more simplified technique [21, 22] published by the authors of this report, presents a better alternative for this problem. In this simplified TE-polarized field formulation, pulse expansion and point matching were introduced. Analytical evaluation of diagonal elements of the impedance matrix was developed.

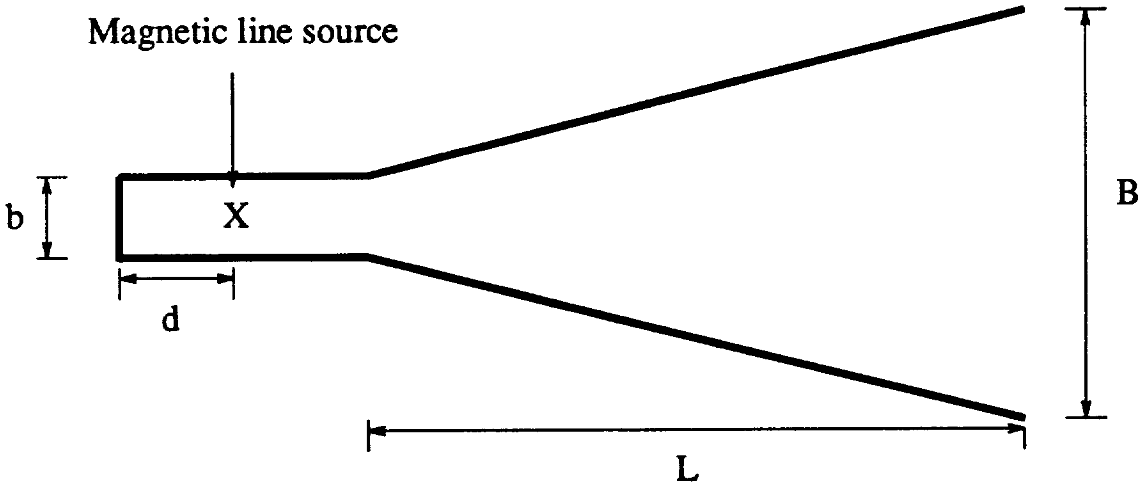

Fig. 1.1: E-plane geometry of a pyramidal horn antenna.

Figs. 1.2 and 1.3 compare the normalized E-plane radiation patterns between the two-dimensional model and the full three-dimensional model, of 10-dB and 20-dB X-band standard gain horns, respectively. As shown in the figures, the prediction of the

E-plane radiation pattern based on the two-dimensional model provides reasonable accuracy in the main beam. The agreement is better for the 20-dB standard gain horn because the two-dimensional model approximates a larger horn better than a smaller one.

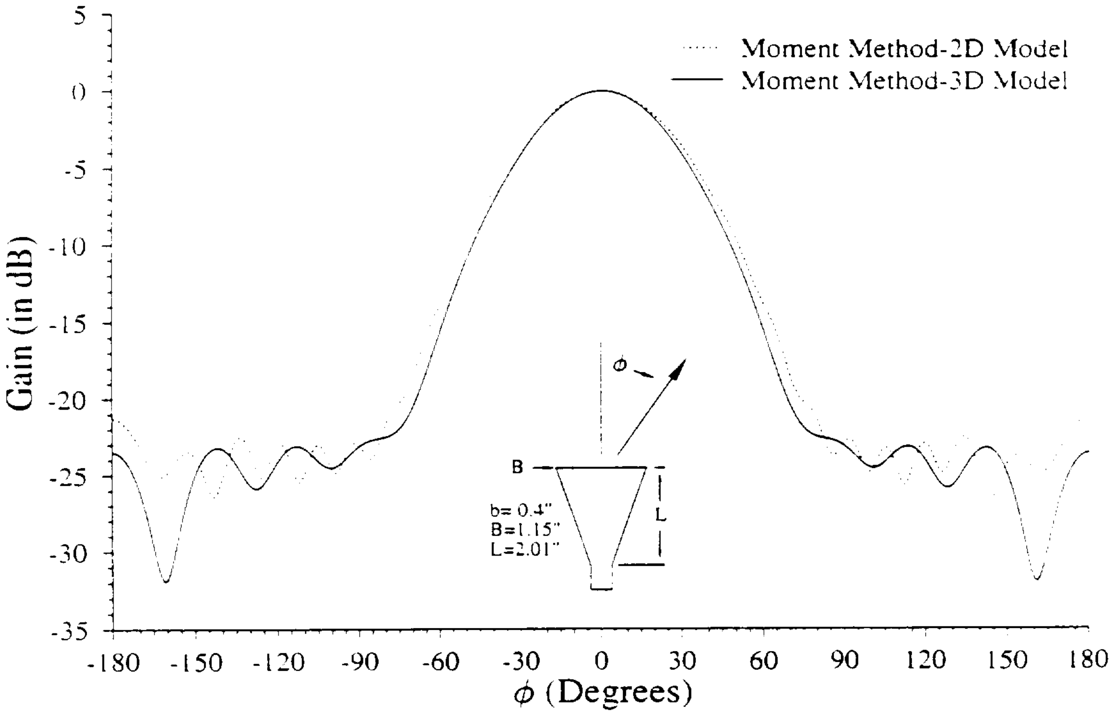

Fig. 1.2: Normalized E-plane patterns of a 10-dB X-Band gain horn.

B. H-plane Pattern

The H-plane geometry of a pyramidal horn is shown in Fig. 1.4. The position of the electric line source d was chosen to be a multiple of $\frac{\lambda_g}{4}$ to achieve best robustness of the Moment Method solution. This two-dimensional model was analyzed using integral equation formulation with TM-polarization. The simple technique outlined by Harrington [8] was introduced to predict the radiation pattern.

Figs. 1.5 and 1.6 compare the normalized H-plane radiation patterns between the two-dimensional model and the full three-dimensional model, of 10-dB and 20-dB X-band standard gain horns, respectively. Predictions of the H-plane radiation pattern

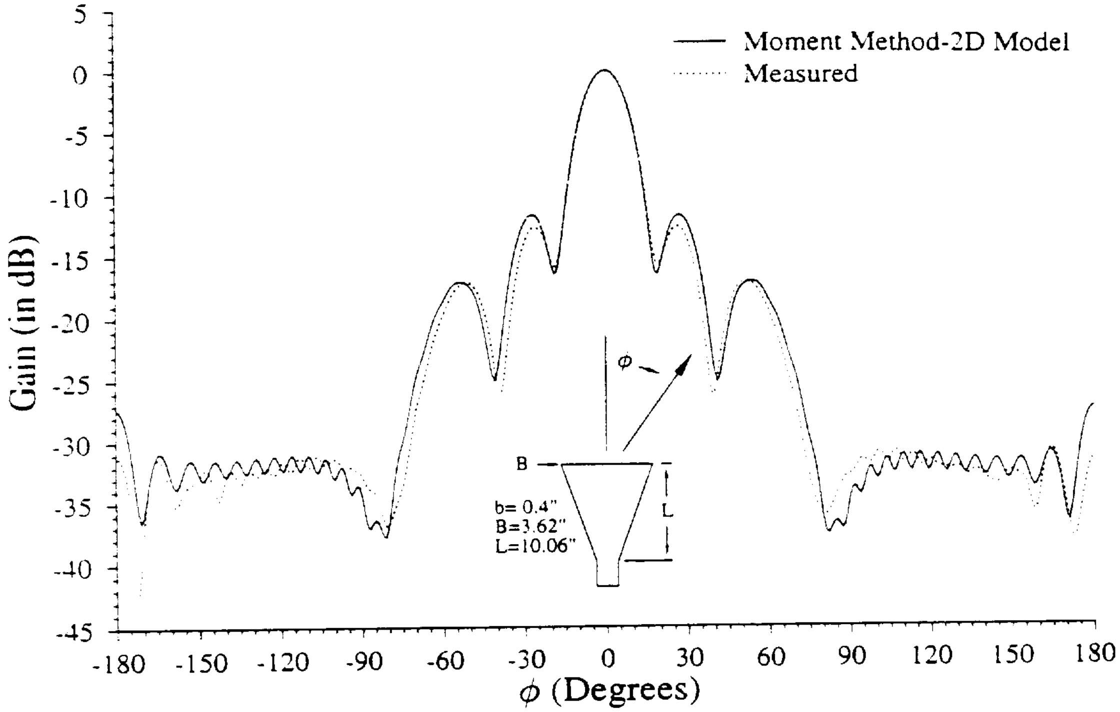

Fig. 1.3: Normalized E-plane patterns of a 20-dB X-Band gain horn.

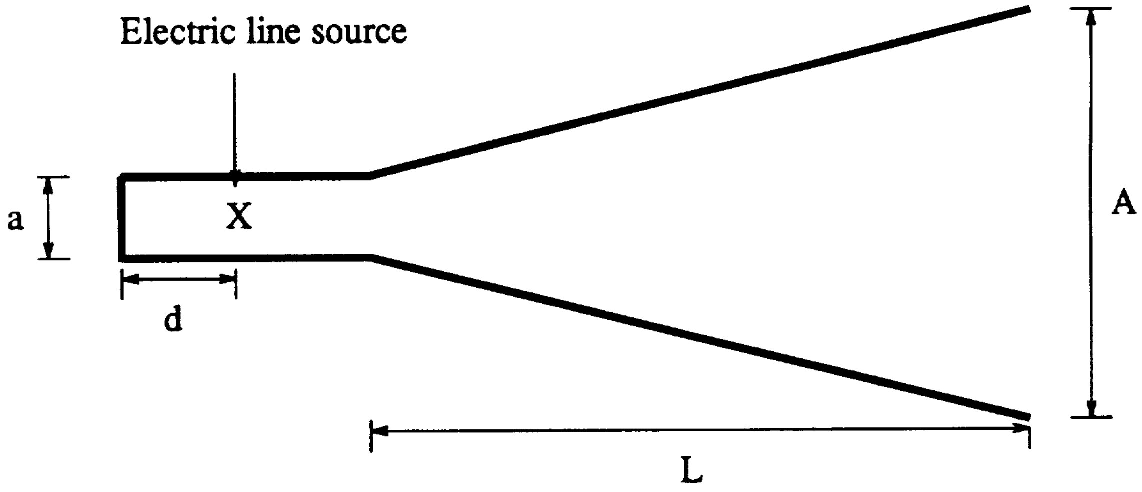

Fig. 1.4: H-plane geometry of a pyramidal horn antenna.

based on the two-dimensional model provide reasonable accuracy in the main beam, especially for the 20-dB standard gain horn. Since the coupling of diffracted fields from the E-plane edges are not included in this two-dimensional model, the H-plane patterns in the back regions were not predicted accurately.

The advantage of the two-dimensional models is their analytical simplicity. The two-dimensional models predict the main beam of the radiation patterns very effectively. The computer code for the two-dimensional models can be executed on a personal computer with a quick turn-around time. One of the limitations of the two-dimensional models is their inability to analyze the field coupling between two different principal planes. Therefore, back lobes are not predicted very accurately. Finally, the two-dimensional models can not be used to predict aperture distribution, VSWR, gain, and cross-polarized patterns.

1.2.2 Pyramidal Horn Mounted on a Ground Plane

Fig. 1.7 illustrates the geometry of a pyramidal horn antenna mounted on a ground plane. This problem can be separated into two parts. The first part includes the transition from the feeding waveguide to the radiating aperture. A complete full-wave approach is applied to represent this transition as a series of stepped-waveguide sections. This was done as shown in Fig. 1.8. Mode matching was performed by rigorously enforcing the boundary conditions at each step. The result is a scattering matrix for each step, which can be combined to obtain the scattering matrix for the entire transition region.

The second part is the radiating aperture in the presence of an infinite ground plane. The equivalence principle was introduced to formulate the magnetic field integral equation on the radiating aperture which combines the interior field transition problem with the exterior radiation.

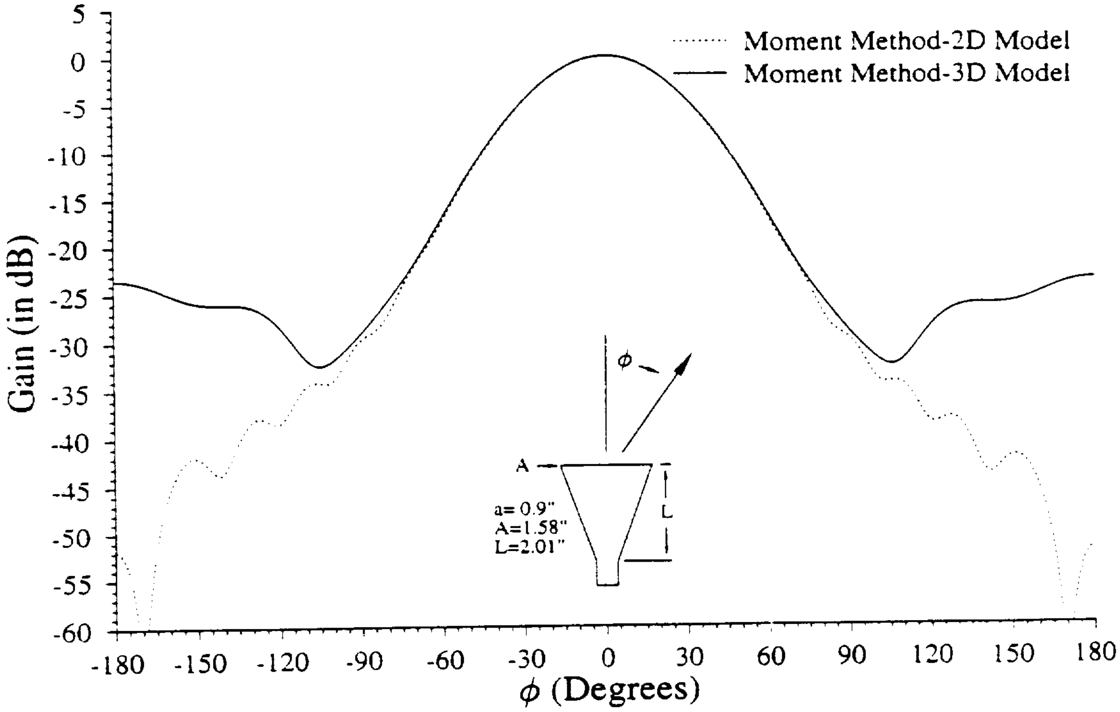

Fig. 1.5: Normalized H-plane patterns of a 10-dB X-Band gain horn at 10 GHz.

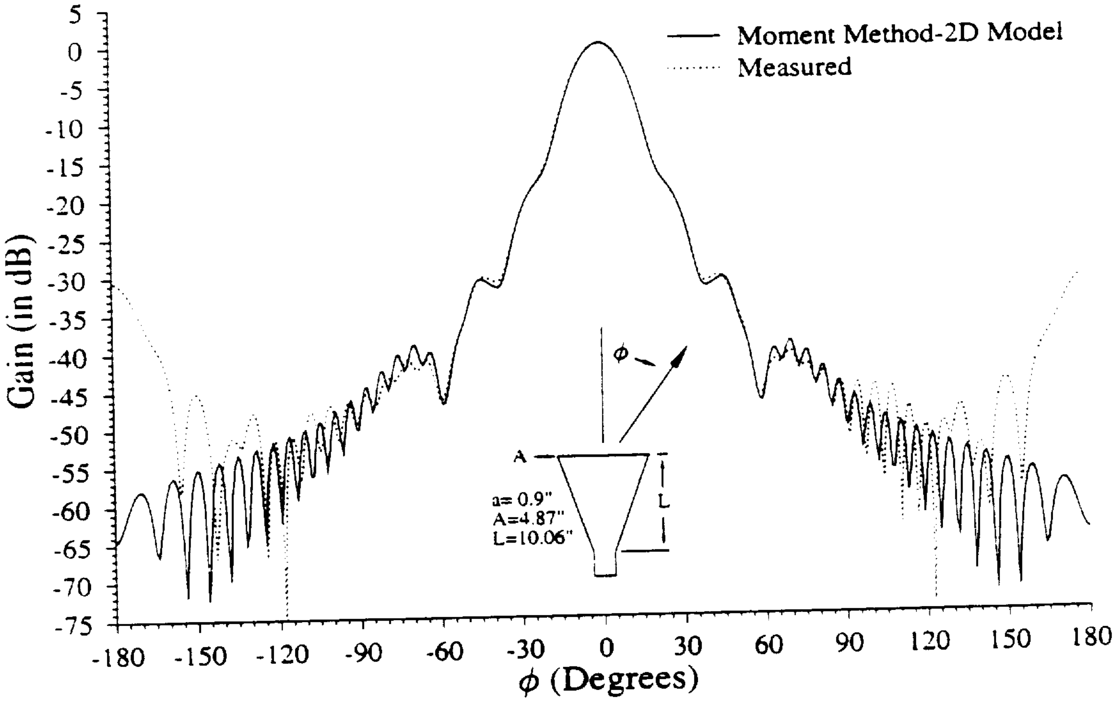

Fig. 1.6: Normalized H-plane patterns of a 20-dB X-Band gain horn at 10 GHz.

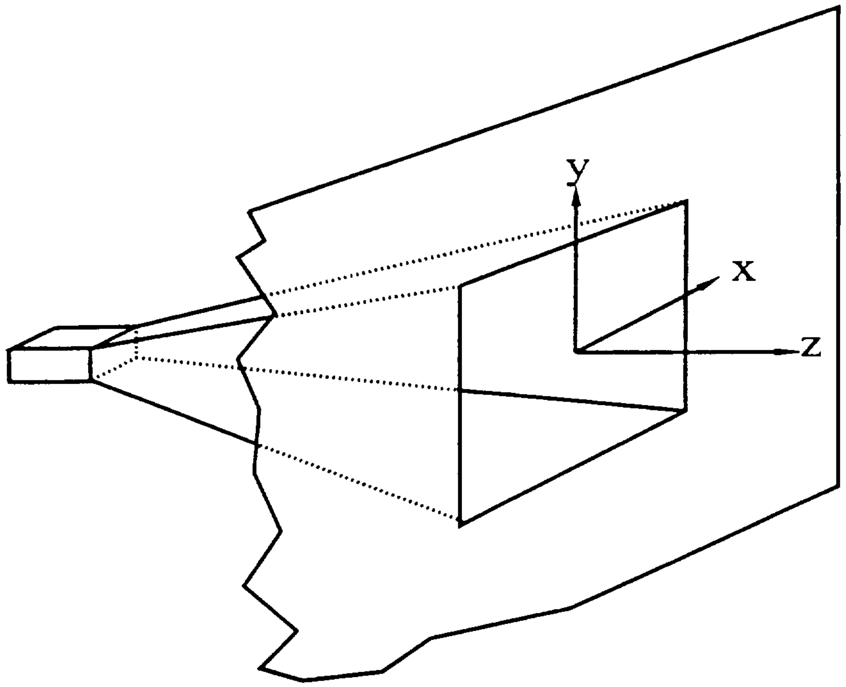

Fig. 1.7: Pyramidal horn mounted on a ground plane.

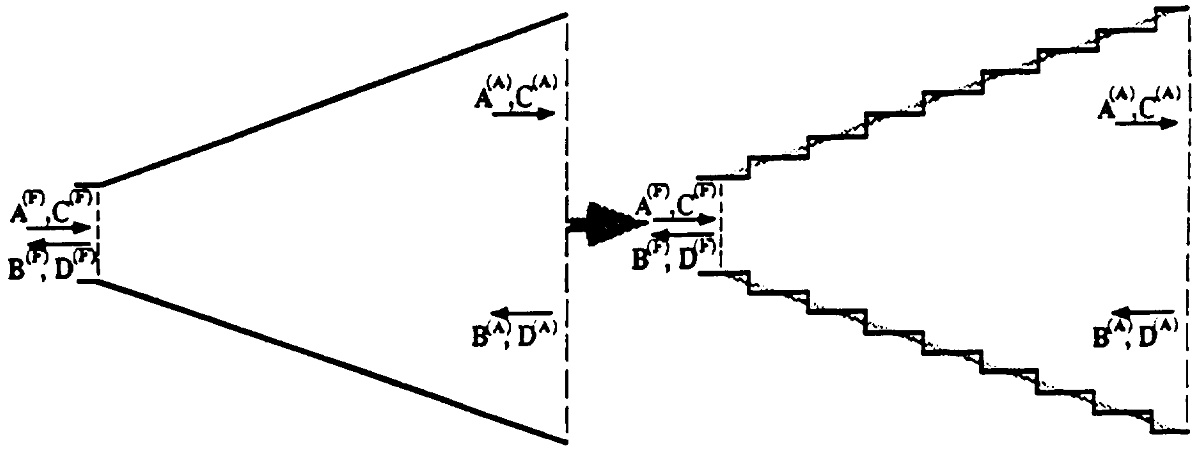

Fig. 1.8: Stepped waveguide model of the horn transition.

A. Interior Horn Transitions

Accurate analysis of waveguide transitions has been an interesting research topic in microwave circuit design [23, 24, 25, 26]. The available numerical approaches can be divided into two classes. First is a numerical solution of a system of ordinary differential equations [24, 27], and second is the stepped waveguide model with a full-wave mode-matching technique on the stepped junctions [13, 18, 23, 27]. With the first class, the numerical solution of the differential equations must be performed with a finite advancing step size. However, due to the numerical problem caused by evanescent modes, the taper has to be divided into several sections. The hybrid matrix of each section needs to be computed separately, then translated and combined into a scattering matrix.

On the other hand, the stepped-waveguide technique uses a finite number of subdivisions of waveguide steps to approach the continuous horn taper. Within each waveguide step, the waveguide section is uniform. The scattering matrices of each waveguide step are related to each other by the electromagnetic boundary conditions on the discontinuous junctions connecting them. The combination of the scattering matrices of all the steps gives the total scattering matrix of the horn transition.

As examined by [25] and [27], the numerical technique in solving the first-order differential equation yields results with the same accuracy as given by the stepped-waveguide technique, when the size of the steps is sufficiently small. The validity of the stepped-waveguide approximation to simulate the continuous horn transition has been justified in [12, 13, 18, 23, 27]. The computational effort for the two approaches is about the same.

The stepped waveguide technique was employed in this project because of its advantage in numerical stability. Fig. 1.8 represents a typical stepped waveguide model of the horn transition. The continuous transition is approximated by a number of cascaded stepped-waveguides. For the pyramidal horn transition, each step is a section of rectangular waveguide. Electromagnetic field distributions in each of the rectangular sections were expressed as the superposition of all possible TM_z and TE_z modes. Moreover, the TM_z and TE_z modes in each region were generated by the z components of two vector potentials[22]

$$F_z = \epsilon \sum_{\substack{m=1,M \\ n=0,N}} (A_{mn}e^{-j\beta_z z} + B_{mn}e^{j\beta_z z})e_{mn}(x,y) \tag{1.1}$$

$$A_z = \sqrt{\mu\epsilon} \sum_{\substack{m=1,M \\ n=2,N}} (C_{mn}e^{-j\beta_z z} - D_{mn}e^{j\beta_z z})h_{mn}(x,y) \tag{1.2}$$

$$e_{mn}(x,y) = \frac{2\cos(\beta_x x)\cos(\beta_y y)}{\beta_c\sqrt{ab(1+\delta_{no})}} \quad ; \quad h_{mn}(x,y) = \frac{2\sin(\beta_x x)\sin(\beta_y y)}{\beta_c\sqrt{ab}}$$

$$\beta_x = \frac{m\pi}{a};\ \beta_y = \frac{n\pi}{b};\ \beta_c = \sqrt{\beta_x^2+\beta_y^2} \quad ; \quad \beta_c^2+\beta_z^2 = \omega^2\mu\epsilon;\ \delta_{no} = \begin{cases} 1 & \text{if n=0} \\ 0 & \text{otherwise} \end{cases}$$

Then the transverse electric and magnetic fields due to the two vector potentials were evaluated by the following equations [22]:

$$E_x = -\frac{1}{\epsilon}\frac{\partial F_z}{\partial y} - j\frac{1}{\omega\mu\epsilon}\frac{\partial^2 A_z}{\partial x\partial z} \tag{1.3}$$

$$E_y = \frac{1}{\epsilon}\frac{\partial F_z}{\partial x} - j\frac{1}{\omega\mu\epsilon}\frac{\partial^2 A_z}{\partial y\partial z} \tag{1.4}$$

$$H_x = -j\frac{1}{\omega\mu\epsilon}\frac{\partial^2 F_z}{\partial x\partial z} + \frac{1}{\mu}\frac{\partial A_z}{\partial y} \tag{1.5}$$

$$H_y = -j\frac{1}{\omega\mu\epsilon}\frac{\partial^2 F_z}{\partial y\partial z} - \frac{1}{\mu}\frac{\partial A_z}{\partial x} \tag{1.6}$$

At each stepped waveguide junction of Fig. 1.8, the boundary conditions relating the two slightly different-sized waveguides are

$$E_{x,y}^{(1)}(x,y)|_{\text{on } S} = E_{x,y}^{(2)}(x,y)|_{\text{on } S} \tag{1.7}$$

$$E^{(2)}_{x,y}(x,y)|_{\text{on }\Delta S} = 0 \tag{1.8}$$

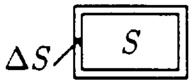

$$H^{(1)}_{x,y}(x,y)|_{\text{on }S} = H^{(2)}_{x,y}(x,y)|_{\text{on }S} \tag{1.9}$$

where S is the area of the smaller waveguide section, and ΔS is the "ring" area of the larger waveguide section.

Testing the boundary conditions in (1.7)-(1.9) by the corresponding expansion functions (this process is equivalent to a full-domain Galerkin's Method), uniquely defines the relation between the full-wave expansion coefficients on both sides of the junction. After some straight forward mathematical manipulations, the resulting transition equations for the full-wave expansion coefficients of TM_z and TE_z are given by

$$A^{(2)}_{mn} + B^{(2)}_{mn} = \sum_{kl} \frac{\beta_c^{(1)}\beta_x^{(2)}}{\beta_c^{(2)}\beta_x^{(1)}} U_{mnkl}(A^{(1)}_{kl} + B^{(1)}_{kl}) \tag{1.10}$$

$$\begin{aligned} C^{(2)}_{mn} + D^{(2)}_{mn} &= \sum_{kl} \frac{\beta_o[(\beta_x^{(1)}\beta_y^{(2)})^2 - (\beta_x^{(2)}\beta_y^{(1)})^2)]}{\beta_z^{(2)}\beta_x^{(1)}\beta_y^{(2)}\beta_c^{(2)}\beta_c^{(1)}} U_{mnkl}(A^{(1)}_{kl} + B^{(1)}_{kl}) \\ &+ \sum_{kl} \frac{\beta_x^{(1)}\beta_c^{(2)}\beta_z^{(1)}}{\beta_x^{(2)}\beta_c^{(1)}\beta_z^{(2)}} V_{mnkl}(C^{(1)}_{kl} + D^{(1)}_{kl}) \end{aligned} \tag{1.11}$$

$$\begin{aligned} A^{(1)}_{kl} - B^{(1)}_{kl} &= \sum_{mn} \frac{\beta_z^{(2)}\beta_c^{(1)}\beta_x^{(2)}}{\beta_z^{(1)}\beta_c^{(2)}\beta_x^{(1)}} U_{mnkl}(A^{(2)}_{mn} - B^{(2)}_{mn}) \\ &+ \sum_{mn} \frac{\beta_o[(\beta_x^{(1)}\beta_y^{(2)})^2 - (\beta_x^{(2)}\beta_y^{(1)})^2)]}{\beta_z^{(1)}\beta_x^{(1)}\beta_y^{(2)}\beta_c^{(2)}\beta_c^{(1)}} U_{mnkl}(C^{(2)}_{mn} - D^{(2)}_{mn}) \end{aligned} \tag{1.12}$$

$$C^{(1)}_{kl} - D^{(1)}_{kl} = \sum_{mn} \frac{\beta_x^{(1)}\beta_c^{(2)}}{\beta_x^{(2)}\beta_c^{(1)}} V_{mnkl}(C^{(2)}_{mn} - D^{(2)}_{mn}) \tag{1.13}$$

where

$$U_{mnkl} = \frac{4\int_0^{a_1}\int_0^{b_1} \sin(\beta_x^{(2)}x')\sin(\beta_x^{(1)}x)\cos(\beta_y^{(2)}y')\cos(\beta_y^{(1)}y)dxdy}{\sqrt{a_1a_2b_1b_2(1+\delta_{no})(1+\delta_{lo})}} \tag{1.14}$$

$$V_{mnkl} = \frac{4\int_0^{a_1}\int_0^{b_1} \cos(\beta_x^{(2)}x')\cos(\beta_x^{(1)}x)\sin(\beta_y^{(2)}y')\sin(\beta_y^{(1)}y)dxdy}{\sqrt{a_1a_2b_1b_2}} \tag{1.15}$$

$$x' = x + \frac{\Delta a}{2} = x + \frac{a_2 - a_1}{2} \tag{1.16}$$

$$y' = y + \frac{\Delta b}{2} = y + \frac{b_2 - b_1}{2} \tag{1.17}$$

The integrals in U_{mnkl} and U_{mnkl} were evaluated analytically and reduced to

$$U_{mnkl} = \frac{4[1+(-1)^{m+k}][1+(-1)^{n+l}]}{\sqrt{a_1a_2b_1b_2(1+\delta_{no})(1+\delta_{lo})}} \frac{\beta_x^{(1)}\sin(\beta_x^{(2)}\frac{\Delta a}{2})}{{\beta_x^{(1)}}^2 - {\beta_x^{(2)}}^2} \frac{\beta_y^{(2)}\sin(\beta_y^{(2)}\frac{\Delta b}{2})}{{\beta_y^{(1)}}^2 - {\beta_y^{(2)}}^2} \tag{1.18}$$

$$V_{mnkl} = \frac{\beta_x^{(2)}\beta_y^{(1)}}{\beta_x^{(1)}\beta_y^{(2)}} U_{mnkl} \tag{1.19}$$

To express (1.10)-(1.13) in matrix form, let

$$a^{(1)} = \begin{pmatrix} A_{kl}^{(1)} \\ C_{kl}^{(1)} \end{pmatrix} \qquad b^{(1)} = \begin{pmatrix} B_{kl}^{(1)} \\ D_{kl}^{(1)} \end{pmatrix} \tag{1.20}$$

$$a^{(2)} = \begin{pmatrix} A_{mn}^{(2)} \\ C_{mn}^{(2)} \end{pmatrix} \qquad b^{(2)} = \begin{pmatrix} B_{mn}^{(2)} \\ D_{mn}^{(2)} \end{pmatrix} \tag{1.21}$$

Then, the matrix equations of (1.11)-(1.13) are

$$a^{(2)} + b^{(2)} = Y(a^{(1)} + b^{(1)}) \tag{1.22}$$

$$a^{(1)} - b^{(1)} = Z(a^{(2)} - b^{(2)}) \tag{1.23}$$

where Y is a matrix with corresponding elements defined by (1.10) and (1.11), and Z by (1.12) and (1.13), respectively. With a simple mathematical manipulation of the two matrix equations, the scattering matrix of the stepped-waveguide junction can be obtained in the form

$$\begin{pmatrix} b^{(1)} \\ a^{(2)} \end{pmatrix} = \begin{pmatrix} (I+ZY)^{-1}(I-ZY) & 2(I+ZY)^{-1}Z \\ 2(I+YZ)^{-1}Y & (I+YZ)^{-1}(YZ-I) \end{pmatrix} \begin{pmatrix} a^{(1)} \\ b^{(2)} \end{pmatrix} \quad (1.24)$$

The next step is to combine the scattering matrices of the stepped-waveguide sections. Consider two series stepped-waveguides each having the scattering matrix of the form

$$\begin{pmatrix} b^{(i)} \\ a^{(i+1)} \end{pmatrix} = \begin{pmatrix} S_{11}^{(i)} & S_{12}^{(i)} \\ S_{21}^{(i)} & S_{22}^{(i)} \end{pmatrix} \begin{pmatrix} a^{(i)} \\ b^{(i+1)} \end{pmatrix} \quad (1.25)$$

$$\begin{pmatrix} b^{(i+1)} \\ a^{(i+2)} \end{pmatrix} = \begin{pmatrix} S_{11}^{(i+1)} & S_{12}^{(i+1)} \\ S_{21}^{(i+1)} & S_{22}^{(i+1)} \end{pmatrix} \begin{pmatrix} a^{(i+1)} \\ b^{(i+2)} \end{pmatrix} \quad (1.26)$$

where the scattering matrices in the i-th and (i+1)-th section of stepped-waveguides are given by the combination of their junction scattering matrices and the corresponding propagation matrices due to the lengths of the waveguide section. These can be expressed as

$$S_{11}^{(\nu)} = [I + Z^{(\nu)}Y^{(\nu)}]^{-1}[I - Z^{(\nu)}Y^{(\nu)}] \quad (1.27)$$

$$S_{12}^{(\nu)} = 2[I + Z^{(\nu)}Y^{(\nu)}]^{-1}Z^{(\nu)}D^{(\nu)} \quad (1.28)$$

$$S_{21}^{(\nu)} = 2D^{(\nu)}[I + Y^{(\nu)}Z^{(\nu)}]^{-1}Y^{(\nu)} \quad (1.29)$$

$$S_{22}^{(\nu)} = D^{(\nu)}[I + Y^{(\nu)}Z^{(\nu)}]^{-1}[Y^{(\nu)}Z^{(\nu)} - I]D^{(\nu)} \quad (1.30)$$

where the propagation matrix $D^{(\nu)}$ is a diagonal matrix expressing the phase delay or magnitude attenuation of all possible positively going modes in the full-wave expansion of the ν-th (i-th or (i+1)-th) section of the waveguide which has a length of $d^{(\nu)}$. The element of $D^{(\nu)}$ is given by

$$D_{kk}^{(\nu)} = e^{-j\beta_k^{(\nu)} d^{(\nu)}} \tag{1.31}$$

Using (1.25) and (1.26), one can expand the two scattering matrices and obtain the combined scattering matrix of

$$\begin{pmatrix} b^{(i)} \\ a^{(i+2)} \end{pmatrix} = \begin{pmatrix} S_{11}^{(comb)} & S_{12}^{(comb)} \\ S_{21}^{(comb)} & S_{22}^{(comb)} \end{pmatrix} \begin{pmatrix} a^{(i)} \\ b^{(i+2)} \end{pmatrix} \tag{1.32}$$

where

$$S_{11}^{(comb)} = S_{11}^{(i)} + S_{12}^{(i)} F S_{11}^{(i+1)} S_{21}^{(i)} \tag{1.33}$$

$$S_{12}^{(comb)} = S_{12}^{(i)} F S_{12}^{(i+1)} \tag{1.34}$$

$$S_{21}^{(comb)} = S_{21}^{(i+1)} G S_{21}^{(i)} \tag{1.35}$$

$$S_{22}^{(comb)} = S_{22}^{(i+1)} + S_{21}^{(i+1)} G S_{22}^{(i)} S_{12}^{(i+1)} \tag{1.36}$$

with

$$F = [I - S_{11}^{(i+1)} S_{22}^{(i)}]^{-1} \tag{1.37}$$

$$G = [I - S_{22}^{(i)} S_{11}^{(i+1)}]^{-1} \tag{1.38}$$

Finally, if all incident full-wave modes are represented by a vector **a**, and the reflected full-wave modes by a vector **b**, the total scattering matrix for the horn transition relates the two by

$$\begin{pmatrix} \mathbf{b}^{(F)} \\ \mathbf{a}^{(A)} \end{pmatrix} = \begin{pmatrix} \mathbf{S}_{11}^{(T)} & \mathbf{S}_{12}^{(T)} \\ \mathbf{S}_{21}^{(T)} & \mathbf{S}_{22}^{(T)} \end{pmatrix} \begin{pmatrix} \mathbf{a}^{(F)} \\ \mathbf{b}^{(A)} \end{pmatrix} \tag{1.39}$$

where superscripts '(F)' and '(A)' denote, respectively, the full-wave coefficients at the feed junction and radiating aperture, and the superscript '(T)' denotes the total contribution of the horn transition. Although pyramidal horns are generally excited by the dominant TE_{10} mode from the feeding waveguide, higher order TE_{mn} and TM_{mn} modes are generated in the transition. For horn geometries with symmetrical flaring in both dimensions, only those modes which have $m = 1, 3, 5, 7, ..., M$ and $n = 0, 2, 4, 6, ..., N$ ($n = 0$ for TE modes only) are generated in the transition. The coupling between TE_{mn} and TM_{mn} modes is automatically included in the full-wave analysis of the stepped junctions.

There are two factors which affect the accuracy of the stepped-waveguide approximation. First is the size of the steps and second is the number of terms in the series (M and N in (1.1)-(1.2)). Past experience demonstrated that convergence is achieved by limiting the maximum size of the steps to $\lambda/32$. The choice of M and N should be based on the flare angle and length of steps. For horn antennas mounted on a ground plane, the choice of M and N is less critical. A choice of $M = 5$ and $N = 4$ is sufficient to predict accurately both the antenna patterns and the aperture field distributions.

B. Integral Equations

The radiation from the aperture into the half-space can be analyzed using an integral equation formulation and a Moment Method solution [8, 22]. Since the aperture is mounted on an infinite ground plane, only a magnetic field integral equation equation is needed to solve the aperture discontinuity. This equation is

$$2\mathbf{H}^{ext}_{tan}(\mathbf{M}) = \mathbf{H}^{int}_{tan}(\mathbf{a}^{(A)}, \mathbf{b}^{(A)}) \qquad \text{on the aperture} \tag{1.40}$$

where field components with 'ext' denote the fields on the half-space side of the aperture, and 'int' the fields on the horn side of the aperture. The equivalent magnetic current density is given by

$$\mathbf{M}(\mathbf{a}^{(A)} + \mathbf{b}^{(A)}) = -\mathbf{n} \times \mathbf{E}^{int}(\mathbf{a}^{(A)}, \mathbf{b}^{(A)}) \tag{1.41}$$

where $\mathbf{n}$ is the unit vector normal to the aperture, and $\mathbf{E}^{int}(\mathbf{a}^{(A)}, \mathbf{b}^{(A)})$ is the electric field internal to the aperture. The Moment Method solution of the integral equation is a simplified procedure from the field problem of a pyramidal horn antenna in free space presented in the next section.

Recently, a technique was introduced by Williams *et al.* [28] to simulate experimentally radiation of an antenna on an infinite ground plane using available measurements from the same antenna mounted on a finite-size ground plane. The foundation of the technique presented by Williams *et al.* is based on the fact that the scattered electromagnetic fields on the front and back sides of an electrically thin ground plane are symmetric. The measured radiation pattern in the back-side of the finite-size ground plane is used to correct the front-side of the radiation patterns by subtracting off the diffracted fields. Therefore, the corrected front-side radiation patterns represent the radiation patterns of the antenna mounted on an infinite ground plane.

This "subtraction" technique was applied in this project to convert measured radiation patterns of a pyramidal horn mounted on a finite-size ground plane to corresponding radiation patterns of a pyramidal horn mounted on an infinite ground plane. The radiation patterns for the latter case was computed numerically and compared with the corrected experimental measurements. For our experiment, a 20-dB standard gain horn antenna (A = 4.87″, B = 3.62″, L = 10.06″, a = 0.9″ and b = 0.4″) was mounted on a 3 × 3 feet planar aluminum sheet ground plane.

Figs. 1.9 and 1.10 compare the measured and computed E- and H-plane radiation patterns of the 20-dB standard gain horn mounted on an infinite ground plane. The measured padiation patterns from a 3 × 3 finite-size ground plane were corrected in Figs. 1.9 and 1.10 to correspond to the infinite ground plane using the "subtraction" technique in [28]. As illustrated by both figures there is very good agreement between the experimental and computed radiation patterns.

The results obtained from this study lead us to conclude that the analysis of pyramidal horn antennas mounted on a ground plane can be performed accurately and efficiently using the stepped-waveguide and Moment Method procedure.

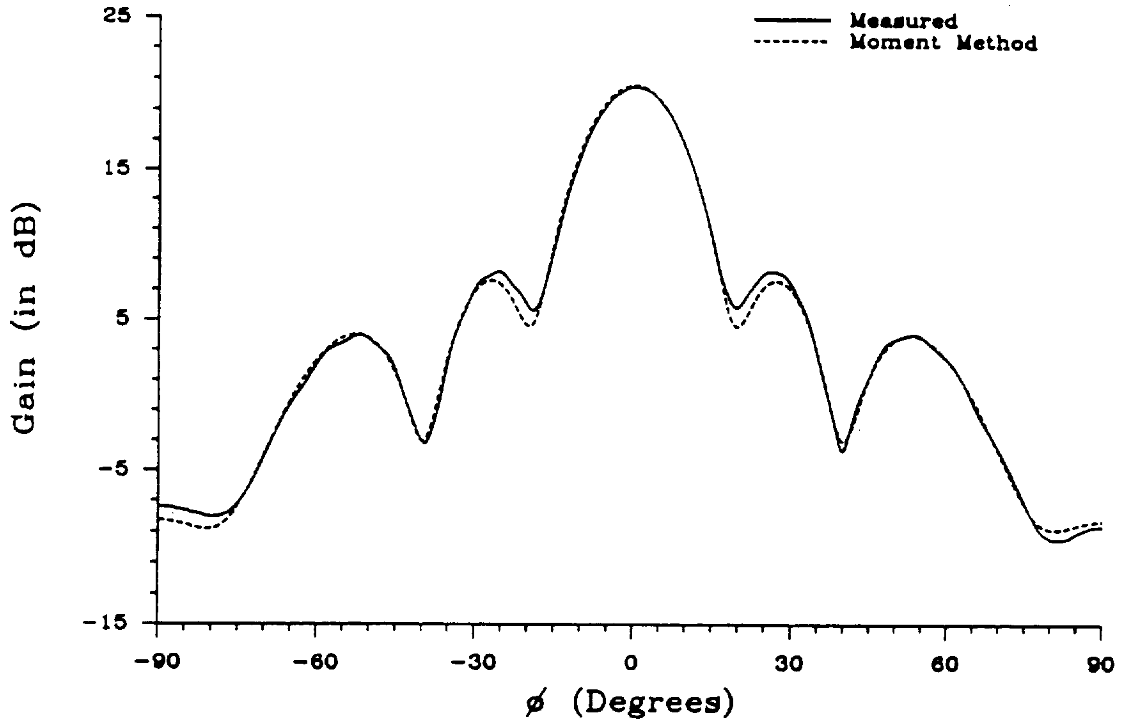

Fig. 1.9: E-plane radiation patterns of a 20-dB X-Band standard gain horn at 10 GHz, mounted on an infinite ground plane (A = 4.87″, B = 3.62″, L = 10.06″, a = 0.9″ and b = 0.4″).

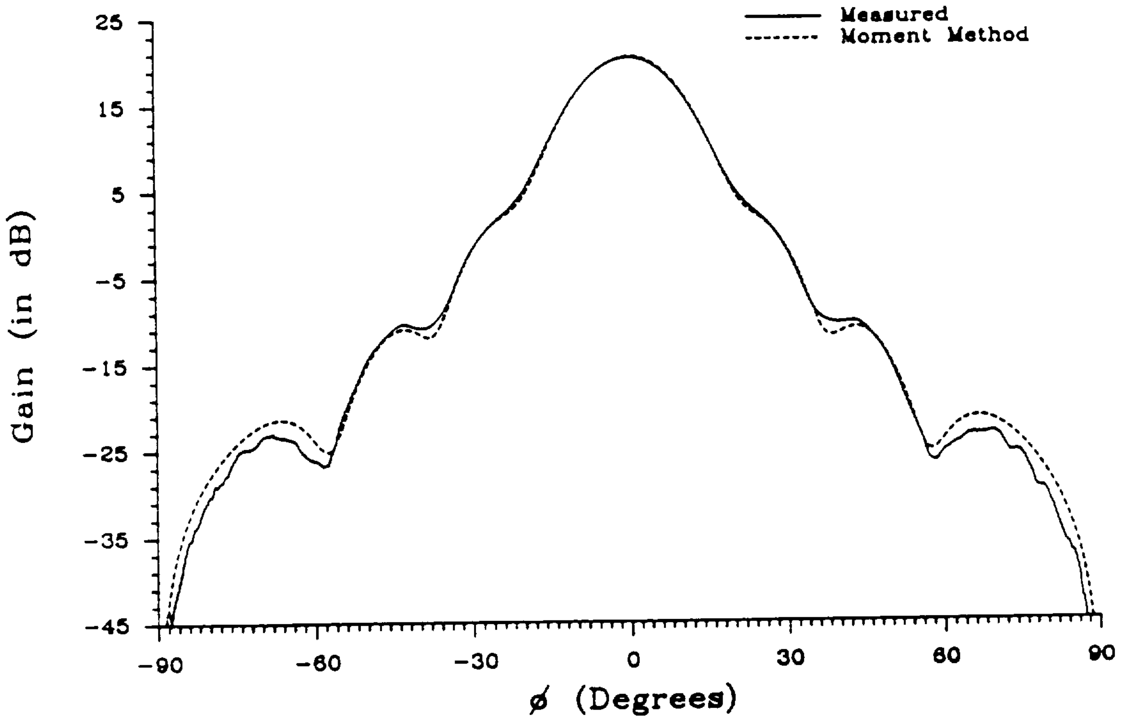

Fig. 1.10: H-plane radiation patterns of a 20-dB X-Band standard gain horn mounted on an infinite ground plane.

1.2.3 Pyramidal Horn Antennas in Free Space

Fig. 1.11 illustrates a pyramidal horn antenna in free space. The field problem in this case also can be separated into two parts. The first part includes the transition from the feeding waveguide to the radiating aperture. The second part includes the aperture radiating into the free space.

The interior transition from the feeding waveguide to the aperture can be analyzed using the stepped-waveguide model as outlined previously for the analysis of pyramidal horns mounted on a ground plane. However, in order to obtain accurate sidelobe levels of the antenna pattern, a sufficient number of terms in the series must be included because higher order modes at the aperture contribute significantly to the radiation pattern in the back regions. Significantly more terms are needed for this analysis than that in [12, 13] for pyramidal horns mounted on a ground plane. An empirically derived formula for determining M and N is the nearest higher integer of

$$(M,N) = \frac{3(A,B)}{\lambda} + 1.5 \tag{1.42}$$

where A and B are the dimensions of the horn aperture. When analyzing a high-gain horn antenna, the required number of modes determined by (1.42) is large, and if used throughout the matching process, the computation could become very inefficient. To reduce the computation time, a variable number of modes was used along the transition. At each step, the number of modes was determined using the same criterion given for the aperture in (1.42) except A and B are replaced by the step dimensions. Therefore, only a few modes are required near the feed, whereas the number of modes approach (1.42) as the computation proceeds toward the horn aperture. This process preserves accuracy, and for the geometries considered in this research reduces the computation time by eight compared to that of a constant number of modes.

Due to the absence of the ground plane on the aperture, the modeling of the antenna aperture is more complicated. The following sections outline a hybrid field

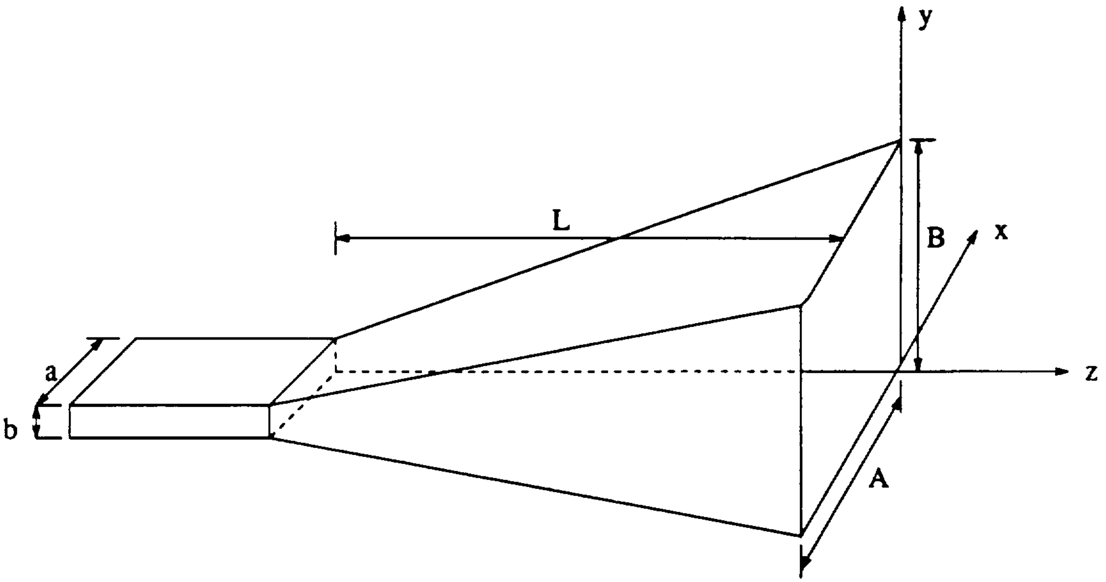

a) Pyramidal horn

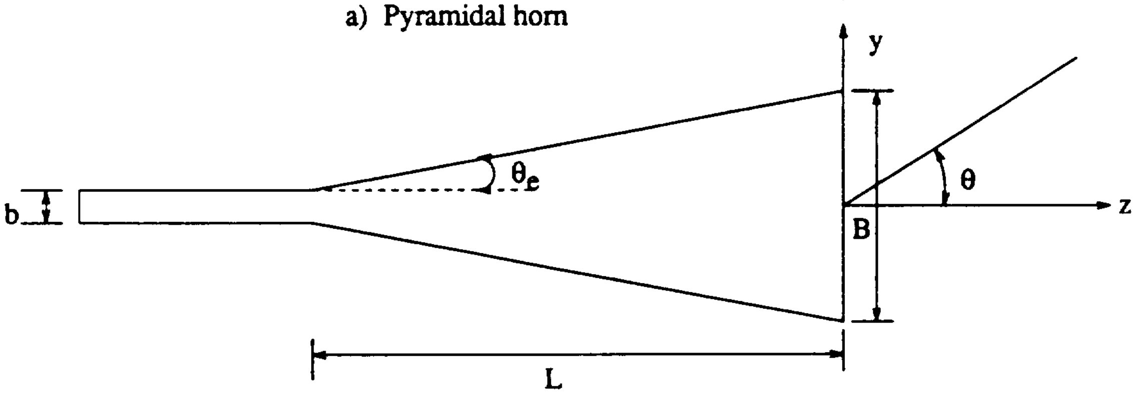

b) E-plane view

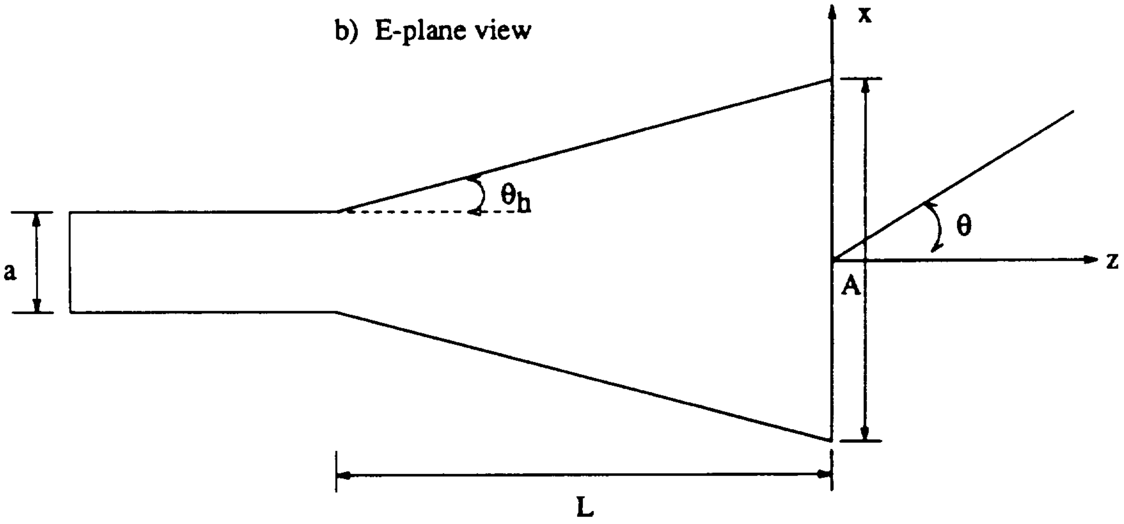

c) H-plane view

Fig. 1.11: Geometry of the pyramidal horn antenna in free-space.

integral equation formulation for the pyramidal horn aperture radiating into free space.

A. The Hybrid Field Integral Equation

Fig. 1.12 presents the general problem of a radiating aperture on a conducting body. The fields internal to the aperture are represented by the full-wave vectors **a** (the incident mode) and **b** (the reflected modes). To relate the internal and external fields on the aperture, *Love's field equivalence principle* [22] was introduced. The radiating aperture was replaced by a sheet of perfect electric conductor with a magnetic current density given by

$$\mathbf{M}(\mathbf{a}^{(A)} + \mathbf{b}^{(A)}) = -\mathbf{n} \times \mathbf{E}^{int}(\mathbf{a}^{(A)}, \mathbf{b}^{(A)}) \tag{1.43}$$

where **n** is the unit vector normal to the aperture, and $\mathbf{E}^{int}(\mathbf{a}^{(A)}, \mathbf{b}^{(A)})$ is the electric field internal to the aperture. Equation (1.43) insures the continuity of tangential electric fields across the aperture. The magnetic current density **M** is radiating in the presence of the closed conducting surfaces of the horn. An electric surface current is then induced to maintain zero tangential electric field on the external surfaces of the horn. The continuity of the tangential magnetic field across the aperture and the boundary conditions on the external surfaces require that

$$\mathbf{H}^{ext}_{tan}(\mathbf{M}) + \mathbf{H}^{ext}_{tan}(\mathbf{J}) = \mathbf{H}^{int}_{tan}(\mathbf{a}^{(A)}, \mathbf{b}^{(A)}) \quad \text{on the aperture} \tag{1.44}$$

$$\mathbf{E}^{ext}_{tan}(\mathbf{J}) + \mathbf{E}^{ext}_{tan}(\mathbf{M}) = 0 \quad \text{on the external surfaces and the aperture} \tag{1.45}$$

where field components with 'ext' denote the fields on the free-space side of the aperture. The boundary conditions of (1.43)-(1.45), derived from *Love's field equivalence principle*, satisfy the uniqueness theorem and define an equivalent to the actual electromagnetic problem.

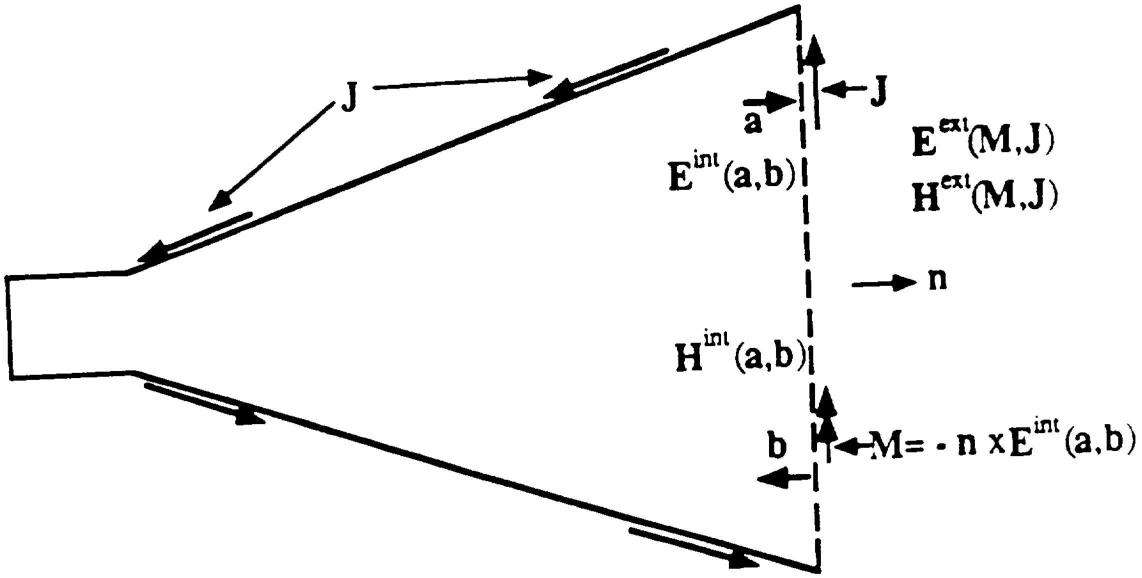

Fig. 1.12: HFIE model of the outside surface of the pyramidal horn.

B. Moment Method Solutions

In the Moment Method solution of the hybrid field integral equations of (1.43) and (1.45), subsectional quadrilateral roof-top patch modes were chosen as both expansion and testing functions for the electric current distribution on the exterior surfaces of the horn. To exploit the Toeplitz property of the impedance matrix elements, the magnetic current on the aperture was also expanded and tested with the same roof-top patch modes as those of electric current modes on the aperture. Thus, the impedance and admittance matrix elements for the integral equation solution on the aperture were related and were not computed twice. A more detailed explanation of such this process can be found in [28].

Since the aperture magnetic current density is related to the full-wave modes $\mathbf{a}^{(A)}$ and $\mathbf{b}^{(A)}$, a conversion matrix is introduced to transform the roof-top patch modes into eigen modes of the aperture field in (1.43)

$$\mathbf{J} = \sum_{i=1}^{N_J} J_i \mathbf{P}_i^J \qquad \mathbf{M} = \sum_{i=1}^{N_M} M_i \mathbf{m}_i = \sum_i M_i \sum_{j=1}^{N_A} V_{ij} \mathbf{P}_j^M \tag{1.46}$$

where $\mathbf{P}_i^J$ and $\mathbf{P}_j^M$ are the subsectional roof-top patch modes for the i-th electric and j-th magnetic current density modes, respectively; N_M is the total number of full-wave expansion modes of both TE and TM in the aperture. N_A is the number of roof-top patch modes representing the aperture magnetic current. N_J is the total number of roof-top patch modes representing the electric current on the entire outer surface of the horn including the aperture. $[V_{ij}]$ is the conversion matrix from the distribution functions of the aperture modes $\mathbf{m}_i$ expressed by $e_{mn}(x, y)$ and $h_{mn}(x, y)$ in (1.1) and (1.2) to the roof-top patch modes. Testing (1.45) with $\mathbf{P}_i^J$ leads to

$$- < \mathbf{P}_i^J, \mathbf{E}_{tan}^{ext}(\mathbf{J}) > = < \mathbf{P}_i^J, \mathbf{E}_{tan}^{ext}(\mathbf{M}) > \tag{1.47}$$

Substituting the expansion representation of $\mathbf{J}$ and $\mathbf{M}$ into (1.47), yields a matrix with elements given by

$$Z_{ij} = -\frac{1}{\eta} < \mathbf{P}_i^J, \mathbf{E}_{tan}^{ext}(\mathbf{P}_j^J) > \;=\; -\frac{1}{\eta} \int_{S_i} \int_{S_j} \mathbf{P}_i^J \cdot \mathbf{E}_{tan}^{ext}(\mathbf{P}_j^J) ds_i ds_j \tag{1.48}$$

$$Q_{kl} = < \mathbf{P}_k^J, \mathbf{E}_{tan}^{ext}(\mathbf{P}_l^M) > \; = \; \int_{S_k}\int_{S_l} \mathbf{P}_k^J \cdot \mathbf{E}_{tan}^{ext}(\mathbf{P}_l^M) ds_k ds_l \tag{1.49}$$

A normalization factor of $1/\eta$ is introduced in computing the matrix elements of Z_{ij} in (1.48) to reduce rounding errors in combining large matrices, which is very helpful in maintaining the numerical stability of the MFIE in (1.44). Efficient and accurate algorithms are developed for evaluating the four-fold integral of (1.48) and (1.49). Descriptions of the algorithm can be found in Appendix A.

Since the expansion and the testing modes are the same, the impedance matrix $\mathbf{Z}$ is a complex symmetric matrix. It can be filled and decomposed with only half of the CPU time needed for the full-matrix system [29, 30]. The solution of (1.47) is given by

$$\mathbf{J} \; = \; \frac{1}{\eta}\mathbf{Z}^{-1}\mathbf{U}\mathbf{M} \tag{1.50}$$

$$\mathbf{U} \; = \; \mathbf{Q}\mathbf{V}^t \tag{1.51}$$

where the superscript 't' signifies transpose. $\mathbf{J}$ is the vector representation of the subsectional roof-top patch modes, and $\mathbf{M}$ represents the aperture field modes. The transformation from $\mathbf{Q}$ to $\mathbf{U}$ in (1.51) reduces the number of right-hand side solution from N_A to N_M (N_M is generally a small fraction of N_A). Again, testing (1.44) with $\mathbf{m}_i$, the MFIE can be expressed by

$$< \mathbf{m}_i, \mathbf{H}_{tan}^{ext}(\mathbf{M}) > + < \mathbf{m}_i, \mathbf{H}_{tan}^{ext}(\mathbf{J}) > = < \mathbf{m}_i, \mathbf{H}_{tan}^{int}(\mathbf{a}^{(\mathbf{A})}, \mathbf{b}^{(\mathbf{A})}) > \tag{1.52}$$

Using duality for the reaction of aperture magnetic current modes[28], reciprocity for the reactions between the aperture magnetic mode and the outer surface electric modes, and the relation of (1.48), (1.52) can be written as

$$\mathbf{b}^{(A)} = \mathbf{S}^{(A)11}\mathbf{a}^{(A)} \; = \; [\mathbf{Y}^{(A)} + \mathbf{Y}^{int}]^{-1}[\mathbf{Y}^{int} - \mathbf{Y}^{(A)}]\mathbf{a}^{(A)} \tag{1.53}$$

where $\mathbf{I}$ is the identity matrix, $\mathbf{Y}^{(A)}$, and $\mathbf{Y}^{(int)}$ the aperture admittance matrices defined by

$$\mathbf{Y}^{(A)}(\mathbf{a}^{(A)}+\mathbf{b}^{(A)}) = [\mathbf{V}\mathbf{Z}^{(A)}\mathbf{V}^t + \mathbf{U}^t\mathbf{Z}^{-1}\mathbf{U}][< \mathbf{m}_i, \mathbf{M}(\mathbf{a}^{(A)}+\mathbf{b}^{(A)}) >] \quad (1.54)$$

$$\mathbf{Y}^{int}(\mathbf{a}^{(A)}-\mathbf{b}^{(A)}) = [< \mathbf{m}_i, \eta\mathbf{H}^{int}_{tan}(\mathbf{a}^{(A)}-\mathbf{b}^{(A)}) >] \quad (1.55)$$

where $\mathbf{Z}^{(A)}$ is a subset of $\mathbf{Z}$ for electric current modes on the aperture. Using (1.53) and (1.39), the incident aperture field distribution coefficients (denoted by a vector $\mathbf{a}^{(A)}$) and the reflected wave at the feed (denoted by a scalar coefficient $b_{10}^{(F)}$) are given by

$$\mathbf{a}^{(A)} = (\mathbf{I}-\mathbf{S}_{22}^{(T)}\mathbf{S}^{(A)})^{-1}\mathbf{S}_{21}^{(T)}a_{10}^{(F)} \quad (1.56)$$

$$b_{10}^{(F)} = [\mathbf{S}_{11}^{(T)}+\mathbf{S}_{12}^{(T)}\mathbf{S}^{(A)}(\mathbf{I}-\mathbf{S}_{22}^{(T)}\mathbf{S}^{(A)})^{-1}\mathbf{S}_{21}^{(T)}]a_{10}^{(F)} \quad (1.57)$$

where $a_{10}^{(F)}$ is the magnitude of the incident TE_{10} mode in the feeding waveguide. Equations (1.57), (1.56), (1.53), and (1.50) specify the antenna reflection coefficient (or return loss), the aperture magnetic current distributions, and the electric current distributions on the exterior surfaces. The radiated electric field can be determined from the current expansions and the gain computed from

$$G(\theta,\phi) = 10\log_{10}\frac{|\mathbf{E}(\mathbf{J},\theta,\phi)+\mathbf{E}(\mathbf{M},\theta,\phi)|^2}{4\pi|a_{10}^{(F)}|^2\sqrt{1-(\frac{f_c}{f})^2}} \quad (1.58)$$

where f_c is the cut-off frequency of the feeding waveguide, and f is the operating frequency.

1.3 Results and Discussions

Five X-band high-gain pyramidal horns were chosen for this analysis. Table 1.1 gives the dimensions and typical computed data for a maximum segment length of 0.15λ for 10- and 15-dB standard gain horn, and 0.2λ for the other three horns in the quadrilateral roof-top expansion of the exterior surfaces at 10 GHz. The CPU times are typical for an IBM R6000-350 workstation.

Table 1.2 lists the gains and VSWR's obtained by the approximate method and the technique of this report. As expected, differences are more obvious for 10-dB gain horn since the approximate method [4] does not work very well for such a small horn. Table 1.3 compares approximated, measured, and predicted gains and VSWR's for the 20-dB X-band standard gain horn antennas at three different frequencies. Note that the gains listed in the tables have almost a constant 0.2 dB difference between the moment method solution and the measured data. The same amount of difference is observed between computed and measured gains for the other two large X-band square aperture horns. It should be mentioned that the same 20-dB standard-gain horn is used as the calibration antenna. Therefore, if there is any inaccuracy in the calibration data, all measured data sets are affected. The agreement between the computed and measured VSWR's is excellent.

Table 1.1: Typical data of pyramidal horn antennas analyzed

	Pyramidal	horn	dimensions	EFIE Matrix	CPU
	A	B	L	size(# of rows)	(in hrs)
10-dB Standard-gain horn	1.58″	1.15″	2.01″	820	0.38
15-dB Standard-gain horn	2.66″	1.95″	5.46″	1600	0.61
20-dB Standard-gain horn	4.87″	3.62″	10.06″	4300	1.8
5-inch square horn	5.04″	5.06″	10.5″	5700	2.6
7-inch square horn	7.0″	7.0″	12.1″	9600	11.3

Figs. 1.13 to 1.14 compare the E- and H-plane patterns obtained from this method and the approximate method for the two smaller X-band horns, respectively. The approximate patterns are computed using the method outlined in Chapter 12 in [4], except that the free-space wave impedance in (12.1d) is replaced by the guide wave impedance at the aperture. As expected, the agreement in Fig. 1.13 is not as

Table 1.2: Comparison of VSWR's and gains of 10- and 15-dB standard gain horns

		8.2 GHz		10.3 GHz		12.4 GHz	
		VSWR	Gain	VSWR	Gain	VSWR	Gain
10-dB	Approximate	N/A	8.98 dB	N/A	11.13 dB	N/A	12.81 dB
Horn	This Method	1.18	9.75 dB	1.17	11.63 dB	1.20	13.48 dB
15-dB	Approximate	N/A	13.83 dB	N/A	15.83 dB	N/A	17.42 dB
Horn	This Method	1.11	14.23 dB	1.14	15.94 dB	1.10	17.58 dB

Table 1.3: Comparison of VSWR's and gains of the 20-dB standard gain horn

	9 GHz		10 GHz		11 GHz	
	VSWR	Gain	VSWR	Gain	VSWR	Gain
Approximate	N/A	19.77dB	N/A	20.59dB	N/A	21.31dB
This Method	1.082	19.98dB	1.057	20.63dB	1.031	21.46dB
Measured	1.10	19.72dB	1.06	20.46dB	1.04	21.24dB

good as in Fig. 1.14.

Fig. 1.15 compares the computed, approximated, and measured E- and H-plane patterns for the 20-dB standard gain horn. Since the horn is much larger than the previous two horns, the approximate method compares well with the measurements in the first few lobes of the patterns. However, the patterns predicted using the moment method code compare much better with the measured patterns. The improvement over the approximate method is more evident in the back region of the antenna.

In 1965, Russo *et al.* [5] presented an investigation of using different wall thicknesses to model the horn and their effect on the E-plane patterns of pyramidal horns using GTD. Fig. 1.16 presents our comparisons of the E- and H-plane patterns for the 5-inch square X-band horn at 10.0 GHz with and without modeling the aperture wall thickness. This comparison agrees with Russo's conclusion for the E-plane radiation patterns. However, for the H-plane patterns, the predicted patterns of the thin wall model do not agree in the back region with the measured patterns as well as those of the thick wall model. The thick wall model accurately predicts the fine ripple structure in the back region while the thin wall model does not. The aperture wall thickness affects the fine ripple structures of the H-plane patterns. The addition of the outer surface of the feeding structure in the EFIE has only a negligible effect on the patterns of the horn antennas.

Another advantage of the solution implemented in this research is the ability to examine the aperture field distribution. Figs. 1.17 to 1.19 represent computed aperture field (E_y and H_x components) distributions of the three X-band pyramidal horns at 10 GHz, respectively. Contrary to the approximation that the aperture fields are basically TE_{10} with parabolic phase fronts, the distributions presented here demonstrate a more complicated shape. The deviations from the approximate aperture distributions are more evident for H_x. Figs. 1.17 to 1.19 also illustrate that as the electrical size of the aperture become larger, the amplitude distributions become more complicated, but the phase distributions approach a parabolic phase front as assumed by the approximate method.

As presented in the comparisons between computed and measured results, the full-wave HFIE method has demonstrated an excellent accuracy both for small and large pyramidal horn antennas. One of the requirements of this method in solving large pyramidal horns is computer memory. In some workstations such as the IBM RS6000/350, the fast data transferring capability between the memory and the hard-disk enables the out-of-core memory matrix solver for a symmetric complex system to run nearly as fast as the in-core solver. If the symmetric property of the electric current distribution on the exterior surfaces is utilized, the memory can be reduced to 1/8 while the CPU time can be decreased to about 1/4 of the values listed in Table 1.1.

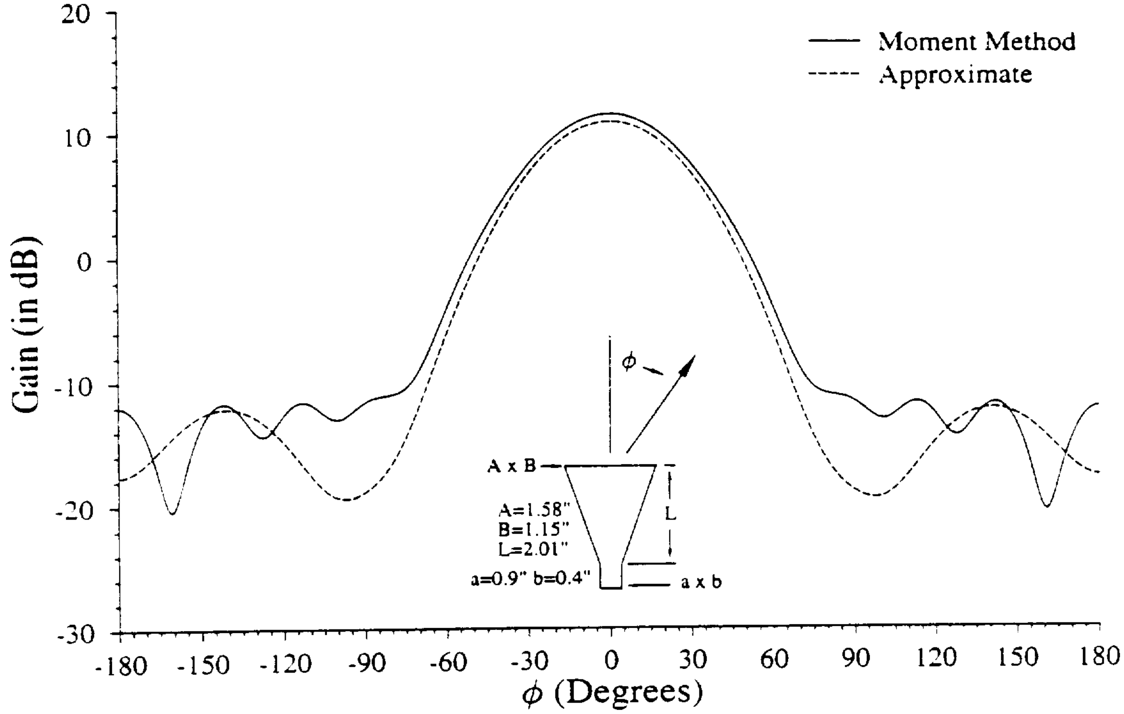

(a) E-plane

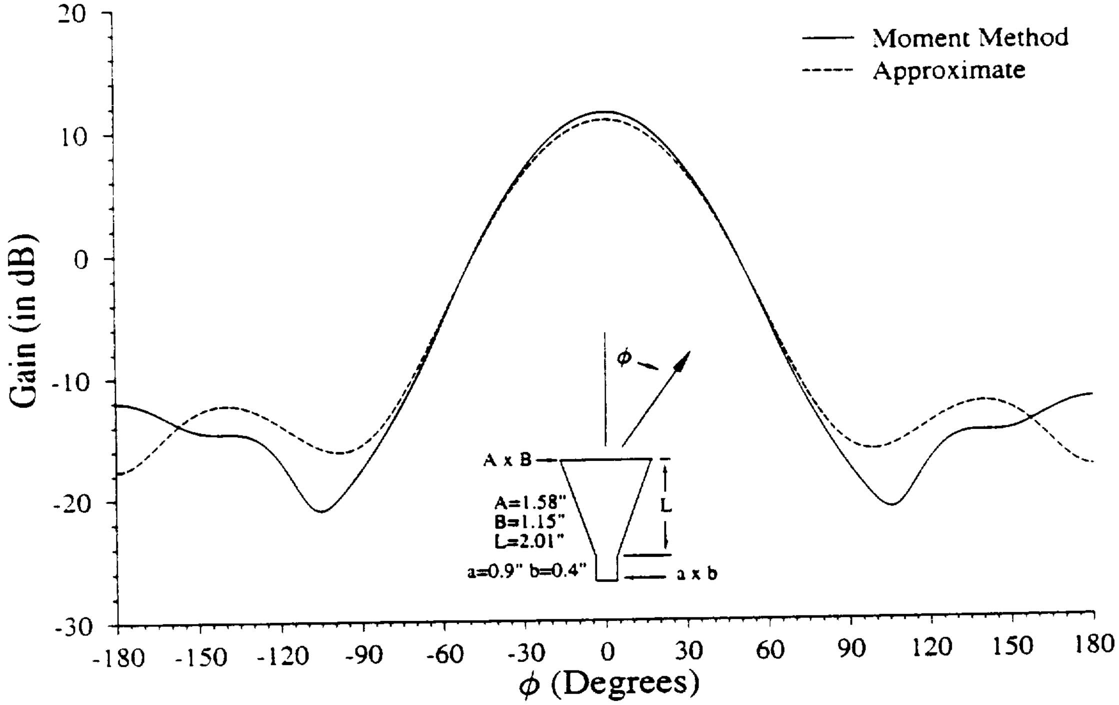

(b) H-plane

Fig. 1.13: Comparison of E- and H-plane patterns for 10-dB standard gain horn at 10 GHz.

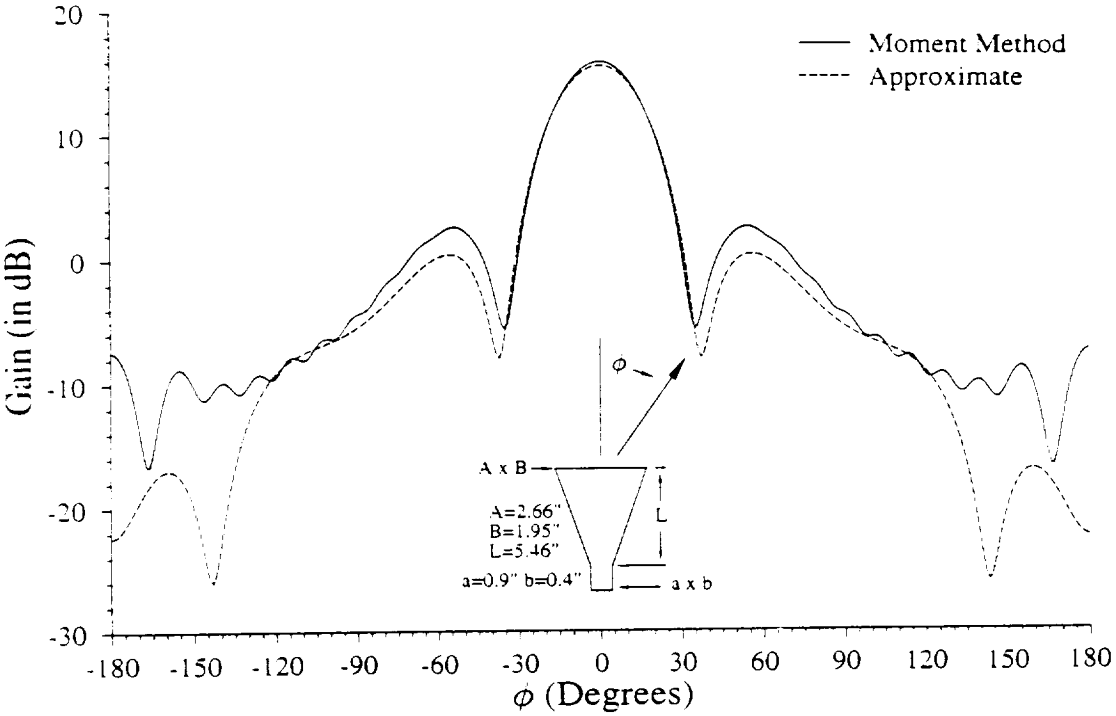

(a) E-plane

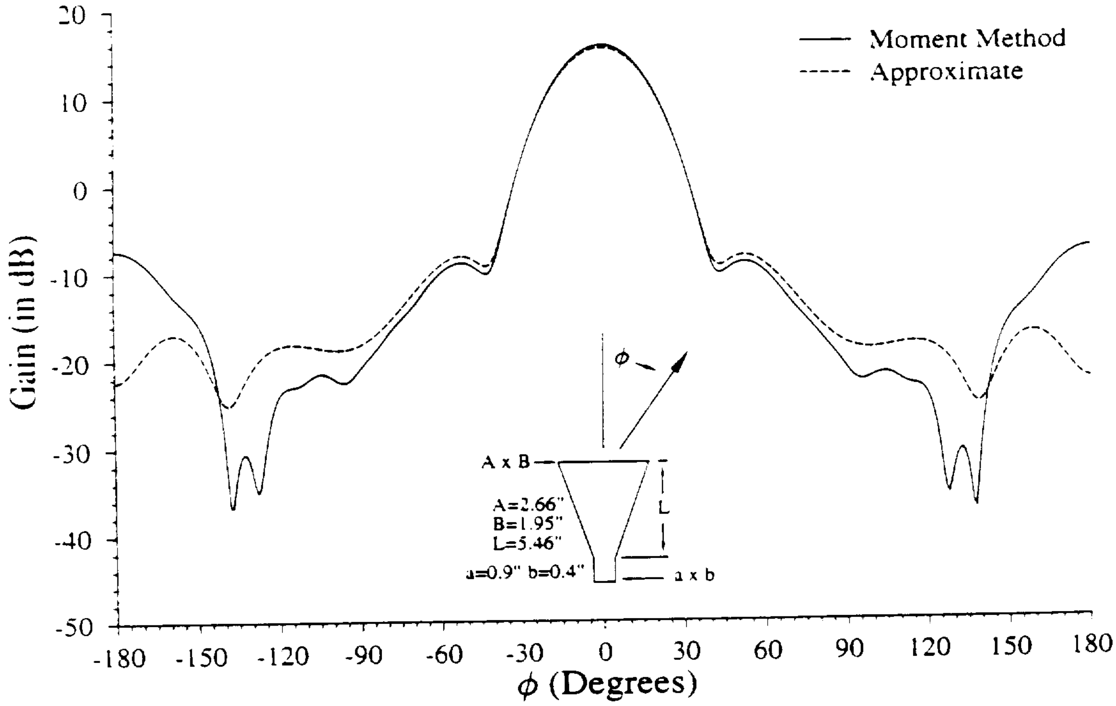

(b) H-plane

Fig. 1.14: Comparison of E- and H-plane patterns for 15-dB standard gain horn at 10 GHz.

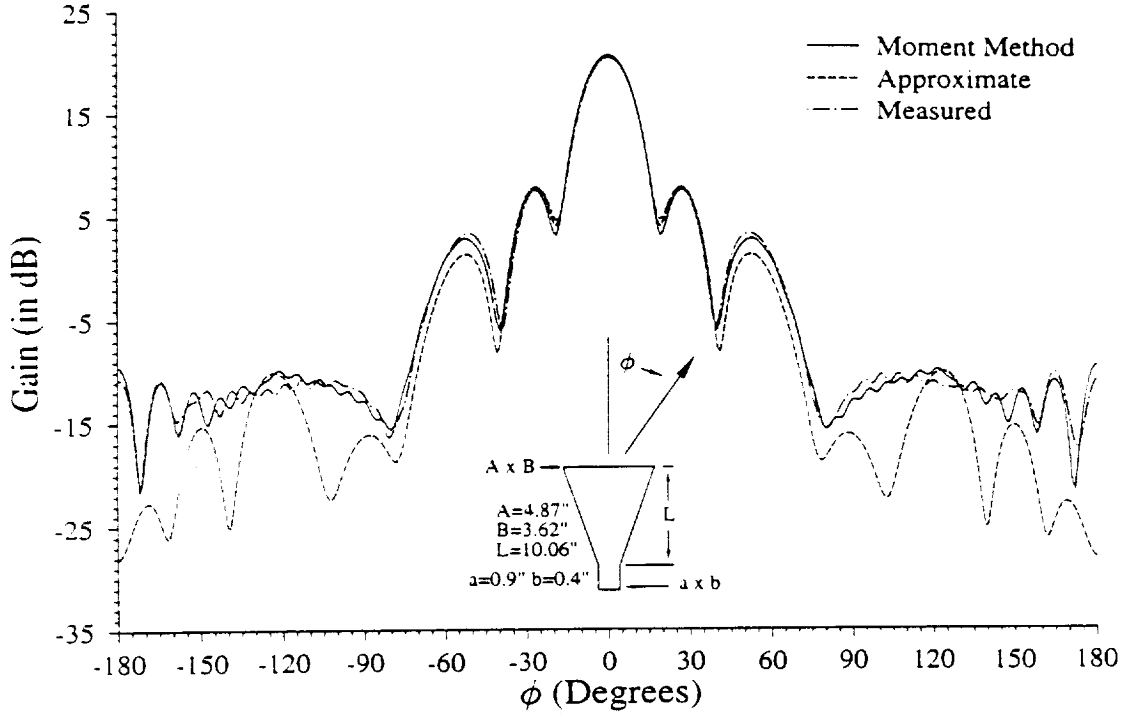

(a) E-plane

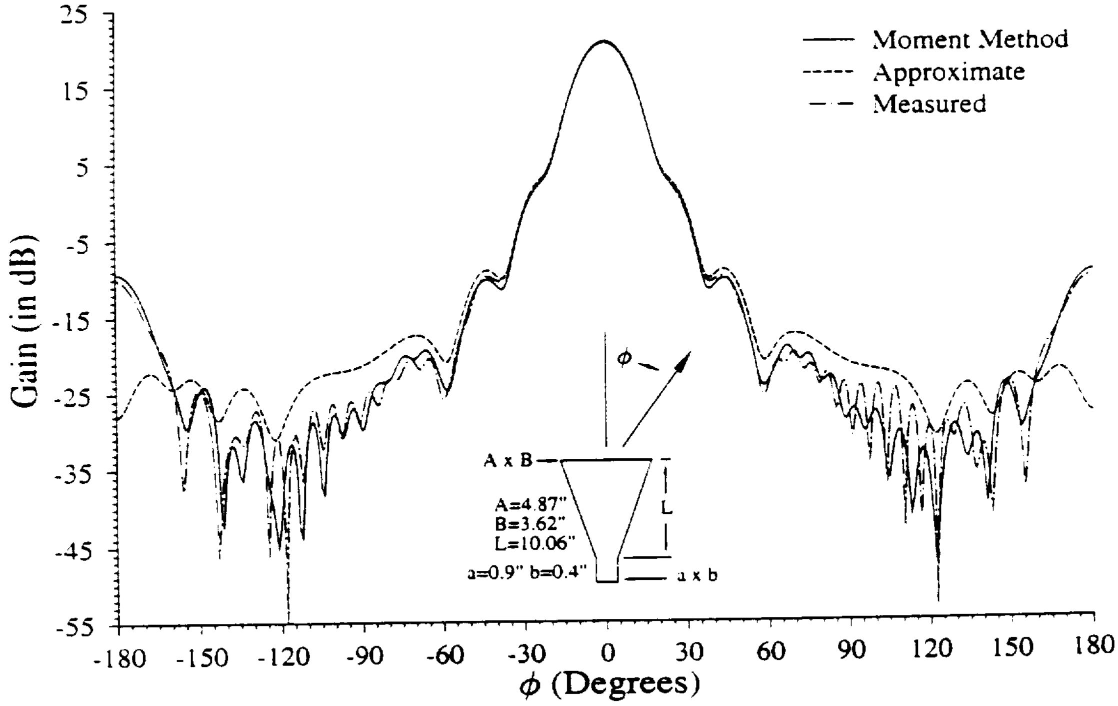

(b) H-plane

Fig. 1.15: Comparison of E- and H-plane patterns for 20-dB standard-gain horn at 10 GHz.

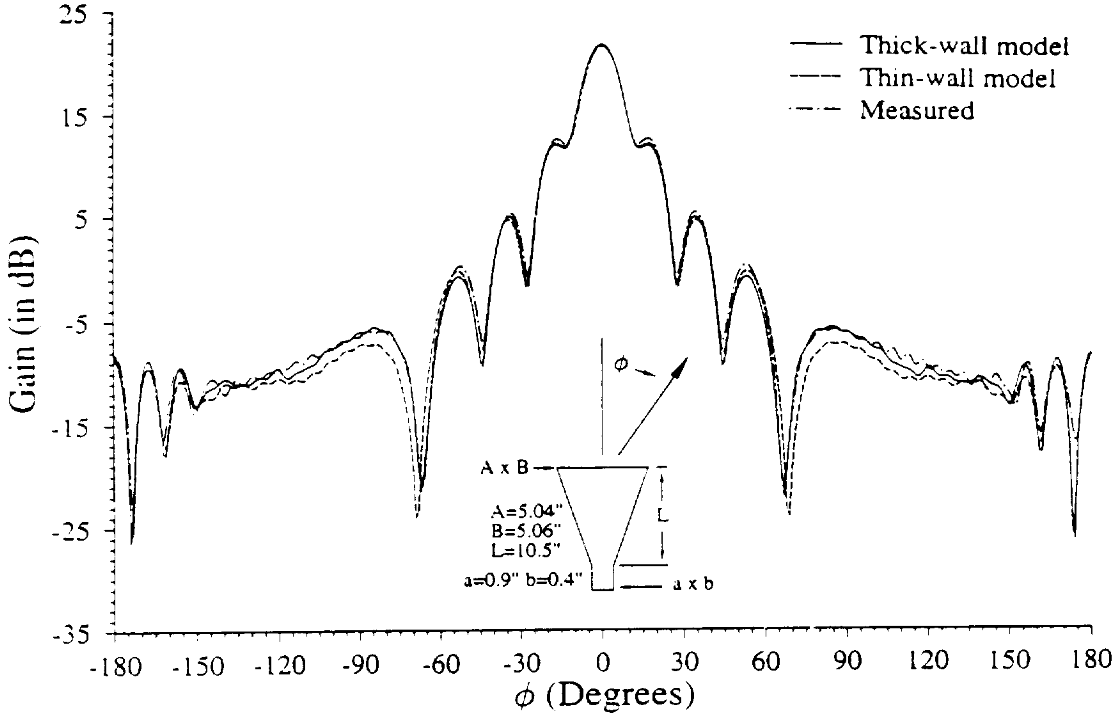

(a) E-plane

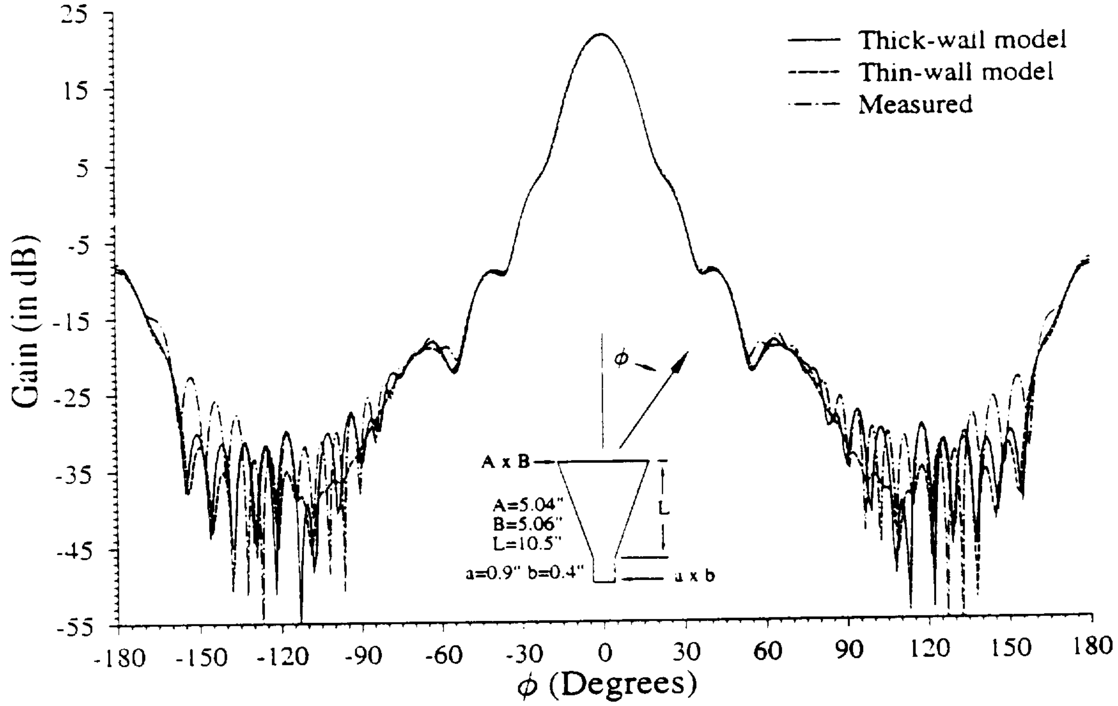

(b) H-plane

Fig. 1.16: Comparison of E- and H-plane patterns for different aperture wall models of 5-inch horn at 10 GHz.

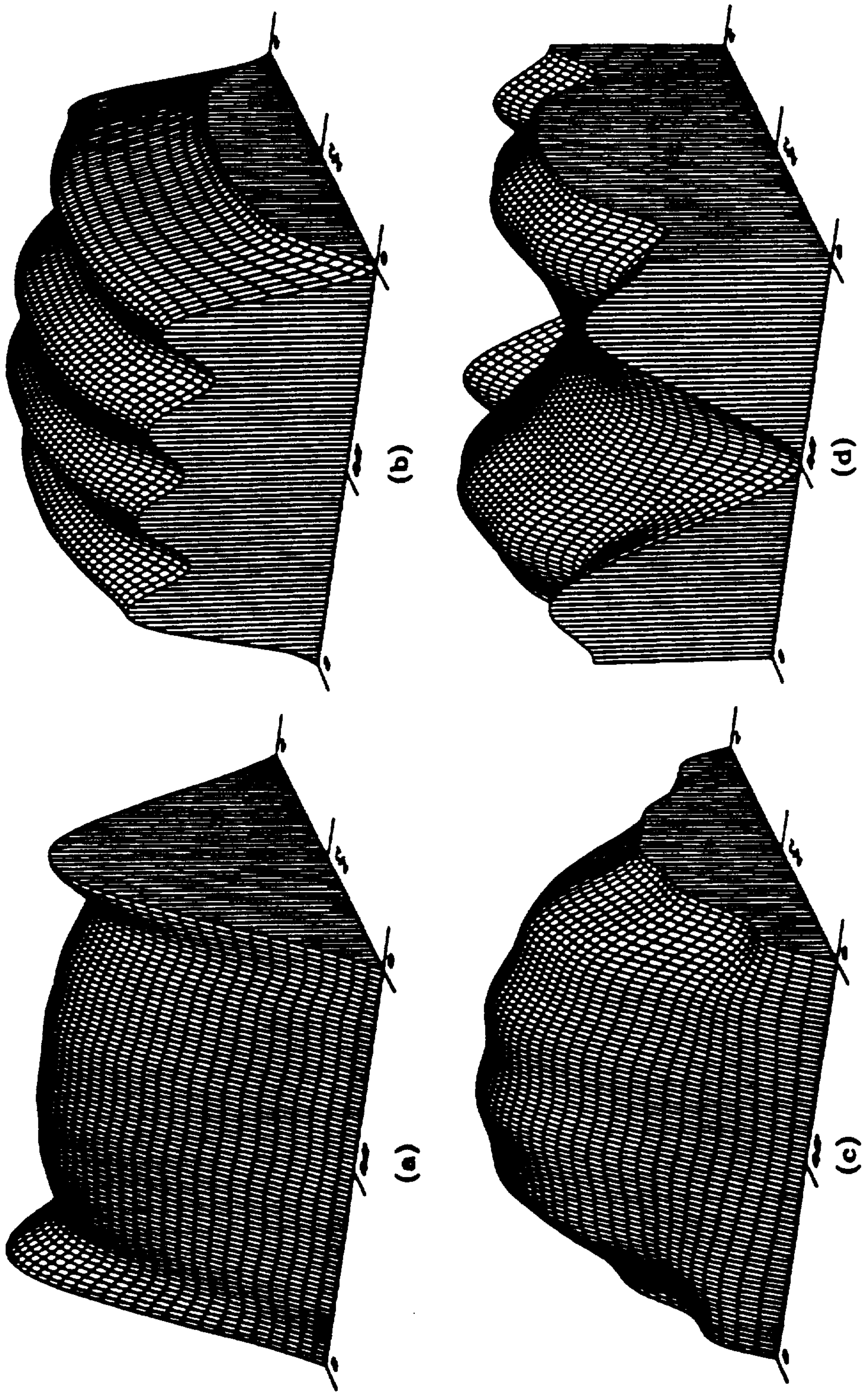

Aperture fields of 10-dB standard gain horn at 10 GHz.

(a), (b)—Magnitude and phase distributions of E_y

(c), (d)—Magnitude and phase distributions of H_x

Fig. 1.17: Aperture fields of 10-dB X-band standard-gain horn at 10 GHz.

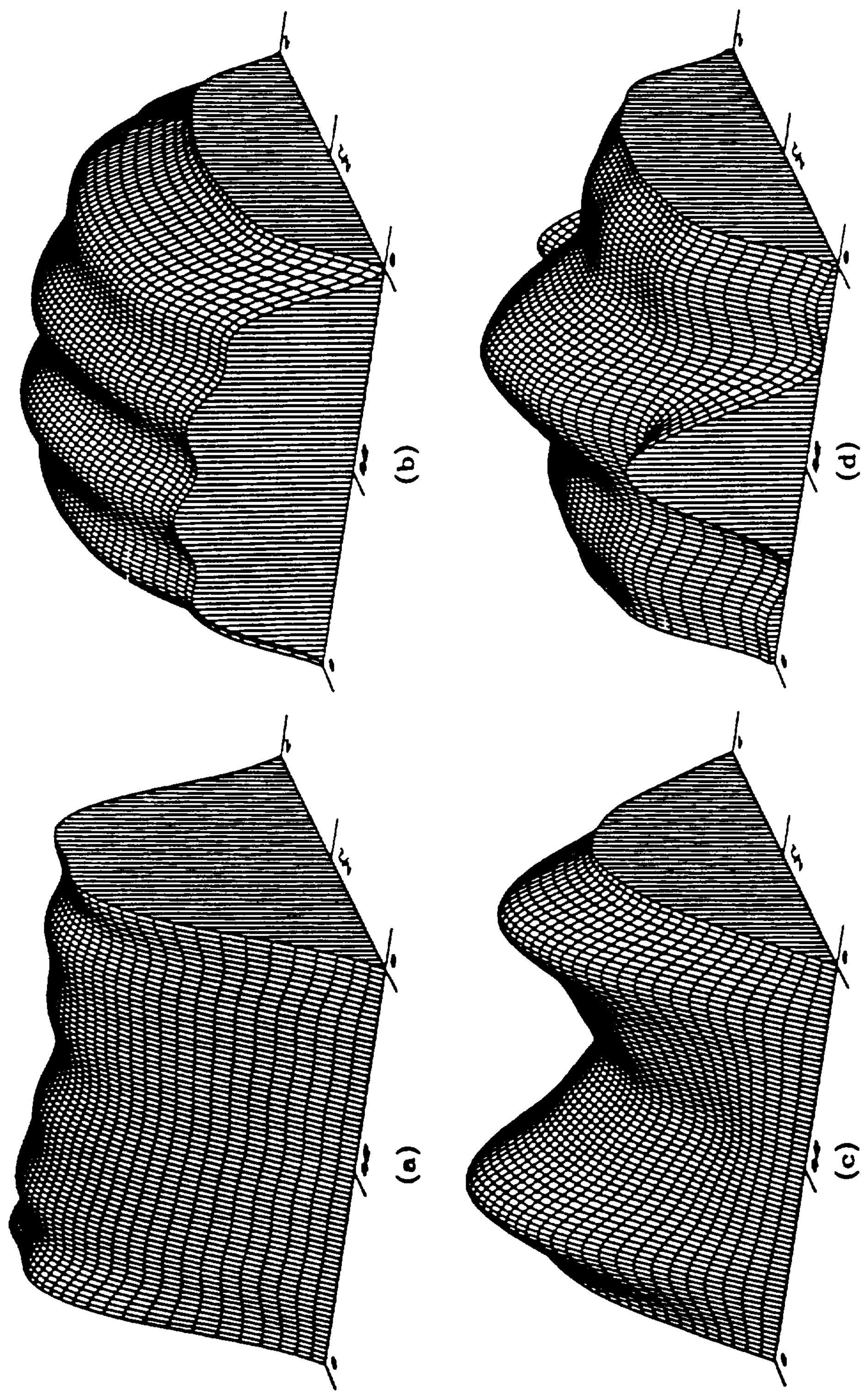

Aperture fields of 15–dB standard gain horn at 10 GHz.
(a), (b)——Magnitude and phase distributions of E_y
(c), (d)——Magnitude and phase distributions of H_x

Fig. 1.18: Aperture fields of 15-dB X-band standard-gain horn at 10 GHz.

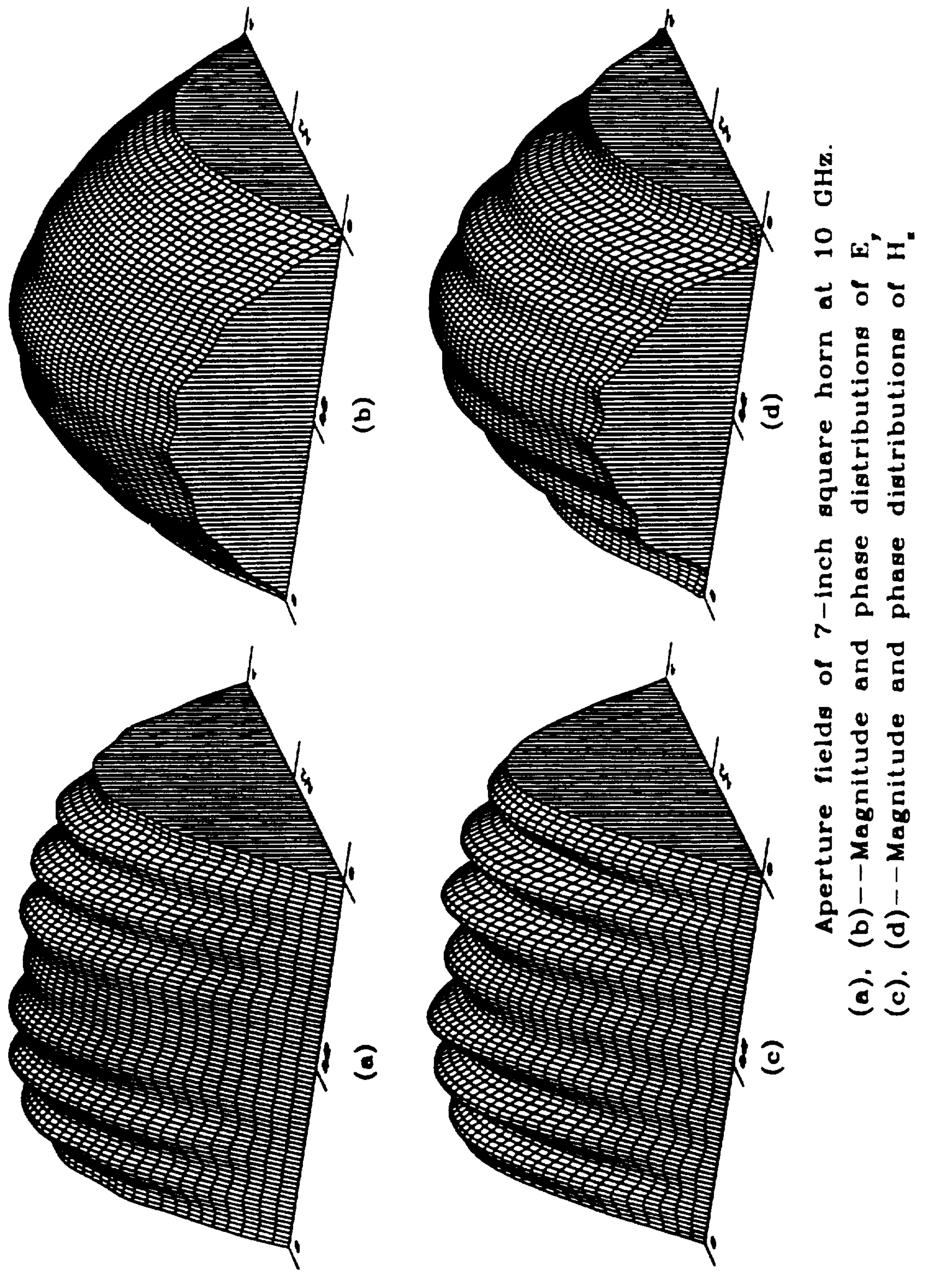

Fig. 1.19: Aperture fields of 7-inch horn at 10 GHz.

1.4 Conclusions

A full-wave, hybrid field integral equation method has been developed to analyze electromagnetic horns of pyramidal configuration. The model includes the current induced on the exterior surfaces and has been verified by comparison of computed and measured data. For accurate results, the following guidelines are suggested:

- include a sufficient number of higher order modes in the full-wave analysis. The required number of modes is determined using the empirical formula (1.42).
- limit the size of the stepped discontinuity to less than $\lambda/32$ when approximating continuous horn transition.
- limit the largest segment size of the roof-top patch to less than 0.2λ to ensure an effective and accurate solution of the electric field integral equation on the outer surfaces of the pyramidal horn antenna.
- include the wall thickness in the segmentation of the outer surface.

The research in this project demonstrated that the approximate method found in most antenna books is not very accurate in predicting gains and patterns of the pyramidal horns of small electrical size. However, as the electrical size gets larger, the approximate method becomes more accurate in predicting gains and the first few sidelobes of the far-field radiation patterns of a pyramidal horn. The aperture field distributions of pyramidal horns are much more complicated than those predicted by the approximate formula. However, the phase distribution approaches a parabolic distribution for apertures of large electrical sizes.

Although a straight forward application of this method is computationally intensive, a widespread application of high-power workstations, such as the IBM RISC6000 platforms, is making it more effective to serve as a computer-aided analysis and design tool. Although the present development has concentrated on pyramidal horn antennas, the model can be extended to analyze wide-band dual-ridged, and quadruple-ridged horns.

CHAPTER 2

MOMENT METHOD ANALYSIS OF HORN ANTENNAS WITH LOSSY WALLS

2.1 Introduction

Most horn antennas with simple designs, including the pyramidal horn antenna, have asymmetric E- and H-plane radiation patterns and relatively high cross-polarization levels. These two properties become undesirable when the horns are used as feeding devices for reflector antennas. Many complex designs were developed to overcome these two undesirable features[1]. One was to introduce corrugations in the transition from the feeding waveguide to the radiation aperture. The corrugations on the interior surfaces of horns successfully suppress the sidelobes of the E-plane radiation pattern, maintain symmetric E- and H-plane radiation patterns, and reduce the cross-polarization [31, 32]. However, due to the high cost and heavy weight of the corrugations, application of corrugated horn antennas is still limited. The search for the substitution of the corrugations has become an interesting topic for many years [33, 34].

A waveguide with lossy wall was undesirable until Knop *et al.* discovered its antenna beam shaping capability in the early 1980's [33]. Independently, Lee *et al.* also noted the same field tapering in a circular waveguide by introducing a thin coating of lossy material on the waveguide[35, 36]. Knop *et al.* also applied this finding to shape the radiation pattern of a large conical horn antenna [37, 38]. Wang *et al.* introduced lossy magnetic coating to produce the same beam shaping results on pyramidal horns [39, 40]. Ghobrial *et al.* introduced lossy walls to suppress the cross polarization of a pyramidal horn used as a feeding antenna for a paraboloidal reflector [41]. These early experimental studies have demonstrated the effectiveness of lossy material coatings in controlling the radiation patterns of horn antennas. Although a few simplified methods were presented to provide guidelines in using lossy material coatings on the walls of horn antennas [36, 37, 38, 39, 40], a rigorous analysis for horn antennas with impedance walls has not been reported.

The full-wave, hybrid integral-equation method presented in this report provides an analytic solution to the pyramidal horn antennas with or without the impedance walls. The validation and efficiency of this analytical method is important in the application of lossy material coatings to control the radiation pattern of horn antennas.

2.2 Eigen Expansions

The coating of lossy materials on the walls of the horn antenna introduces a change of the electromagnetic field distribution along the horn transition. It is important to note that maintaining a symmetric coating is very important because asymmetry in the coating will introduce significant cross polarization, as noted in [41].

Fig. 2.1 shows the geometry of an E-plane coated horn transition and its stepped-waveguide model. One difference between the coated and uncoated stepped waveguide sections is the eigenfunctions in the full-wave expansions. To find the new eigenfunctions, the new eigenvalues for each individual eigenfunction based on the boundary conditions across the surfaces of the coating material must be found. Such process can be analyzed by using the Transverse Resonance Method (TRM) [22] when coatings are applied on the top and the bottom walls, and TM_y and TE_y modes are used to represent the field distribution. By using the TRM technique, the cross-sectional wave constants can be obtained by solving the following two complex transcendental equations for TE_y and TM_y modes respectively, are obtained:

$$\frac{\beta_e}{\epsilon_d}\tan(\beta_e h) + \beta_{oe}\tan(\beta_{oe} d) = 0 \qquad {\beta_e}^2 - {\beta_{oe}}^2 = \omega^2 \mu_o \epsilon_o(\mu_r \epsilon_r - 1) \tag{2.1}$$

$$\frac{\beta_m}{\mu_d}\cot(\beta_m h) + \beta_{om}\cot(\beta_{om} d) = 0 \qquad {\beta_m}^2 - {\beta_{om}}^2 = \omega^2 \mu_o \epsilon_o(\mu_r \epsilon_r - 1) \tag{2.2}$$

where (β_e, β_{oe}), and (β_m, β_{om}) are the complex propagation constants inside and outside the coating material for TE_y and TM_y modes, respectively.

The solution of (2.1) and (2.2) requires a complex root solver to obtain all the roots in the complete eigenvalue sequence. Such a complex root solver has been developed for this project. Once the complex eigenvalues are provided, the scattering matrix for each individual coated waveguide step can be found following a similar procedure as the one applied to the perfectly conducting waveguide step. The technique of combining the scattering matrices of the coated-waveguide steps is identical to that of the uncoated case.

When the modified electromagnetic field distribution (due to the presence of the lossy coating) is computed using the complex eigenfunctions, the results are analytical. The effect of impedance surfaces is therefore computed more accurately using the complex eigenfunctions than by using an approximate impedance boundary condition.

2.3 Low-Loss Design Using Impedance Surfaces

Investigation of using impedance surfaces in horn antennas for radiation pattern control have been conducted by many researchers [36, 38, 40]. The introduction of lossy material on the inner walls of the horn antenna presents a good alternative to corrugations. However, the coating of lossy material introduces ohmic losses ranging in gain losses from 0.5 dB in [38], 10 dB in [36], and 0.8-2.7 dB in [40]. Our objective in applying impedance surfaces to horn antennas is to control the horn antenna radiation pattern with minimum ohmic loss. This can be achieved through a comprehensive study of the effect of the coating on the the radiation patterns of horn antennas.

Based on the stepped-waveguide mode outlined in Fig. 2.1, the ohmic loss is mainly contributed by the imaginary part of the propagation constant of the dominant mode (HE_{11}) along the horn transition. Further studies of the eigenvalue of the dominant mode (HE_{11}) suggest that the ohmic losses depend upon the material properties, the thickness of the coating, and the size of waveguide cross section [42].

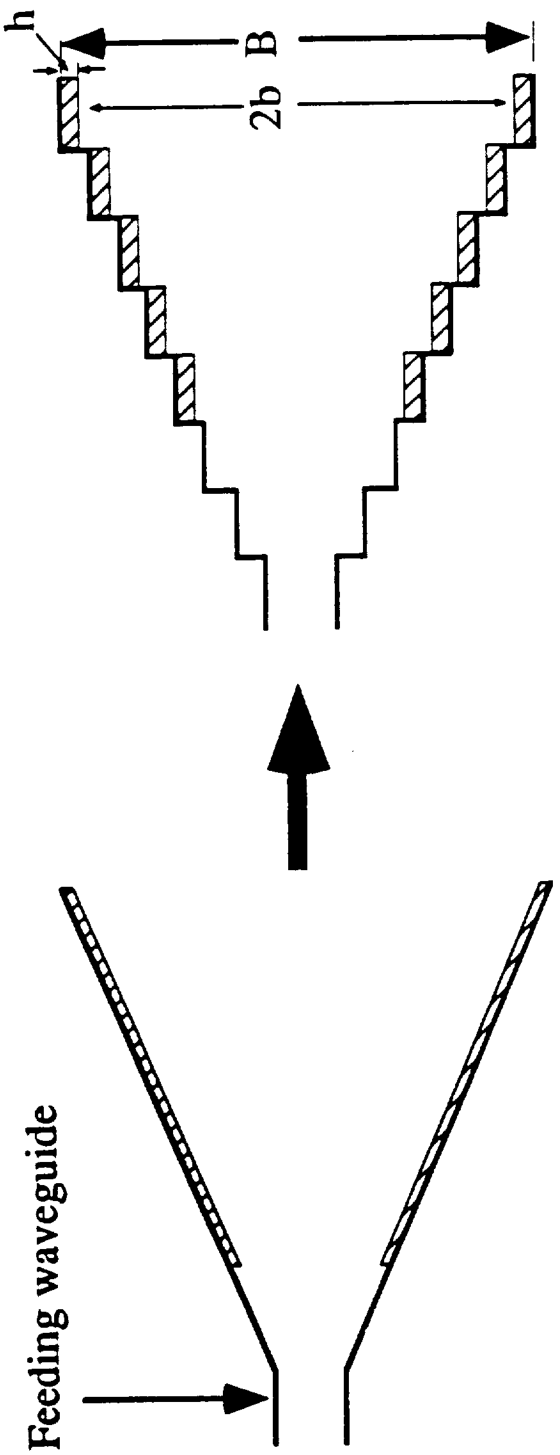

Fig. 2.1: Partially coated horn transition and its stepped waveguide model.

The following **design guidelines** hightlight the importance of each factor:

- As was noted in [36], the ohmic losses decrease monotonically as the cross-sectional size increases because the electromagnetic fields are expelled from the lossy material when the cross-sectional size of the horn transition is large. This explains why the antenna in [38] has significantly smaller ohmic losses than others. One can reduce the ohmic losses by not applying the lossy coating on the small cross-sectional portion of the horn transition while applying a robust coating on the large cross-sectional portion of the horn.
- For a large cross-sectional size antenna, the choice of the material is less critical. For a smaller size antenna, choice of the lossy material is more important to achieve the needed HE_{11} mode in the horn transition. A good material for such an application is one having a high magnetic loss.
- There exists an optimum thickness of the lossy material coating for low-loss implementation of the HE_{11} mode.

Both analytical and experimental results presented in a later section demonstrate a significant reduction of ohmic loss by following the above design guidelines.

2.4 Horn Transition with Impedance Walls

In previous reporting periods, we have presented the stepped-waveguide model for analyzing the lossy impedance coating on the interior surfaces of the horn transition. Figure 2.1 represents the stepped waveguide model for the analysis of a partially coated horn transition. Unlike the perfectly conducting part of the horn transition, the stepped-waveguide model for the lossy material coated section of the horn transition exhibits a much more complicated boundary conditions at the stepped discontinuity.

Fig. 2.2 shows three types of interfaces encountered in the stepped model. The difficulty involved in an accurate analysis of the lossy coating can be discussed in two parts. First, to avoid a high gain loss, the thickness of the lossy material coating should be relatively thin compared to the cross-sectional sizes of the horn transition. Therefore, to effectively control field tapering, the coated lossy material should have a relatively high dielectric constant and/or a high permeability[36, 39, 40]. The analysis of the field tapering can be carried out by using eigen modes provided by the partially-filled waveguide techniques [22]. An accurate expansion of the field distributions controlled, by a small part of the discontinuity at the edges of the cross section, requires many eigen modes. This requirement presents a challenge in the numerical implementation. Second, the stepped-waveguide model artificially creates media discontinuities at the stepped junction which could act as a false control on the field distributions.

To investigate these problem, three different techniques in modeling the coating discontinuity were studied in this project:

- Solving the stepped discontinuity exactly as shown in Figure 2.2. This technique is an exact boundary condition solution, if a real stepped discontinuity at the interface actually existed. However, due to the incompleteness of eigen modes and the artificially created material discontinuities, this method does not work very well. The predicted E-plane pattern presented in the previous report showed some discrepancies even in the main lobe of the pattern.

- Approximating the material interface by assuming a continuous material transition (there is no material-air interface as shown in Fig. 2.2 for the stepped discontinuity). By this assumption, the eigen values of eigen modes on both sides of the stepped discontinuity are assumed to have their original values. This method average out some of the artificial discontinuities on the interface. As a result, the computed patterns have demonstrated a better agreement with measured data.

- Hybrid Fourier transform method. This method applies a Fourier transform to

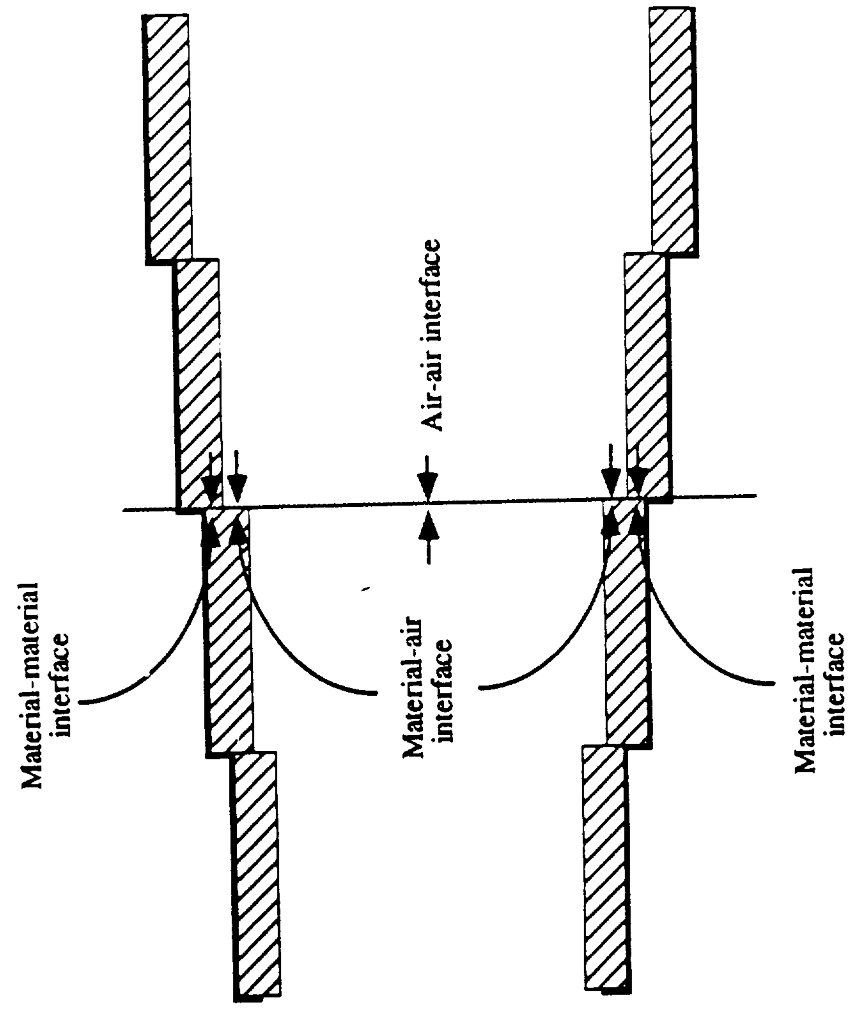

Fig. 2.2: Stepped discontinuity of in a stepped waveguide model.

expand the field distributions of eigen modes on both sides of the stepped discontinuity. By testing the transformed field distributions with different weighting functions at the discontinuity, the full-wave coefficients are related. Once the discontinuity is resolved, the field distributions are transformed back to the eigen mode expansion in the waveguide section to account for the propagation factor. This method provides the best agreement with measurements among the three methods considered. We do not yet have a sound explanation for this result. However, it looks like this method averages out the error more effectively than the other two.

2.5 Results and Discussions

Based on the hybrid Fourier transform stepped discontinuity algorithm, numerical simulations were carried out to predict the E-plane radiation patterns for the 20-dB X-band standard gain horn with 2cm, 5cm, and 10cm Northrop Nitrile lossy magnetic material coating from the radiating aperture. The Nitrile material has a measured relative permittivity of $18.75 - j0.1$ and a relative permeability of $1.55 - j1.85$ at 10 GHz. The thickness of the material is 44 mils. However, considering the tilting effect when the material is coated, the effective thickness is taken to be 44.41 mils. In Figs. 2.3 through 2.5, the predicted patterns of the horn without a material coating (PEC wall surfaces) are included to demonstrate the effect of lossy material coatings on the control of antenna radiation patterns.

Fig. 2.3 compares the measured and predicted E-plane radiation patterns for the 20-dB X-Band standard gain horn with 2cm of lossy magnetic coating. We observe a good agreement in the main lobe and small discrepancies in the back region. This demonstrates that the Fourier transform technique can be used to analyze the lossy coatings with reasonably good accuracy. Fig. 2.4 represents the E-plane patterns for the same horn with 5cm of lossy magnetic material coating. It exhibits the same agreement as that of Fig. 2.3 except that the measured gain is a about 0.7 dB lower than predicted. Fig. 2.5 compares the E-plane patterns for the horn with 10cm lossy magnetic coating. In this figure, more discrepancies between the predicted and measured patterns are observed. It is believed that the discrepancies are caused by the following two sources:

- The inaccuracy of the stepped waveguide model in the lossy horn transition. A thin lossy material coating on the E-plane surfaces of the pyramidal horn introduces an abrupt discontinuity for the electric field of the dominant mode. This discontinuity is more severe for the Nitrile material which has a very high dielectric constant. Since the material is very thin compared to the horn transition, it is very difficult for any numerical method to model very accurately and efficiently. Such a disagreement becomes more evident when a larger portion of the horn transition is coated by the lossy material.

- The imhomogeneous lossy material. The lossy materials used in the experimental verification may not be homogeneous. Therefore, the material constants used in the analysis, which is measured from samples of the material, may not have accurate representation of the material actually used in coating the horn surfaces.

Figs. 2.3 to 2.5 also demonstrate that the application of the lossy materials on the E-plane walls has a strong control on the E-plane radiation patterns. The length, the thickness, and the properties of the material coating control the sidelobe level of the E-plane in a very sensitive manner. Therefore, there exists an optimum design of material coating for beam shaping without a significant loss of the antenna gain.

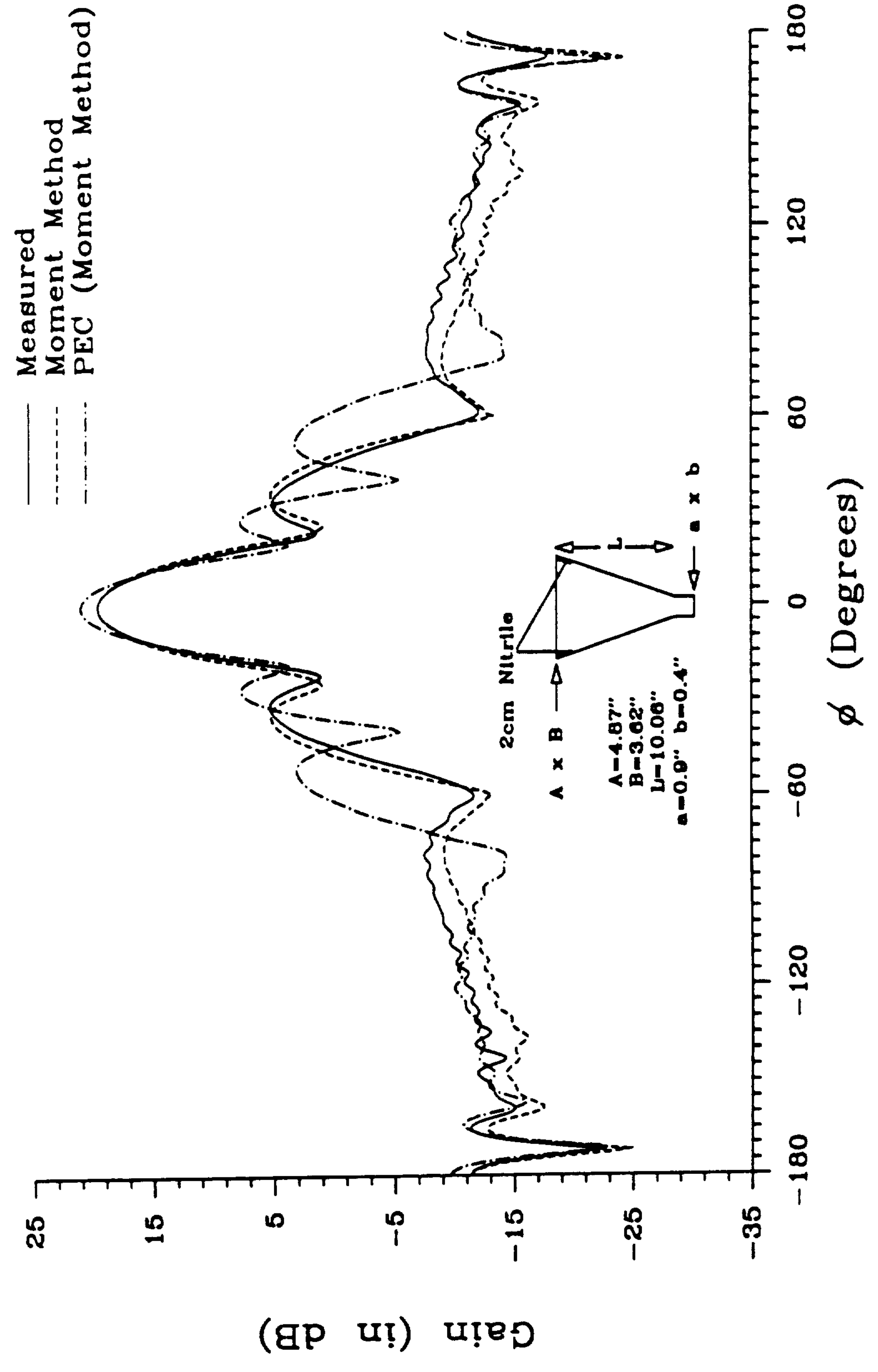

Fig. 2.3: Comparison of E-plane patterns for standard gain horn at 10 GHz with 2cm of lossy Nitrile material coating.

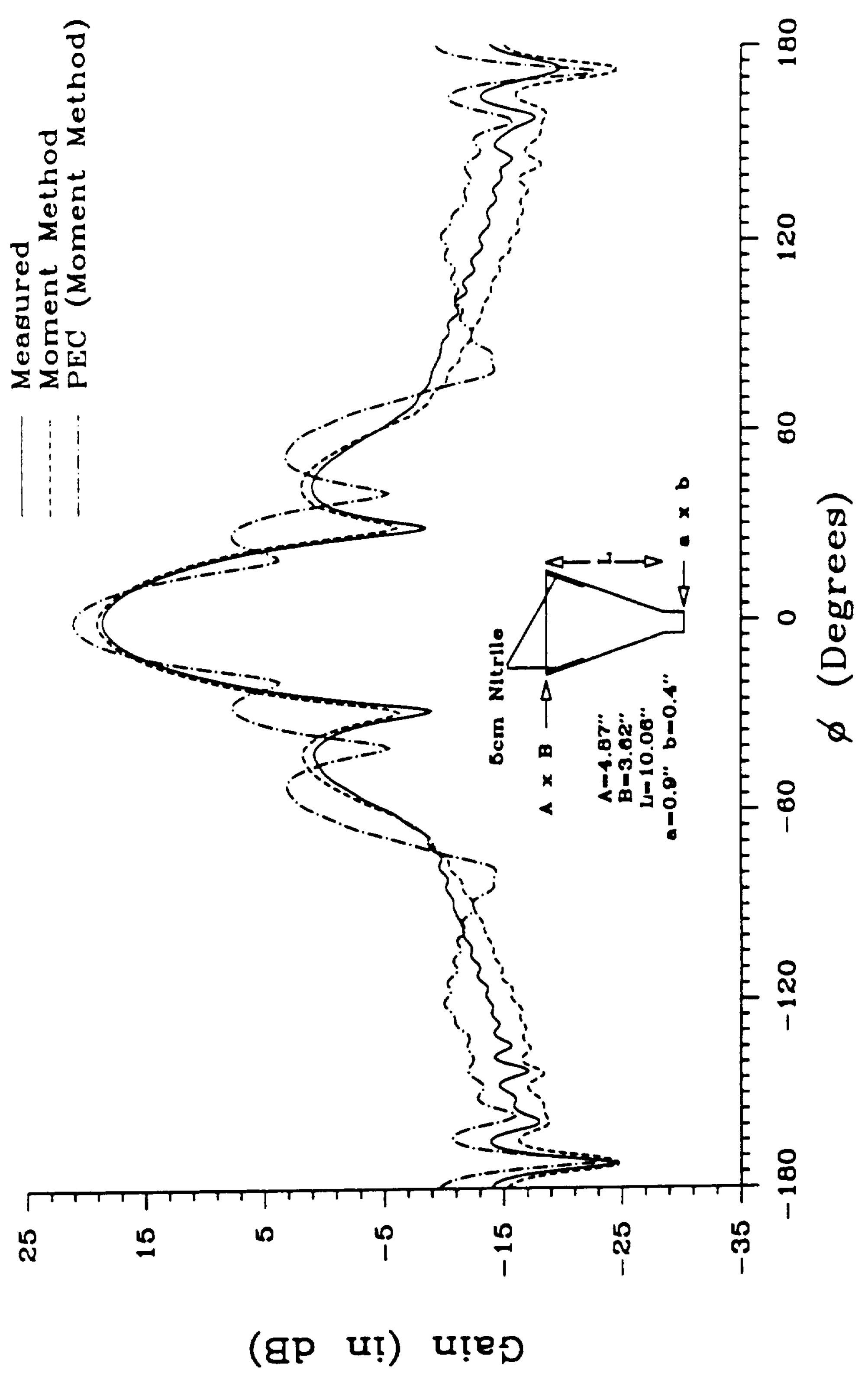

Fig. 2.4: Comparison of E-plane patterns for standard gain horn at 10 GHz with 5cm of lossy Nitrile material coating.

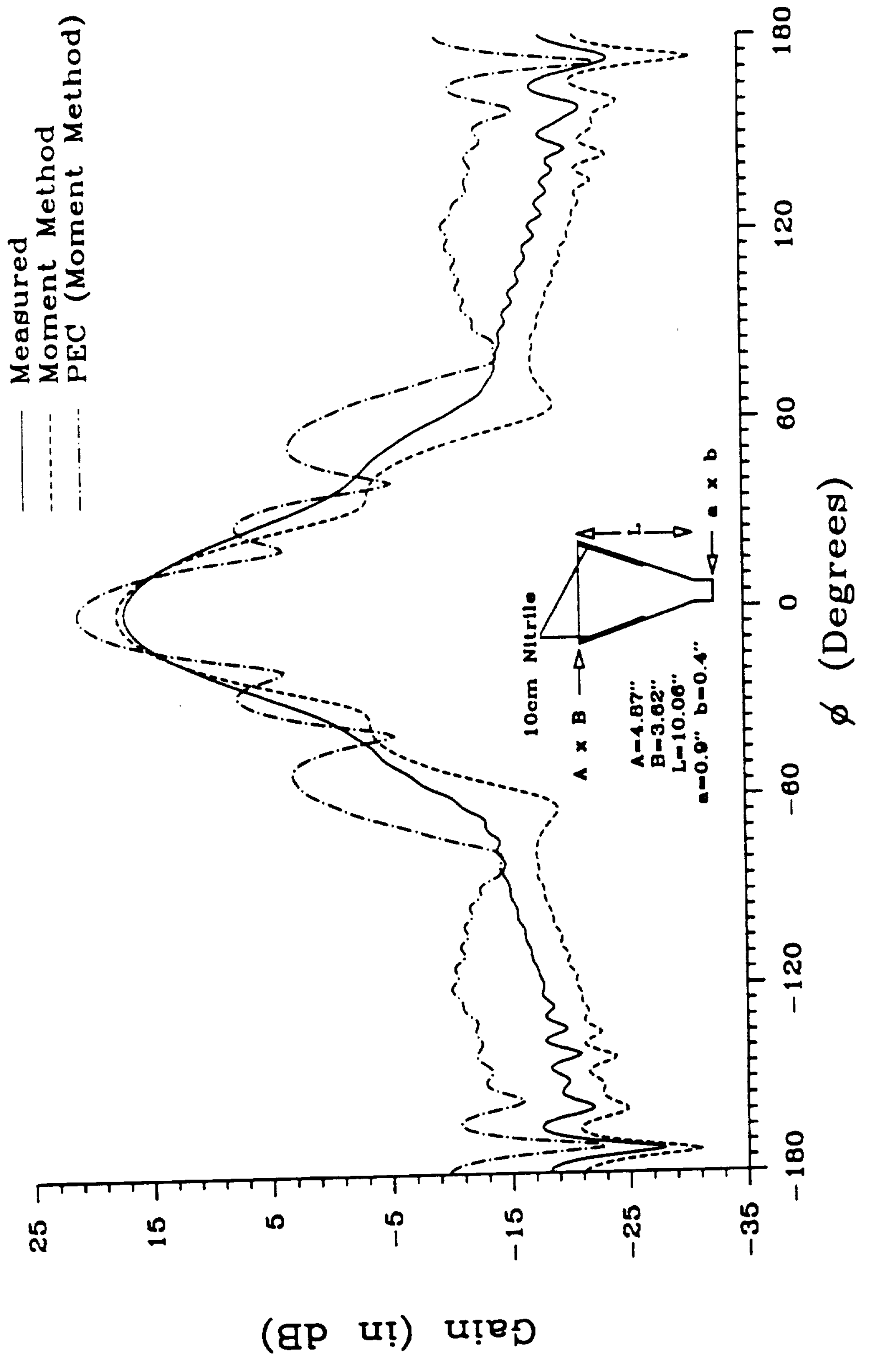

Fig. 2.5: Comparison of E-plane patterns for standard gain horn at 10 GHz with 10cm of lossy Nitrile material coating.

2.6 Conclusions

A full-wave, hybrid field integral equation method has been developed to analyze pyramidal horn antennas with lossy walls. The method can be used to analyze partially-coated pyramidal horn antennas. The presented technique achieves a reasonably good agreement between theoretical predictions and experimental data. This analytical technique represents the first full-wave technique for the analysis and design of horn antennas with lossy walls. Based on the the eigen mode analysis, guidelines are provided to design pyramidal horn antenna with lossy walls to shape the antenna pattern with minimal loss of the antenna gain.

CHAPTER 3

CONTOUR PATH FDTD ANALYSIS OF HORN ANTENNAS

3.1 Introduction

In addition to the full-wave Moment Method analysis, an alternative approach based on the Finite-Difference Time-Domain (FDTD) method was also applied in the analysis of pyramidal horn antennas with and without composite E-plane walls. Because of the flared surface of the pyramidal horns in the E- and H-planes, some augmentations of the basic FDTD method had to be made to model accurately and efficiently the surface of the horns.

Pyramidal horns with and without lossy walls were modeled by applying a contour path FDTD method to model the antenna flared surfaces. The idea behind the contour path approach is to distort the FDTD grid where it is only needed (near the antenna flared surface) and use the basic FDTD algorithm everywhere else in the numerical domain. Modified finite-difference equations are applied over the distorted grid. The equations are obtained by applying Maxwell's integral equations over the distorted part of the grid and making assumptions regarding the distribution of the electric and magnetic fields in the distorted grid.

In this report some familiarity with the basic FDTD method is assumed. The contour path FDTD method is then introduced based on the integral form of Maxwell's equations. This method is then used for the modeling of metallic pyramidal horn antennas. In the last part of the report, the contour path FDTD method is applied to the modeling of pyramidal horn antennas with lossy inner E-plane walls. In all cases, numerical results are compared with available measurements demonstrating the accuracy of the contour path FDTD approach.

3.2 FDTD Method Based on the Integral Form of Maxwell's Equations

Maxwell's equations can be written in integral form as

$$\oint_c \mathbf{H} \cdot d\mathbf{l} = \frac{\partial}{\partial t} \int\!\!\int_s \epsilon \mathbf{E} \cdot ds + \int\!\!\int_s \sigma \mathbf{E} \cdot ds \tag{3.1}$$

$$\oint_c \mathbf{E} \cdot \mathbf{dl} = -\frac{\partial}{\partial t} \int\!\!\int_s \mu \mathbf{H} \cdot ds - \int\!\!\int_s \rho \mathbf{H} \cdot ds \tag{3.2}$$

where (3.1) and (3.2) are referred to as Maxwell's integral equations as derived from Ampere's and Faraday's laws, respectively. **E** is the electric field in (V/m), **H** the magnetic field in (A/m), ϵ the electrical permittivity in (F/m), σ the electrical conductivity in (S/m), μ the magnetic permeability in (H/m), and ρ the magnetic resistivity in (Ω/m). The electrical permittivity ϵ and the magnetic permeability μ of composite materials are often provided in the form $\epsilon = \epsilon' - j\epsilon''$ and $\mu = \mu' - j\mu''$, respectively. The electrical permittivity and magnetic resistivity, σ and ρ, respectively, are then represented by:

$$\sigma = \omega\epsilon'' = \omega\epsilon_0\epsilon_r'', \tag{3.3}$$

$$\rho = \omega\mu'' = \omega\mu_0\mu_r'', \tag{3.4}$$

where ϵ_0 and μ_0 are the electrical permittivity and magnetic permeability of free space, respectively, and $\omega = 2\pi f$, where f is the frequency. Using the above two expressions the imaginary parts of electrical permittivity and magnetic permeability are lumped into σ and ρ, respectively.

Equations (3.1) and (3.2) are implemented in the conventional FDTD method over spatially orthogonal contours referred to as Ampere's and Faraday's contours, respectively [43]. Fig. 3.1 illustrates an example of Faraday's and Ampere's contours. Application of (3.1) and (3.2) over a cubic grid proceeds by assuming that the dimensions of the cell are small enough so that the electric and magnetic fields can be considered linear functions of position, and their values at the midpoints of each

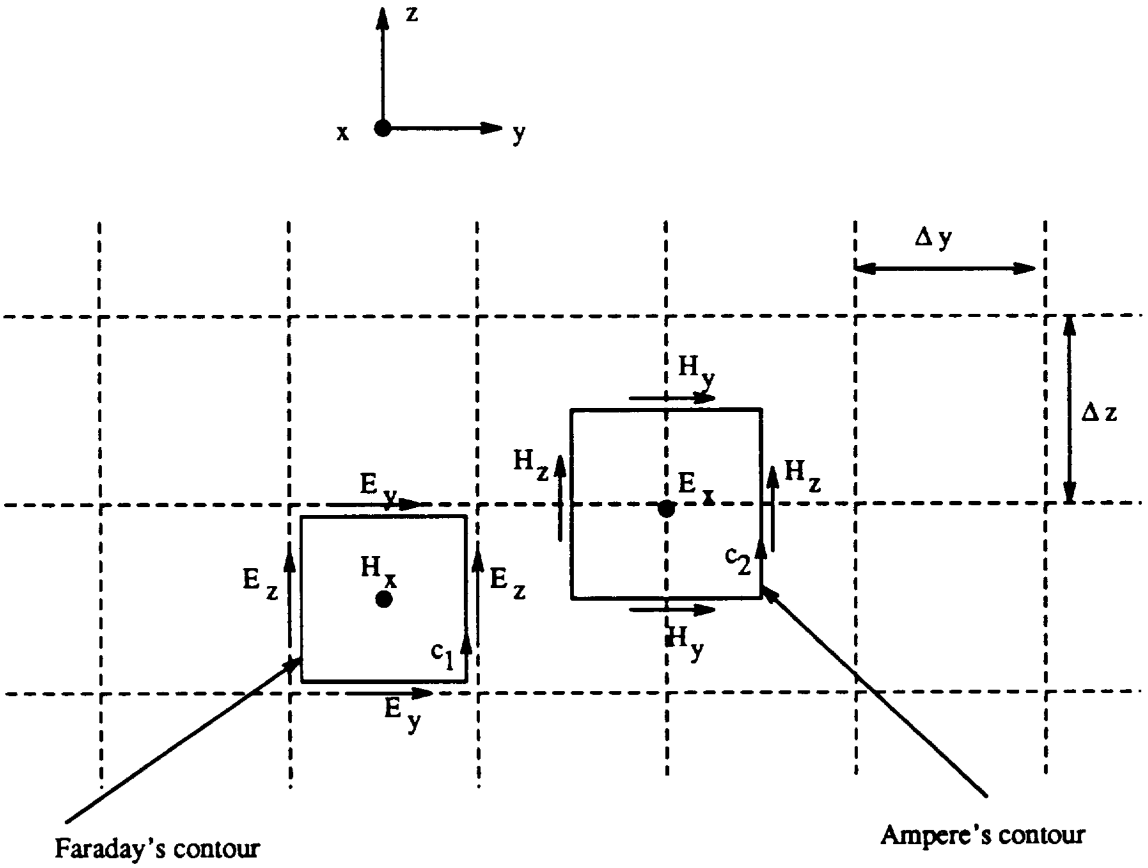

Fig. 3.1: Ampere's and Faraday's contours for implementing Maxwell's equations in integral form.

side of the contour equal to the average value of the field along that side. Under these assumptions, the resulting finite-difference equations for advancing the electric and magnetic fields are exactly the same as those obtained by applying Yee's algorithm [43]. This formulation is second-order accurate because the field components are assumed linear over the cells.

Consider the application of (3.2) over the Faraday's contour shown in Fig. 3.1. This results in

$$\oint_{c_1} \mathbf{E} \cdot d\mathbf{l} = -\frac{\partial}{\partial t} \int \int_{s_1} \mu H_x dy dz \tag{3.5}$$

where s_1 is the area enclosed by contour c_1. It was assumed that c_1 encloses a free-space cell for which $\rho = 0$. The positive direction for c_1 is taken in the counterclockwise direction in accordance with the right-hand rule. Evaluation of (3.5) proceeds by assuming that the dimensions of the cell are small enough so that the fields can be assumed linear functions of position. Consider first the left-hand side of (3.5) which involves four separate integrals, one integral per each side of contour c_1. Assume that the electric field distribution on the left side of contour c_1 to be of the form

$$E_z = E_z\left(i, j, k + \frac{1}{2}\right) + A \cdot z \tag{3.6}$$

where z is measured with respect to the center of the cell and A represents the slope of the electric field distribution. $E_z(i, j, k + \frac{1}{2})$ represents the value of the field at the center of the left side of contour c_1. The lower left corner of the cell is denoted as cell (i, j, k). Thus the contribution from the left side of c_1 is

$$\int_{-\frac{\Delta z}{2}}^{\frac{\Delta z}{2}} E_z dz = -\int_{-\frac{\Delta z}{2}}^{\frac{\Delta z}{2}} \left[E_z\left(i, j, k + \frac{1}{2}\right) + A \cdot z\right] dz = -E_z\left(i, j, k + \frac{1}{2}\right) \cdot \Delta z \tag{3.7}$$

where the negative sign was used because the electric field component points in the opposite direction (clockwise) from that of contour c_1. Similar integrations can be carried out over the rest of the contour to obtain:

$$\oint_{c_1} \mathbf{E} \cdot d\mathbf{l} \;=\; \left[E_z\left(i, j + 1, k + \frac{1}{2}\right) - E_z\left(i, j, k + \frac{1}{2}\right)\right] \Delta z$$

$$+ \quad \left[E_y\left(i,j+\frac{1}{2},k\right) - E_y\left(i,j+\frac{1}{2},k+1\right)\right]\Delta y \qquad (3.8)$$

The x component of the magnetic field must now be integrated over the area enclosed by contour c_1. Assume that H_x is linear within s_1 and its distribution over the cell can be expressed as:

$$H_x = H_x\left(i,j+\frac{1}{2},k+\frac{1}{2}\right) + B\cdot z + C\cdot y \qquad (3.9)$$

where y and z are measured with respect to the center of the cell. $H_x(i,j+\frac{1}{2},k+\frac{1}{2})$ represents the value of the field at the center of the cell and the constants B and C represent the slope of the magnetic field component in the z and y direction, respectively. Inserting (3.9) in (3.5) obtain:

$$\begin{aligned} -\frac{\partial}{\partial t}\int\int_{s_1}\mu H_x dydz &= -\frac{\partial}{\partial t}\int_{-\frac{\Delta z}{2}}^{\frac{\Delta z}{2}}\int_{-\frac{\Delta y}{2}}^{\frac{\Delta y}{2}}\mu\left[H_x\left(i,j+\frac{1}{2},k+\frac{1}{2}\right)+B\cdot z+C\cdot y\right]dydz \\ &= -\mu_0\frac{\partial}{\partial t}\left[H_x\left(i,j+\frac{1}{2},k+\frac{1}{2}\right)\right]\Delta z\Delta y \qquad (3.10)\end{aligned}$$

Note that the magnetic permeability is homogeneous within s_1 since a free-space cell was assumed. Its value is thus replaced by the free-space permeability μ_0. Equating (3.8) and (3.10) results in

$$\begin{aligned} &- \quad \mu_0\frac{\partial}{\partial t}\left[H_x\left(i,j+\frac{1}{2},k+\frac{1}{2}\right)\right]\Delta z\Delta y \\ &= \quad \left[E_z\left(i,j+1,k+\frac{1}{2}\right) - E_z\left(i,j,k+\frac{1}{2}\right)\right]\Delta z \\ &+ \quad \left[E_y\left(i,j+\frac{1}{2},k\right) - E_y\left(i,j+\frac{1}{2},k+1\right)\right]\Delta y \qquad (3.11)\end{aligned}$$

Applying central-difference approximation to the time derivative on the left-hand side at $t = n\Delta t$ and evaluating the right-hand side of the above equation also at $t = n\Delta t$ results in:

$$-\frac{\mu_0}{\Delta t}\left[H_x^{n+\frac{1}{2}}\left(i,j+\frac{1}{2},k+\frac{1}{2}\right) \quad - \quad H_x^{n-\frac{1}{2}}\left(i,j+\frac{1}{2},k+\frac{1}{2}\right)\right]\Delta z\Delta y$$

$$\begin{aligned} &= \left[E_z^n\left(i,j+1,k+\frac{1}{2}\right) - E_z^n\left(i,j,k+\frac{1}{2}\right)\right]\Delta z \\ &+ \left[E_y^n\left(i,j+\frac{1}{2},k\right) - E_y^n\left(i,j+\frac{1}{2},k+1\right)\right]\Delta y \end{aligned} \tag{3.12}$$

Rearranging and separating new and previous times, provides the equation for updating the x component of the magnetic field in a free-space cell as:

$$\begin{aligned} H_x^{n+\frac{1}{2}}\left(i,j+\frac{1}{2},k+\frac{1}{2}\right) &= H_x^{n-\frac{1}{2}}\left(i,j+\frac{1}{2},k+\frac{1}{2}\right) \\ &+ \frac{\Delta t}{\mu_0 \Delta y}\left[E_z^n\left(i,j,k+\frac{1}{2}\right) - E_z^n\left(i,j+1,k+\frac{1}{2}\right)\right] \\ &+ \frac{\Delta t}{\mu_0 \Delta z}\left[E_y^n\left(i,j+\frac{1}{2},k+1\right) - E_y^n\left(i,j+\frac{1}{2},k\right)\right] \end{aligned} \tag{3.13}$$

This equation is the same as the one obtained by applying central difference approximations to the differential form of Maxwell's equation.

Applying (3.1) over the Ampere's contour in Fig. 3.1 results in:

$$\oint_{c_2} \mathbf{H}\cdot d\mathbf{l} = \frac{\partial}{\partial t}\int\int_{s_2} \mu E_x dydz \tag{3.14}$$

where s_2 is the area enclosed by contour c_2. Assuming linear magnetic field components over the four sides of contour c_2 and performing the line integral in (3.14) results in:

$$\begin{aligned} \oint_{c_2} \mathbf{H}\cdot d\mathbf{l} &= \left[H_z\left(i+\frac{1}{2},j+\frac{1}{2},k\right) - H_z\left(i+\frac{1}{2},j-\frac{1}{2},k\right)\right]\Delta z \\ &+ \left[H_y\left(i+\frac{1}{2},j,k-\frac{1}{2}\right) - H_y\left(i+\frac{1}{2},j,k+\frac{1}{2}\right)\right]\Delta y \end{aligned} \tag{3.15}$$

Also, assuming linear distribution for the x component of electric field over s_2 and performing the surface integral in (3.14) results in:

$$\frac{\partial}{\partial t}\int\int_{s_2} \epsilon E_x dy dz = \frac{\partial}{\partial t}\left[\epsilon_0 E_x\left(i+\frac{1}{2},j,k\right)\right]\Delta y\Delta z \tag{3.16}$$

Equating (3.15) and (3.16) yields

$$\begin{aligned}
&\epsilon_0\frac{\partial}{\partial t}\left[E_x\left(i+\frac{1}{2},j,k\right)\right]\Delta z\Delta y\\
= &\left[H_z\left(i+\frac{1}{2},j+\frac{1}{2},k\right)-H_z\left(i+\frac{1}{2},j-\frac{1}{2},k\right)\right]\Delta z\\
+ &\left[H_y\left(i+\frac{1}{2},j,k-\frac{1}{2}\right)-H_y\left(i+\frac{1}{2},j,k+\frac{1}{2}\right)\right]\Delta y
\end{aligned} \tag{3.17}$$

Applying central-difference approximation to the time derivative on the left-hand side at $(n+1/2)\Delta t$ and evaluating the right-hand side at $(n+1/2)\Delta t$ also, rearranging and separating previous and new times results in:

$$\begin{aligned}
E_x^{n+1}\left(i+\frac{1}{2},j,k\right) = &\; E_x^n\left(i+\frac{1}{2},j,k\right)\\
+ &\;\frac{\Delta t}{\epsilon_0\Delta y}\left[H_z^{n+\frac{1}{2}}\left(i+\frac{1}{2},j+\frac{1}{2},k\right)-H_z^{n+\frac{1}{2}}\left(i+\frac{1}{2},j-\frac{1}{2},k\right)\right]\\
+ &\;\frac{\Delta t}{\epsilon_0\Delta z}\left[H_y^{n+\frac{1}{2}}\left(i+\frac{1}{2},j,k-\frac{1}{2}\right)-H_y^{n+\frac{1}{2}}\left(i+\frac{1}{2},j,k+\frac{1}{2}\right)\right]
\end{aligned} \tag{3.18}$$

The analysis in this section demonstrates that when the integral form of Maxwell's equations is applied over a cubic grid, equations similar to the ones obtained by applying central-difference approximations to the differential form of Maxwell's equations are obtained. Since the field components were assumed linear over the cells the resulting finite-difference equations are second-order accurate.

The integral equation formulation has several advantages over the differential equation formulation. One advantage is that it provides a better insight as to how the

FDTD method works. Also, the integral formulation approach allows the application of the FDTD method to a more general class of problems involving distorted grids or nonhomogeneous cells. Material discontinuities within the numerical domain can be modeled by applying the integral form of Maxwell's equation at the discontinuities.

One approach in FDTD applications, is to use modified equations where it is only necessary and to apply the standard FDTD algorithm everywhere else within the numerical domain. For example, if a curved surface is to be modeled, the grid is distorted near the surface of the curved structure only and retains its basic cubic form in the rest of the numerical domain. The same approach is applied when modeling sub cell features within the numerical domain, for example, very thin dielectric slabs or conducting structures coated with thin composite material. To implement correctly the required modifications, assumptions concerning the near field components over the distorted grid must be made.

3.3 Contour Path FDTD Method

Consider now applying the FDTD method to model a smoothly curved conducting surface such as the one shown in Fig. 3.2. As illustrated by the figure, the contours for updating the magnetic field components must be modified in such a way so as to conform with the curved conducting surface. For example, contour c_1 is stretched, whereas contour c_2 is shrunk to conform with the curved structure.

Update equations for the magnetic field components within the distorted contours are obtained by applying Maxwell's integral equations within the distorted contours. The electric and magnetic field components are assumed constant within the distorted contour segments. This assumption reduces the second-order accurate FDTD method to a first-order accurate method.

The contours for updating the electric fields are not modified. Where possible, the electric field components are updated by using normal Ampere's contours. If that is not possible the electric field components are declared unused field points. Par-

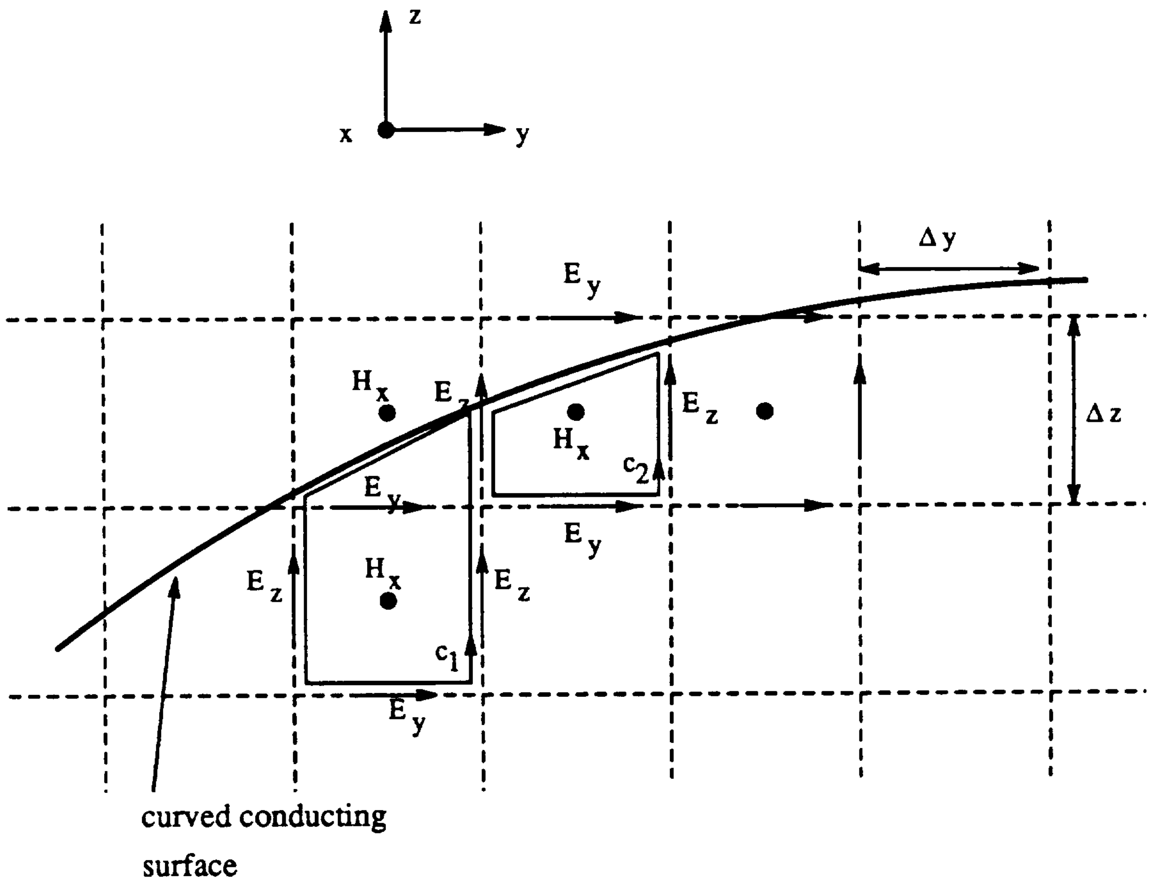

Fig. 3.2: Modified contours for implementing the contour path method.

ticularly, Ampere's contours that cross the conducting media interface are avoided. For example, the z component of electric field at the left side of contour c_2 cannot be updated normally because the magnetic field points are residing on opposite sides of the conducting surface. This field component is declared unused field point and it is not updated. To update the magnetic field point inside contour c_2, use is made of the lower z component of electric field on the left side of contour c_2, i.e., a near neighborhood approach is used when necessary.

The application of the contour path FDTD approach to model curved structures involves both cubic and distorted grids. The linearity of the field components is applied over the cubic part of the grid, while over the distorted part of the grid the field components are assumed constant. Therefore, the contour path FDTD approach reduces from second-order accurate to first-order accurate over the distorted part of the grid.

The assumptions of the contour path FDTD method can be summarized as follows [44], [45]:

1) The normally rectangular Faraday's contours surrounding the magnetic field components near a curved conducting surface are distorted so as to conform to the surface.

2) The magnetic field components are assumed to represent the average value of the magnetic field within the surface bounded by the distorted contour.

3) The tangential component of the electric field, E_{tan}, of the distorted contour at the conducting curved surface is zero.

4) Along the straight portions of the distorted contour the electric field components are assumed constant; where possible these fields are calculated using rectangular Ampere's contours from adjacent magnetic field components.

5) Calculations of Ampere's contours which cross the boundary of the curved conducting surface are avoided; the electric fields along the corresponding Faraday's contour segments, if needed, are obtained using a "near neighbor" approximation.

The concepts behind the contour path FDTD method will become more clear in the next chapter, where the method is applied in the modeling of pyramidal horn antennas with or without composite impedance walls. The grid is distorted to conform with the flared surface of the horn. The equations updating the magnetic fields within the distorted grid are derived based on the assumptions of the contour path FDTD method.

3.4 Contour Path FDTD Modeling of Horn Antennas

The pyramidal horns were also modeled using the contour path FDTD method. In this case the grid was distorted near the antenna surface to conform to its surface. The FDTD equations that update the fields near the surface were modified according to the distorted grid. These modifications were based on the assumptions stated in the previous section on the contour path FDTD method. Away from the antenna surface the cubic form of the grid was retained.

Fig. 3.3 illustrates how the grid can be distorted to model the pyramidal horn surface in the E-plane. The FDTD grid is represented using dashed lines. The dots in this figure represent the locations of the magnetic field points whose contours are affected by the presence of the inclined surface. In the E-plane cross section, in which the antenna flares in the y direction, the dots represent x directed magnetic field locations.

Consider the upper surface of the antenna in the E-plane cross section shown in Fig. 3.3. For flare angles less than 45°, three distinctive contours were identified. These three contours are shown in Fig. 3.4. In Fig. 3.4(a) the antenna surface cuts the grid below the location of the magnetic field point in the cell, in Fig. 3.4(b) above the location of the magnetic field point, and in Fig. 3.4(c) the antenna surface extends from a lower cell point to an upper cell point.

The equations for updating H_x in each case must be modified based on the assumptions of the contour path FDTD method. Assume that the electric field

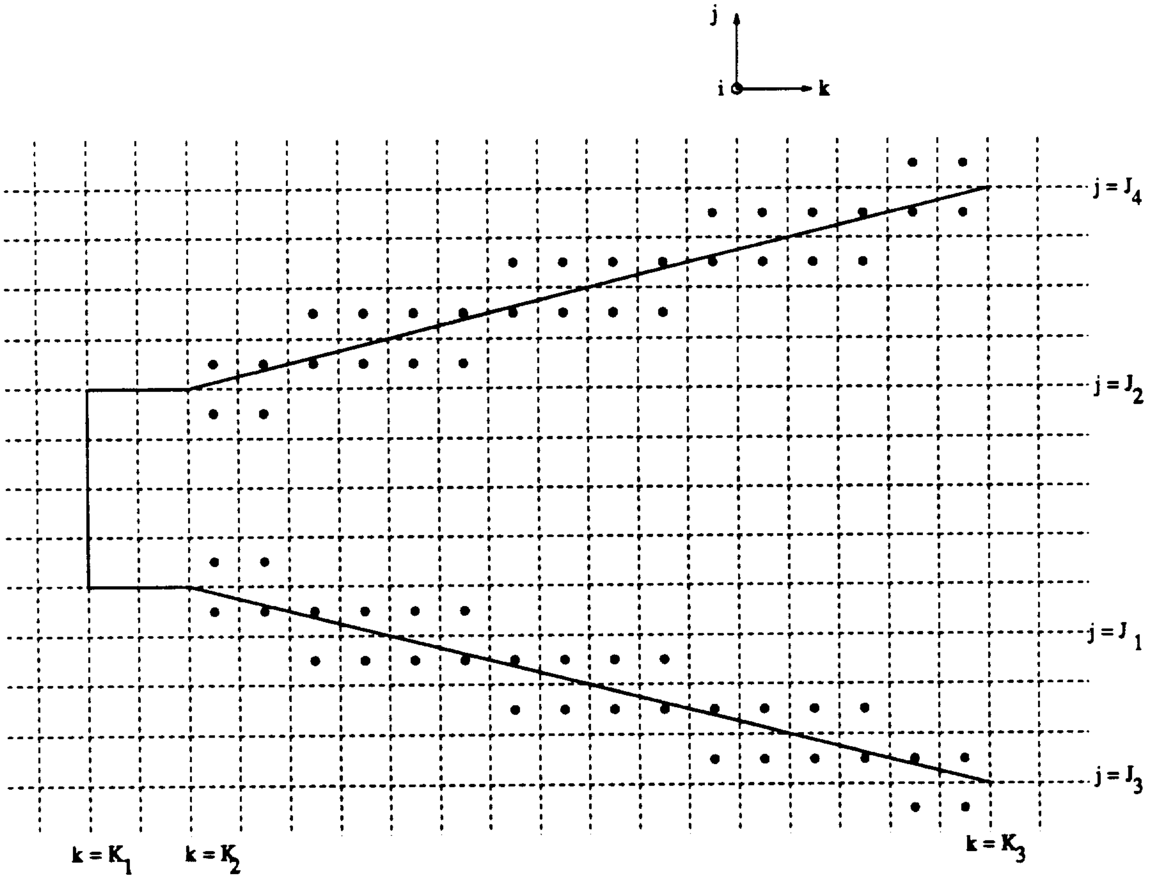

Fig. 3.3: Distorted Faraday's contours at the antenna surface in the E-plane cross section.

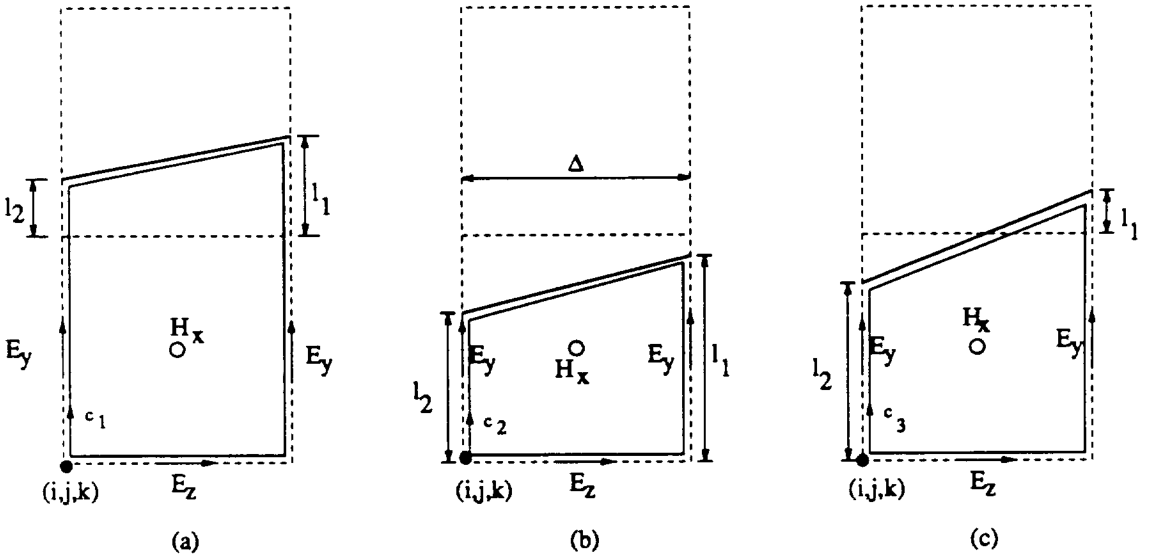

Fig. 3.4: Distorted Faraday's contours used to update H_x near the upper surface of the horn in the E-plane cross section.

components are constant on the sides of the distorted contours and that the magnetic field components are constant within the area enclosed by the distorted contour. Applying the integral form of Maxwell's equations over each contour shown in Fig. 3.4 results in the following update equations for the x component of the magnetic field, respectively:

$$\begin{aligned} H_x^{n+\frac{1}{2}}\left(i,j+\frac{1}{2},k+\frac{1}{2}\right) &= H_x^{n-\frac{1}{2}}\left(i,j+\tfrac{1}{2},k+\tfrac{1}{2}\right) \\ &+ \frac{\Delta t}{\mu_0}\cdot\frac{1}{A_1}\left[E_y^n\left(i,j+\frac{1}{2},k+1\right)\cdot(l_1+\Delta y)\right. \\ &- \left. E_y^n\left(i,j+\frac{1}{2},k\right)\cdot(l_2+\Delta y)+E_z^n\left(i,j,k+\frac{1}{2}\right)\cdot\Delta z\right] \end{aligned} \tag{3.19}$$

$$\begin{aligned} H_x^{n+\frac{1}{2}}\left(i,j+\frac{1}{2},k+\frac{1}{2}\right) &= H_x^{n-\frac{1}{2}}\left(i,j+\tfrac{1}{2},k+\tfrac{1}{2}\right) \\ &+ \frac{\Delta t}{\mu_0}\cdot\frac{1}{A_2}\left[E_y^n\left(i,j+\frac{1}{2},k+1\right)\cdot l_1\right. \\ &- \left. E_y^n\left(i,j+\frac{1}{2},k\right)\cdot l_2+E_z^n\left(i,j,k+\frac{1}{2}\right)\cdot\Delta z\right] \end{aligned} \tag{3.20}$$

$$\begin{aligned} H_x^{n+\frac{1}{2}}\left(i,j+\frac{1}{2},k+\frac{1}{2}\right) &= H_x^{n-\frac{1}{2}}\left(i,j+\tfrac{1}{2},k+\tfrac{1}{2}\right) \\ &+ \frac{\Delta t}{\mu_0}\cdot\frac{1}{A_3}\left[E_y^n\left(i,j+\frac{1}{2},k+1\right)\cdot(l_1+\Delta y)\right. \\ &- \left. E_y^n\left(i,j+\frac{1}{2},k\right)\cdot l_2+E_z^n\left(i,j,k+\frac{1}{2}\right)\cdot\Delta z\right] \end{aligned} \tag{3.21}$$

where A_1, A_2, and A_3 are the areas enclosed by the distorted Faraday's contours (a), (b), and (c) of Fig. 3.4, respectively. Note that the contribution from the tangential electric field component on the antenna conducting surface is zero, and therefore, not included in the above expressions.

Similar equations can be written for the distorted contours outside the upper surface of the horn antenna as well as for the lower surface. Distances l_1 and l_2 in each case (a), (b), and (c) are shown in Fig. 3.4, and they are estimated from the intersection points of the flared surface with the grid. Once l_1 and l_2 are estimated, then the areas A_1, A_2, and A_3 are determined for each case (a), (b) and (c), respectively.

Assuming a cubic grid, i.e., $\Delta x = \Delta y = \Delta z = \Delta$, define the following normalizations

$$l'_1 = \frac{l_1}{\Delta} \tag{3.22}$$

$$l'_2 = \frac{l_2}{\Delta} \tag{3.23}$$

$$A'_1 = \frac{A_1}{\Delta^2} \tag{3.24}$$

$$A'_2 = \frac{A_2}{\Delta^2} \tag{3.25}$$

$$A'_3 = \frac{A_3}{\Delta^2} \tag{3.26}$$

Inserting the above normalizations into (3.19)-(3.21) simplifies the modified equations for updating the x component of magnetic field as follows:

$$\begin{aligned} H_x^{n+\frac{1}{2}}\left(i,j+\frac{1}{2},k+\frac{1}{2}\right) &= H_x^{n-\frac{1}{2}}\left(i,j+\tfrac{1}{2},k+\tfrac{1}{2}\right) \\ &+ \frac{\Delta t}{\mu_0 \Delta}\cdot\frac{1}{A'_1}\left[E_y^n\left(i,j+\frac{1}{2},k+1\right)\cdot(l'_1+1.0)\right. \\ &- \left. E_y^n\left(i,j+\frac{1}{2},k\right)\cdot(l'_2+1.0)+E_z^n\left(i,j,k+\frac{1}{2}\right)\right] \end{aligned} \tag{3.27}$$

$$\begin{aligned}
H_x^{n+\frac{1}{2}}\left(i,j+\frac{1}{2},k+\frac{1}{2}\right) &= H_x^{n-\frac{1}{2}}\left(i,j+\tfrac{1}{2},k+\tfrac{1}{2}\right) \\
&+ \frac{\Delta t}{\mu_0\Delta}\cdot\frac{1}{A_2'}\left[E_y^n\left(i,j+\frac{1}{2},k+1\right)\cdot l_1'\right. \\
&- \left. E_y^n\left(i,j+\frac{1}{2},k\right)\cdot l_2' + E_z^n\left(i,j,k+\frac{1}{2}\right)\right]
\end{aligned} \tag{3.28}$$

$$\begin{aligned}
H_x^{n+\frac{1}{2}}\left(i,j+\frac{1}{2},k+\frac{1}{2}\right) &= H_x^{n-\frac{1}{2}}\left(i,j+\tfrac{1}{2},k+\tfrac{1}{2}\right) \\
&+ \frac{\Delta t}{\mu_0\Delta}\cdot\frac{1}{A_3'}\left[E_y^n\left(i,j+\frac{1}{2},k+1\right)\cdot(l_1'+1.0)\right. \\
&- \left. E_y^n\left(i,j+\frac{1}{2},k\right)\cdot l_2' + E_z^n\left(i,j,k+\frac{1}{2}\right)\right]
\end{aligned} \tag{3.29}$$

where the normalized areas for A_1', A_2', A_3' enclosed by the distorted contours (a), (b), and (c) of Fig. 3.4, respectively, are given by:

$$A_1' = 1.0 + \frac{l_1' + l_2'}{2} \tag{3.30}$$

$$A_2' = \frac{l_1' + l_2'}{2} \tag{3.31}$$

$$A_3' = \frac{1.0 + l_1' + l_2'}{2} \tag{3.32}$$

Finally, the normalized distances l_1' and l_2' can easily be determined from the intersection points of the antenna surface and the FDTD grid. The above formulation makes programming, of the modified equations for updating the magnetic field component, easy.

In certain cases the y directed electric field at the sides of the distorted contours can not be updated because Ampere's contours that cross the surface of the antenna must not be used. The algorithm identifies such cases and uses the most close y directed electric field in updating the x directed magnetic field. If the H_x field point is located within the antenna surface, the lower E_y field is taken. If the H_x field point is outside and on the upper surface of the antenna, then the upper E_y field is used. Similar reasoning is applied to the lower surface of the horn antenna.

For example, consider the distorted grid shown in Fig. 3.5. The electric field denoted as E_{y4} cannot be updated using the magnetic field points H_{x2} and H_{x3}, because they are at points on opposite sides of the antenna surface and Ampere's contours intersecting the boundary media should not be used. Therefore, the value of E_{y4} is not available. To update H_{x3}, instead of E_{y4} use the nearest E_y field collinear with it; i.e., E_{y2}. The resulting equation to update H_{x3} is

$$\begin{aligned} H_{x3}^{n+\frac{1}{2}}\left(i,j+\frac{1}{2},k+\frac{1}{2}\right) &= H_{x3}^{n-\frac{1}{2}}\left(i,j+\tfrac{1}{2},k+\tfrac{1}{2}\right) \\ &+ \frac{\Delta t}{\mu_0}\cdot\frac{1}{A_2}\left[E_{y6}^{n}\left(i,j+\frac{1}{2},k+1\right)\cdot l_1\right. \\ &- \left. E_{y2}^{n}\left(i,j+\frac{1}{2},k\right)\cdot l_2 + E_{z_2}^{n}\left(i,j,k+\frac{1}{2}\right)\cdot\Delta z\right] \end{aligned} \tag{3.33}$$

Because the value of E_{y4} is not available, the z component of the magnetic field half-cell above the position of E_{y4} cannot be updated. Both the E_{y4} and H_z field components are declared unused field points and are not updated by the FDTD algorithm. However, the H_z magnetic field component is needed to update the field points E_{x1} and E_{x2}. These field components are also assumed to have zero value (tangential field components close to a conducting surface), and they are not updated by the FDTD algorithm.

Other instances where some of the distorted Faraday's contours create field points that should neither be advanced nor be used by the algorithm to advance other neighboring field points are now examined. Examples of unused field points can easily be identified in case (c) of Fig. 3.4. In this case the field points corresponding

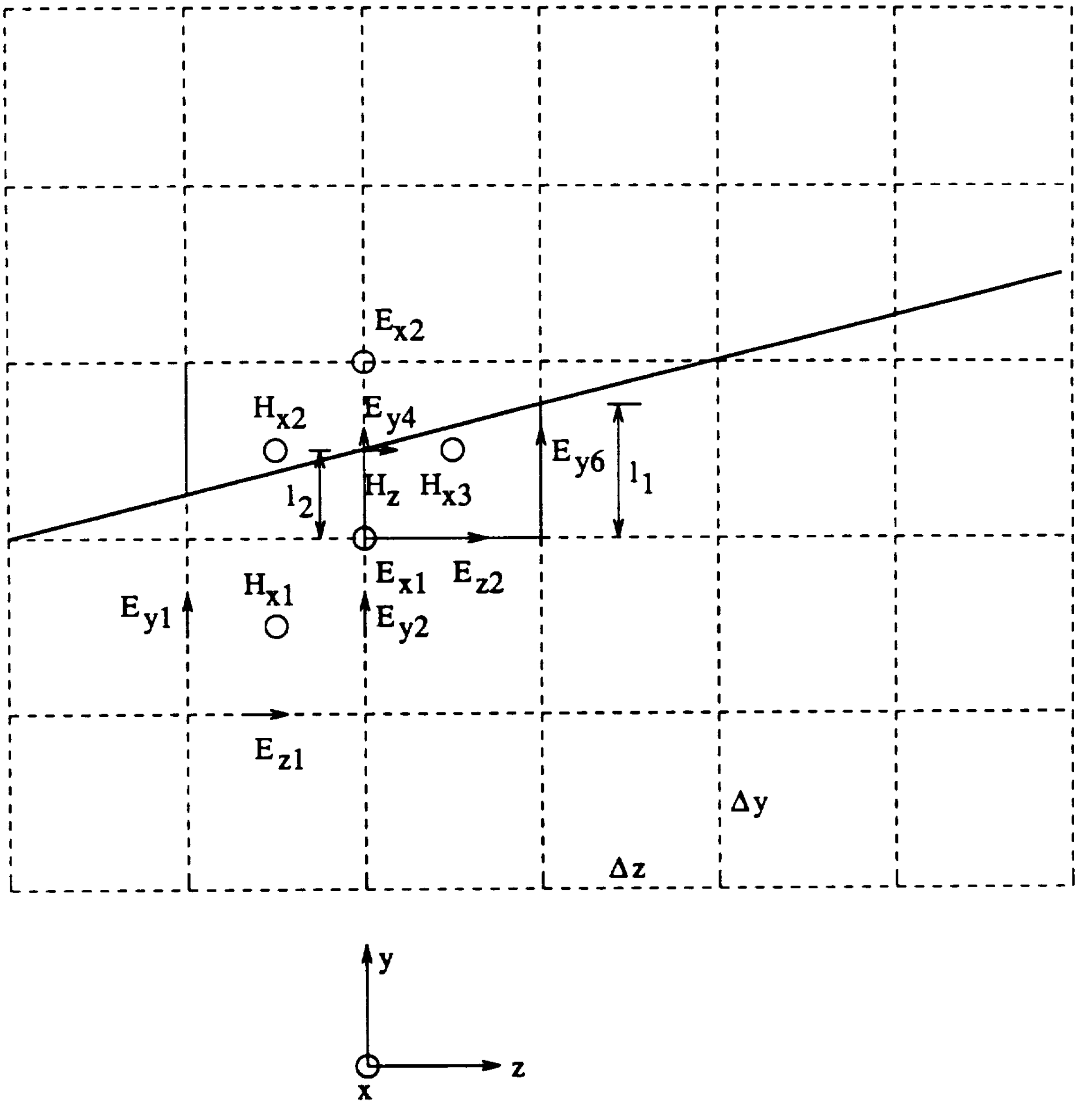

Fig. 3.5: Example of modified updating at locations where an Ampere's contour cannot be used because it is crossing media boundaries.

to the y-directed magnetic field and the z-directed electric field, where the inclined surface intersects the upper side of the unit cell, must be declared unused field points.

The corresponding modifications in the H-plane cross section of the pyramidal horn are obtained by following a similar procedure as that applied in the E-plane cross section. Fig. 3.6 illustrates how the grid can be distorted to model the pyramidal horn surface in the H-plane. The dots in this case represent the locations of the y directed magnetic field components whose contours must be modified to conform to the antenna surface. The equations updating the y-directed magnetic field points in the distorted grid are obtained by applying Maxwell's integral equations over the distorted grid. The procedure is similar to that applied for the E-plane cross section and will not be discussed further.

Slightly different modifications are required for the z component of the magnetic field, compared to those applied for the x and y components of the magnetic field. Fig. 3.7 illustrates how the grid can be distorted to model the pyramidal horn in the xy plane. The dots in this figure represent the locations of the magnetic field points whose contours are affected by the presence of the antenna conducting surface.

Consider the upper surface of the antenna shown in Fig. 3.7. There are two possible ways that the antenna surface can cut the grid. First, the antenna surface can cut the grid below the magnetic field point and second, above the magnetic field point. These two cases are illustrated in Fig. 3.8. The equations for updating H_z in each case must be modified by applying the contour path method over the distorted contours. Normalizing the distance l_1, shown in Fig. 3.8, with respect to the cell size and applying the integral form of Maxwell's second equation (3.2) over the two distorted contours, respectively, results in:

$$\begin{aligned} H_z^{n+\frac{1}{2}}\left(i+\frac{1}{2}, j+\frac{1}{2}, k\right) &= H_z^{n-\frac{1}{2}}\left(i+\tfrac{1}{2}, j+\tfrac{1}{2}, k\right) \\ &+ \frac{\Delta t}{\mu_0 \Delta} \cdot \frac{1}{A_1'} \left[E_y^n\left(i, j+\frac{1}{2}, k\right) \cdot (l_1' + 1.0)\right. \end{aligned}$$

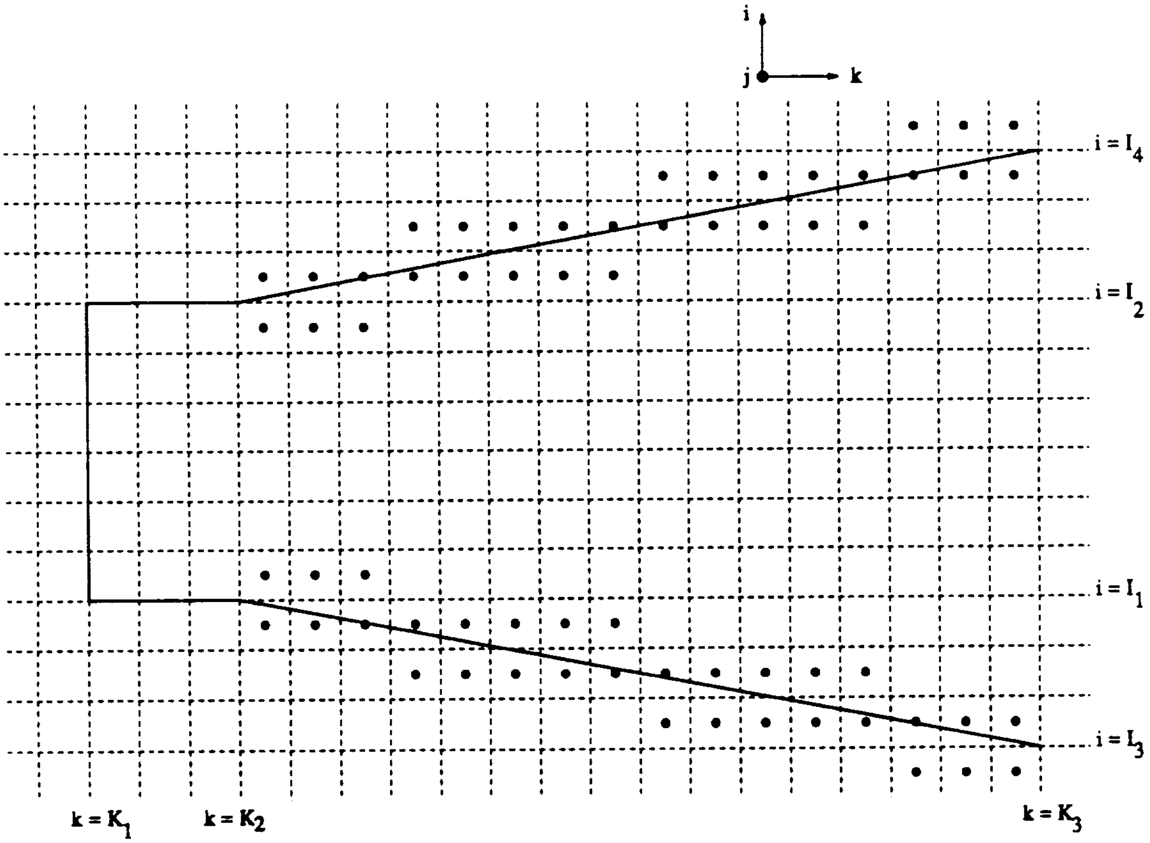

Fig. 3.6: Distorted Faraday's contours at the antenna surface in the H-plane cross section.

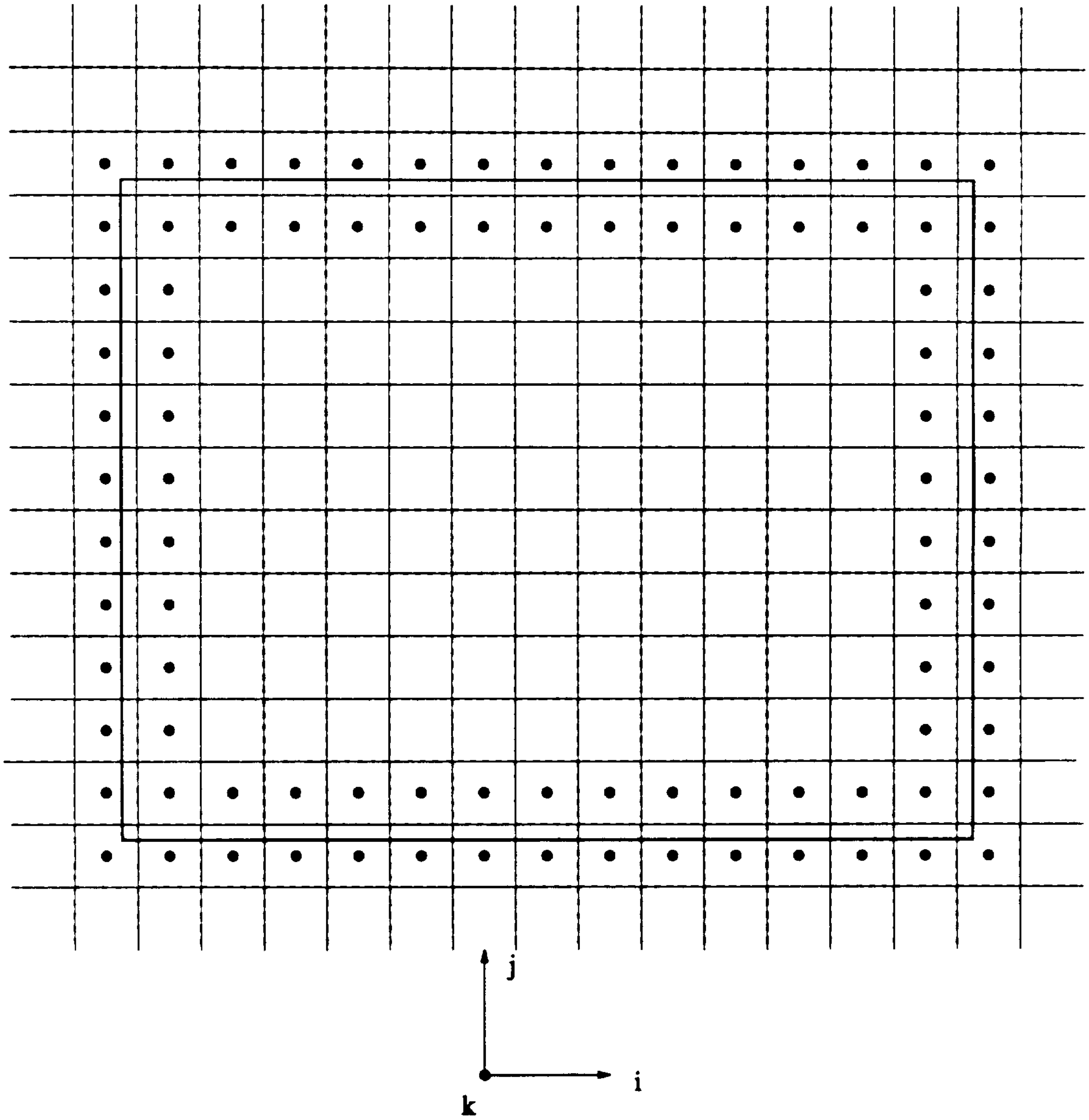

Fig. 3.7: Distorted Faraday's contours at the antenna surface in the xy plane.

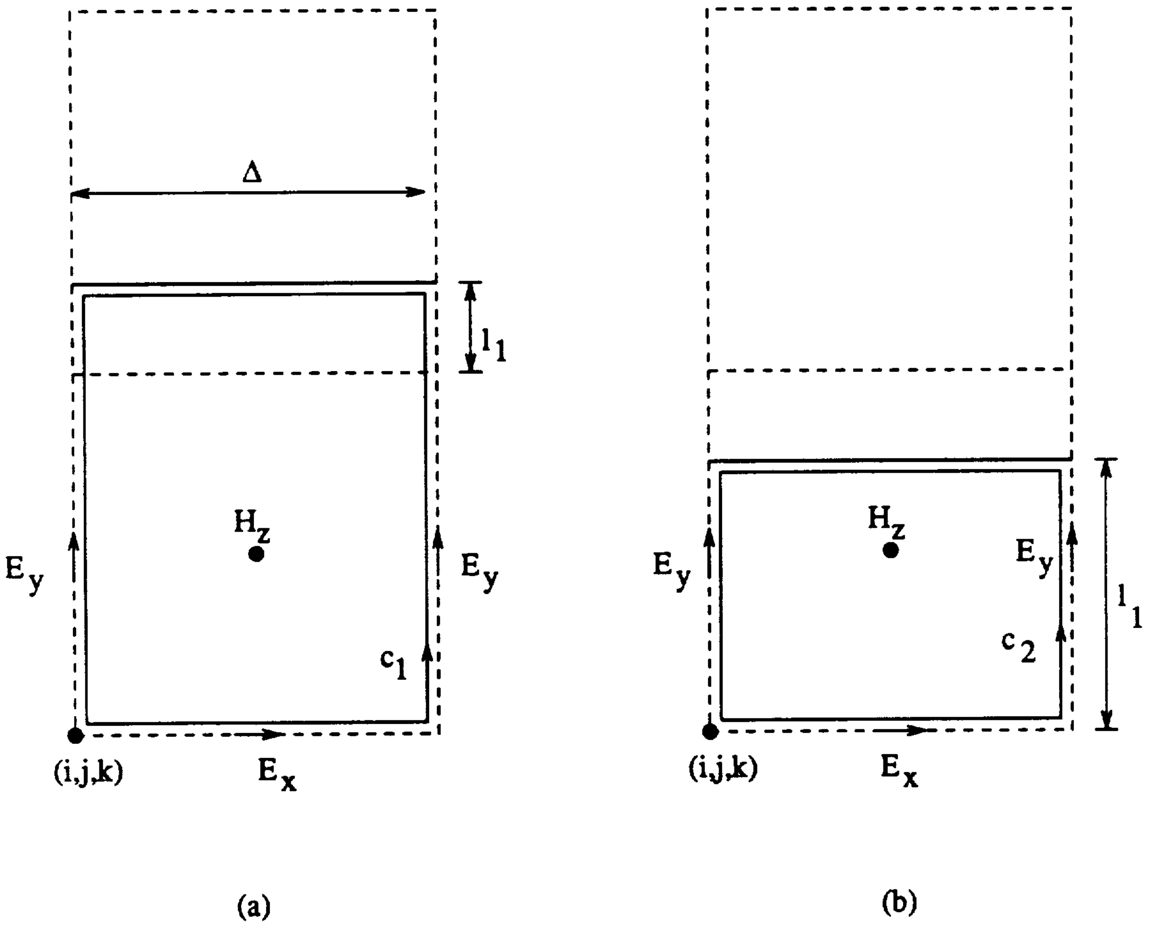

Fig. 3.8: Distorted Faraday's contours used to update H_z near the upper surface of the horn in the xy plane.

$$- \quad E_y^n\left(i+1, j+\frac{1}{2}, k\right) \cdot (l_1' + 1.0) - E_x^n\left(i+\frac{1}{2}, j, k\right)\Big]$$

(3.34)

$$\begin{aligned} H_z^{n+\frac{1}{2}}\left(i+\frac{1}{2}, j+\frac{1}{2}, k\right) &= H_z^{n-\frac{1}{2}}\left(i+\tfrac{1}{2}, j+\tfrac{1}{2}, k\right) \\ &+ \frac{\Delta t}{\mu_0 \Delta} \cdot \frac{1}{A_2'}\Big[E_y^n\left(i, j+\frac{1}{2}, k\right) \cdot (l_1') \\ &- E_y^n\left(i+1, j+\frac{1}{2}, k\right) \cdot (l_1') - E_x^n\left(i+\frac{1}{2}, j, k\right)\Big] \end{aligned}$$

(3.35)

where the normalized areas A_1' and A_2' enclosed by the distorted contours c_1 and c_2 of Fig. 3.8, respectively, are given by:

$$A_1' = 1.0 + l_1' \tag{3.36}$$

$$A_2' = l_1' \tag{3.37}$$

The normalized distances l_1' and l_2' can easily be determined from the intersection points of the antenna surface and the FDTD grid.

3.5 Input Power, Radiated Power and Radiation Efficiency

In analyzing the pyramidal horn, it is assumed that it is fed by a rectangular waveguide operating in the dominant TE_{10} mode whose tangential electric field at the aperture is represented by

$$E_y(x, y, z) = E_0 \sin(\frac{\pi}{a}x)\sin(\omega t - \beta_z z) \tag{3.38}$$

where $0 \leq x \leq a$ and $0 \leq y \leq b$. The constant β_z represents the waveguide propagation constant. At the reference feed plane $\beta_z z$ was set equal to zero.

Using this feeding scheme, the input power to the horn was estimated by integrating the input power density over the waveguide cross section, and it is givenn by

$$P_{10}^{input} = \frac{1}{2} E_0^2 \left(\frac{\beta_z}{\omega\mu_0}\right)\left(\frac{ab}{2}\right) = \frac{E_0^2}{4}\frac{ab}{\eta_0}\sqrt{1-\left(\frac{\lambda}{2a}\right)^2} \tag{3.39}$$

where $\eta_0 = 120\pi$ is the free-space impedance.

The far zone E_θ and E_ϕ electric fields are obtained from the FDTD code through a near-to-far-field transformation. The E-plane gain pattern was calculated using

$$G_E\left(\theta, \phi = 90^\circ\right) = 4\pi \frac{\frac{E_\theta^2(\theta,\phi=90^\circ)}{2\eta_0}}{P_{10}^{input}} \tag{3.40}$$

Similarly, the H-plane gain pattern was calculated using

$$G_H\left(\theta, \phi = 0^\circ\right) = 4\pi \frac{\frac{E_\phi^2(\theta,\phi=0^\circ)}{2\eta_0}}{P_{10}^{input}} \tag{3.41}$$

The antenna radiated power was estimated by integrating the far zone fields over a sphere and it is represented by [4]:

$$P^{rad} = \int_0^{\pi}\int_0^{2\pi} U(\theta,\phi)\sin\theta d\theta d\phi \tag{3.42}$$

where $U(\theta, \phi)$ is the intensity given by

$$U(\theta,\phi) = \frac{1}{2\eta_0}[\mid E_\theta(\theta,\phi)\mid^2 + \mid E_\phi(\theta,\phi)\mid^2] \tag{3.43}$$

One important design parameter of pyramidal horns with lossy materials on the E-plane walls is the power loss or the antenna efficiency calculated using

$$\eta = \frac{P^{rad}}{P_{10}^{input}} \tag{3.44}$$

3.6 Numerical Results

The 20-dB standard gain pyramidal horn antenna was also analyzed using the contour path FDTD. Figs. 3.9 and 3.10 compare the computed E- and H-plane gain patterns, respectively, of the pyramidal horn with measurements. As illustrated by both figures, there is very good agreement between the computed and measured results over a dynamic range of 60 dB. The computed gain patterns agree very well with the measured ones when a standard cell size of $\lambda/12$ was used (0.1″). The overall FDTD grid required for this problem was 76 × 60 × 142 cells. This simulation was run for 40 cycles to reach steady state and took about 2,500 seconds on an IBM-RISC/6000 mainframe computer.

The antenna radiation efficiency was estimated by integrating the far-zone fields to obtain the radiated power. The amplitude of the y-directed electric field was set equal to $E_0 = 1$ V/m, producing a reference power of $P_{10} = 0.116226 \times 10^{-6}$ Watts. By estimating the antenna far fields and then integrating them (1° steps) the radiated power was estimated $P_{rad} = 0.115077 \times 10^{-6}$ Watts. The corresponding radiation efficiency was $\eta = 0.99011 \simeq 99.0\%$. Therefore, most of the input power is radiated except for a small portion which is reflected back into the antenna.

To examine further the accuracy of the contour path FDTD method, it was also used in the analysis of the two square aperture pyramidal horn antennas. The aperture dimensions of the smaller square horn were 5″ × 5″, whereas the aperture dimensions of the larger one was 7″ × 7″.

In Figs. 3.11 and 3.12 the computed antenna gain patterns are compared with measurements for the smaller square aperture horn. As illustrated by both figures, there is very good agreement between the computed and measured antenna gain patterns. The frequency of operation was 10 GHz. The aperture of the horn was 5″ × 5″ whereas the waveguide aperture was of standard X-band dimensions; i.e., 0.9″ × 0.4″. The transition length from the waveguide aperture to the horn aperture, L, was 10.5″. A grid size of 0.1″ was used, i.e., the waveguide was 9 × 4 cells whereas the horn aperture was 50 × 50 cells. The distance from the waveguide transition to the horn aperture was 105 cells.

The computer code was run for 40 cycles to reach steady state, on an IBM-RISC/6000 computer. The CPU time was 4,200 seconds for obtaining the E- and

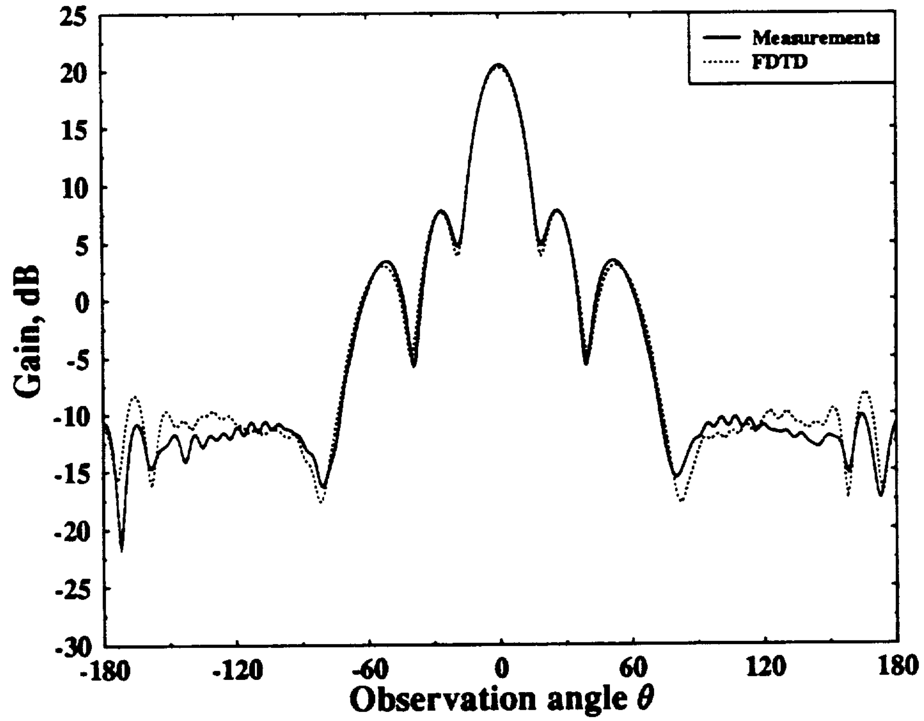

Fig. 3.9: E-plane gain of a 20-dB pyramidal horn at 10.0 GHz (A = 4.87″, B = 3.62″, L = 10.06″, a = 0.9″ and b = 0.4″).

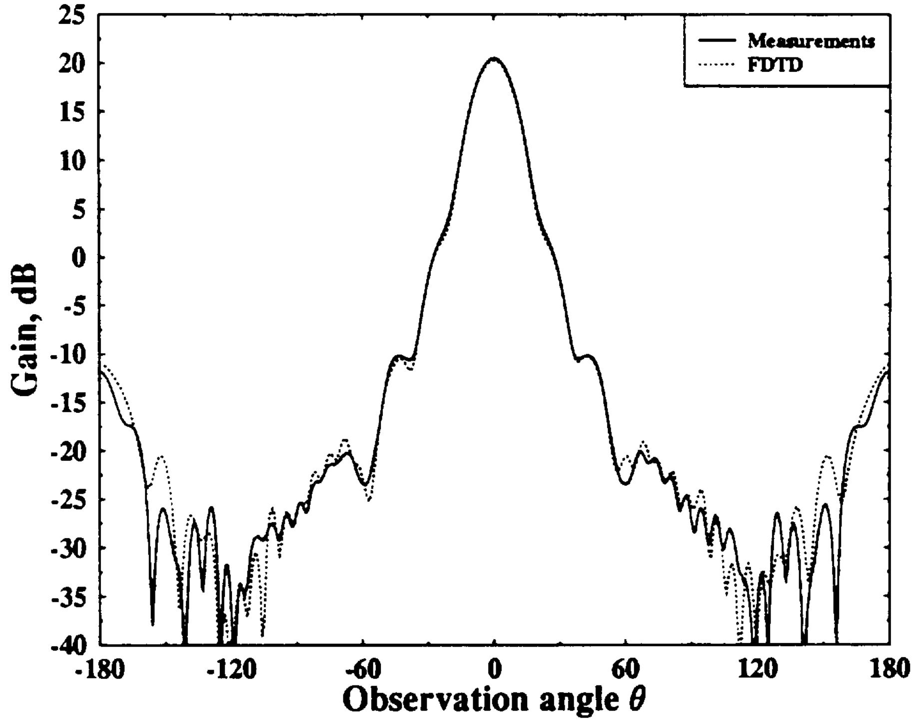

Fig. 3.10: H-plane gain of a 20-dB pyramidal horn at 10.0 GHz.

H-plane patterns over 360° at 1° steps. An overall grid size of $78 \times 78 \times 144$ cells was used for this simulation.

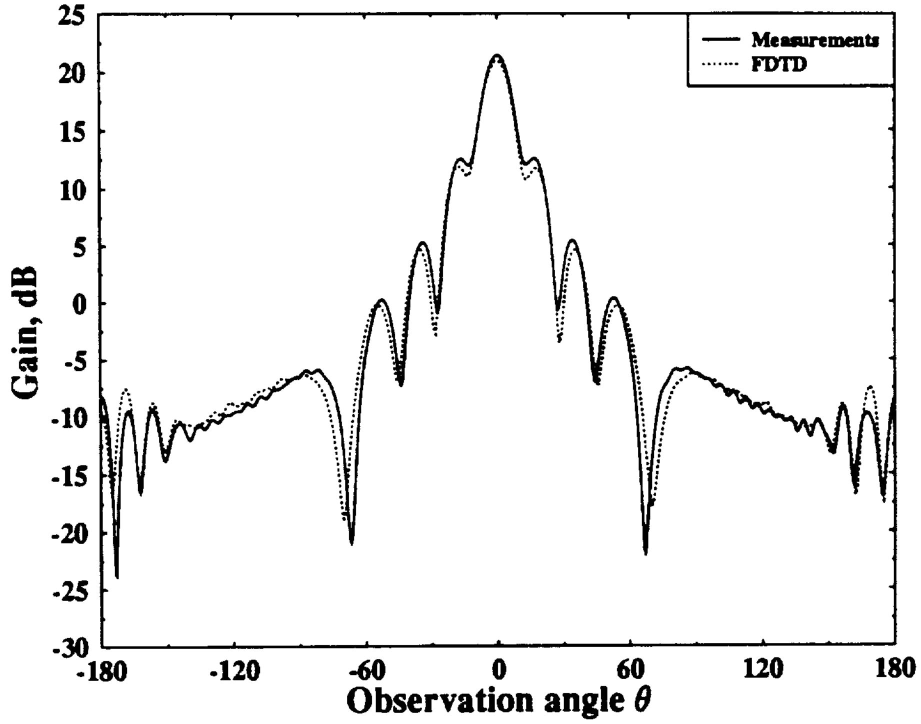

Fig. 3.11: E-plane gain of a square aperture pyramidal horn at 10.0 GHz (A = 5″, B = 5″, L = 10.5″, a = 0.9″ and b = 0.4″).

Finally, the contour path FDTD method was used to model a larger square aperture antenna. The aperture of the horn was 7″ × 7″ whereas the waveguide aperture was of standard X-band dimensions; i.e., 0.9″ × 0.4″. The transition length from the waveguide aperture to the horn aperture, L, was 12.2″. The frequency of operation was 10 GHz. A grid size of 0.1″ was used; i.e., the waveguide was 9×4 cells whereas the horn aperture was 70×70 cells. The distance from the waveguide transition to the horn aperture was 122 cells. Figs. 3.13 and 3.14 compare the computed E-

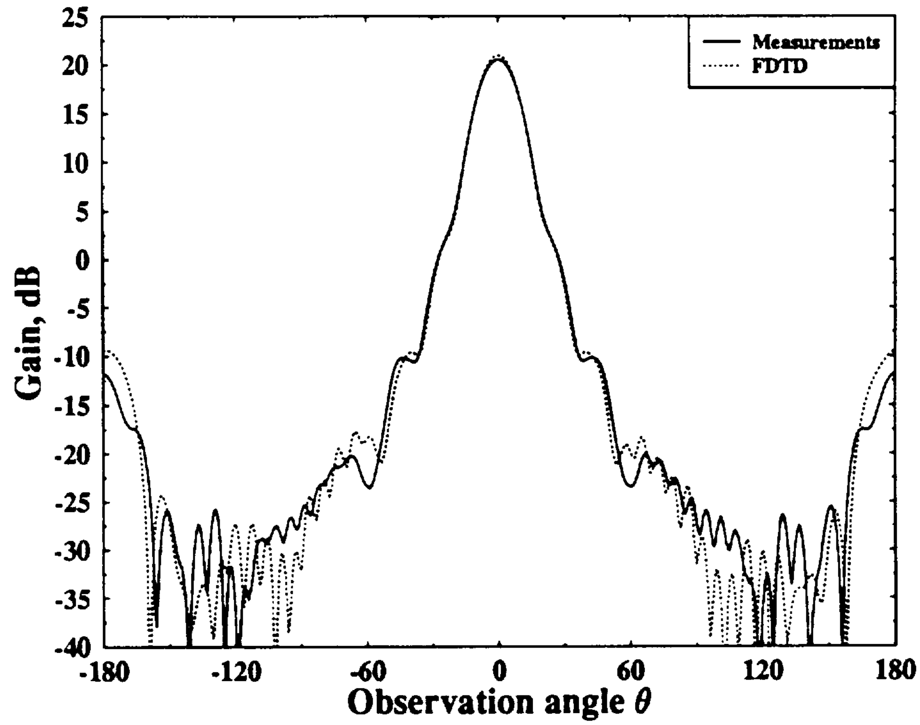

Fig. 3.12: H-plane gain of a square aperture pyramidal horn at 10.0 GHz (A = 5″, B = 5″, L = 10.5″, a = 0.9″ and b = 0.4″).

and H-plane patterns of the square aperture horn antenna with measurements. As illustrated in the figures, there is very good agreement between the computations and the measurements.

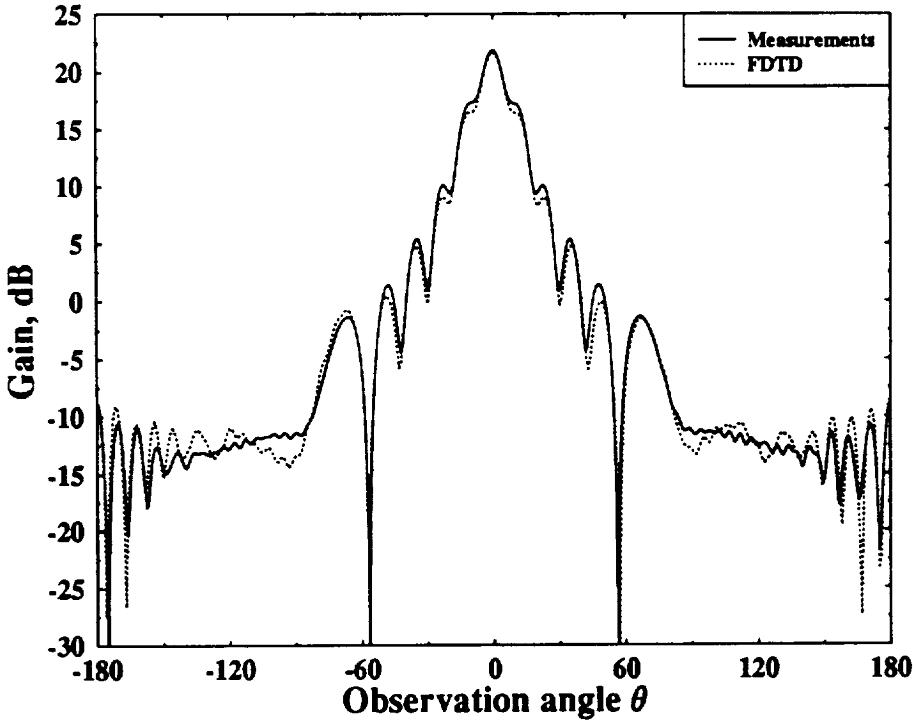

Fig. 3.13: E-plane gain of a square aperture pyramidal horn at 10.0 GHz (A = 7″, B = 7″, L = 12.2″, a = 0.9″ and b = 0.4″).

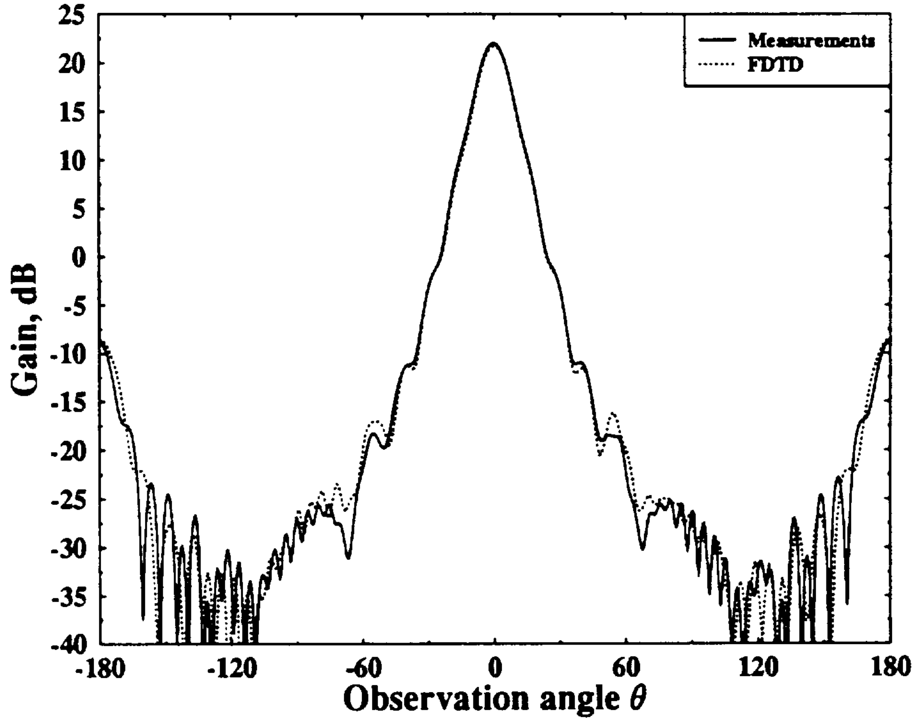

Fig. 3.14: H-plane gain of a square aperture pyramidal horn at 10.0 GHz (A = 7″, B = 7″, L = 12.2″, a = 0.9″ and b = 0.4″).

CHAPTER 4

CONTOUR PATH FDTD ANALYSIS OF HORN ANTENNAS WITH LOSSY WALLS

4.1 Introduction

An advantage in the use of the FDTD method is its ability to model thin composite materials such as coated conductors with dielectric and/or magnetic material slabs. Such materials find applications in electrically and/or magnetically coated aperture antennas [40].

Analysis of three-dimensional material plates, with and without conductor backing, was presented using an open surface integral formulation by Newman and Schrote [46]. Min *et al.* [47] presented an efficient formulation, using the integral equation approach, to solve scattering problems from two-dimensional conducting bodies coated with magnetic materials. A hybrid finite element method has been applied to conducting cylinders coated with inhomogeneous dielectric and/or magnetic materials [48], and a combined finite element-boundary integral formulation was developed for the solution of two-dimensional scattering problems coated with lossy material [49].

The thin coating of composite material presents a computational problem when the FDTD method is applied, because the method demands that the grid size used is at least equal to the thickness of the coating. When the grid size of the FDTD method is chosen very small, the corresponding time step increment must also be comparatively small to satisfy the stability condition [50]. This requirement results in an inefficient way to solve the problem.

A modified FDTD formulation based on the integral representation of Maxwell's equations was applied to thin dielectric structures [51]. The structures involved thin dielectric slabs (with and without conductor backing) and conductor-backed dielectric slabs that contain thin dielectric cracks in the coating. The dielectric coatings considered were lossless, i.e., the conductivity of the dielectric material was zero. Using a slightly different approach, Maloney *et al.* [52] applied the FDTD method to thin dielectric slabs with finite conductivity.

In this research project, the formulations presented in [51] and [52] were extended to model pyramidal horns coated either partially or totally by a thin, lossy, magnetic material coating. The magnetic coating, having both electric and magnetic loss, was applied in the E-plane upper and lower walls of the antenna for pattern control purposes. Depending on the extent to which the E-plane wall is coated, nearly symmetric E-plane and H-plane antenna patterns can be obtained. The approach followed to include the effect of such lossy materials is described next.

4.2 Contour Path FDTD Modeling of Horn Antennas With Lossy Walls

The geometry of a partially coated pyramidal horn antenna is shown in Fig. 4.1, along with the E- and H-plane cross sections of the antenna. As illustrated by the figure, the upper and lower walls of the horn are coated on the inside with a thin composite material having both electric and magnetic losses. Since the composite material is placed only on the upper and lower E-plane walls, modifications in the FDTD update equations must be made only in the E-plane cross section of the antenna. Also, since the composites are placed only on the inside part of the pyramidal horn, the equations for the inside part only, need further modifications (from the metallic case). The modifications made for the outside part of the metallic horn apply for this case also.

Fig. 4.2 shows how the presence of a thin composite material on the inside of the upper and lower E-plane walls modifies the FDTD grid. The composite material section is shown as the shaded region. This region covers, in some cells, the magnetic field points, shown as dots, whose contours are affected by the presence of both the antenna surface and the lossy material. Like in the metallic horn case, three distinctive contours were identified. These contours, for the upper section of the wall, including the lossy coating, are shown in Fig. 4.3.

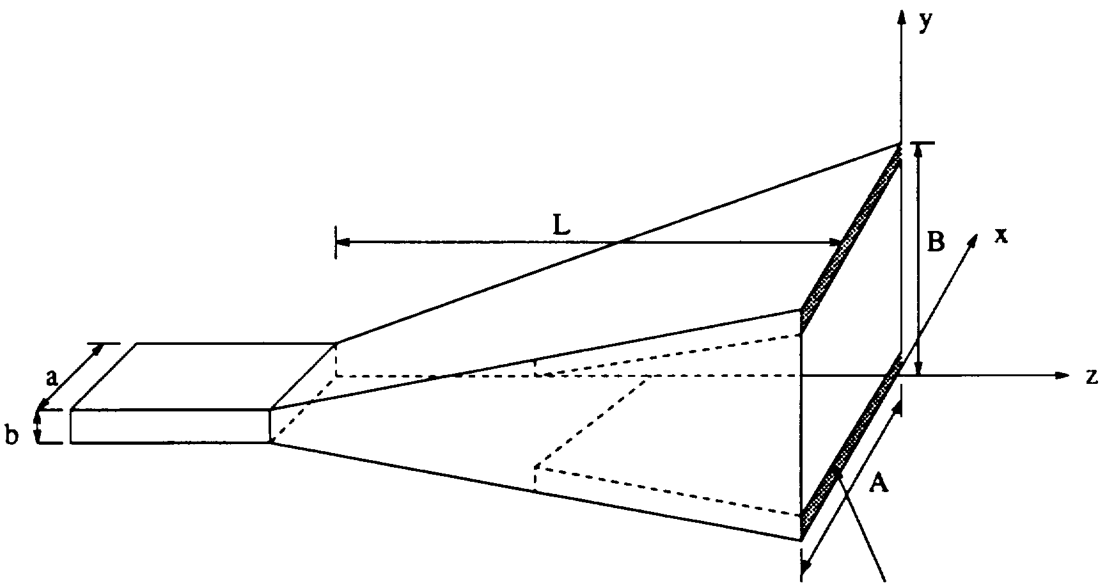

a) Pyramidal horn

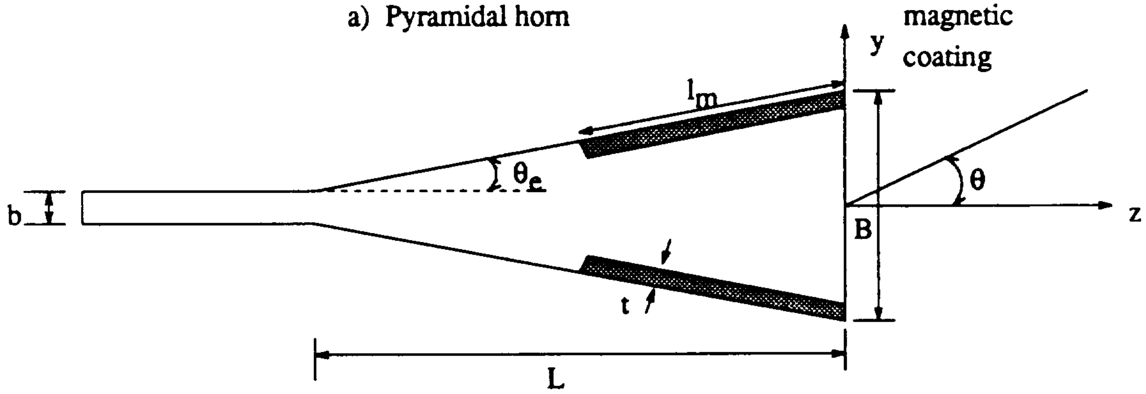

b) E-plane view

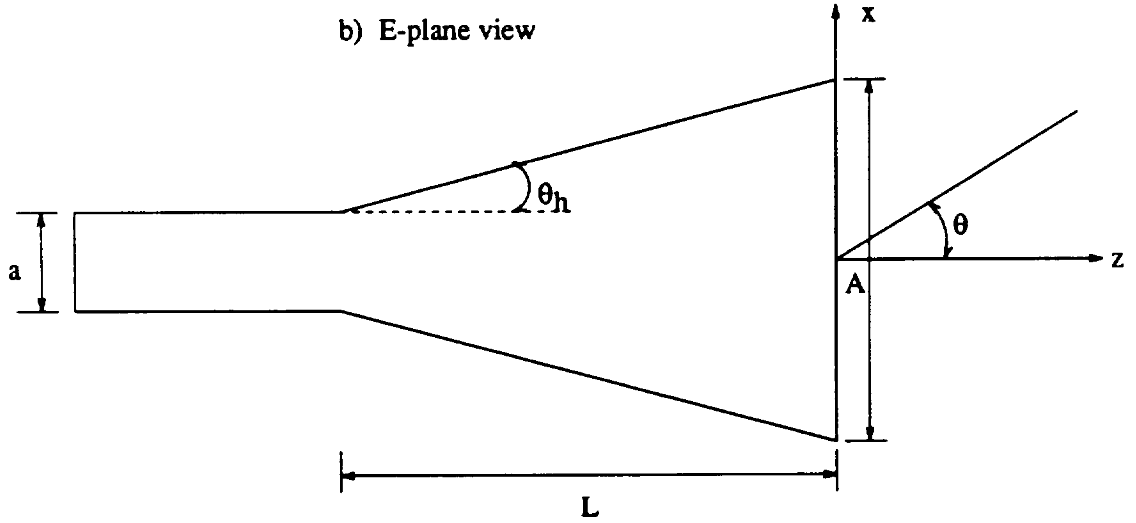

c) H-plane view

Fig. 4.1: Geometry of partially coated pyramidal horn antenna.

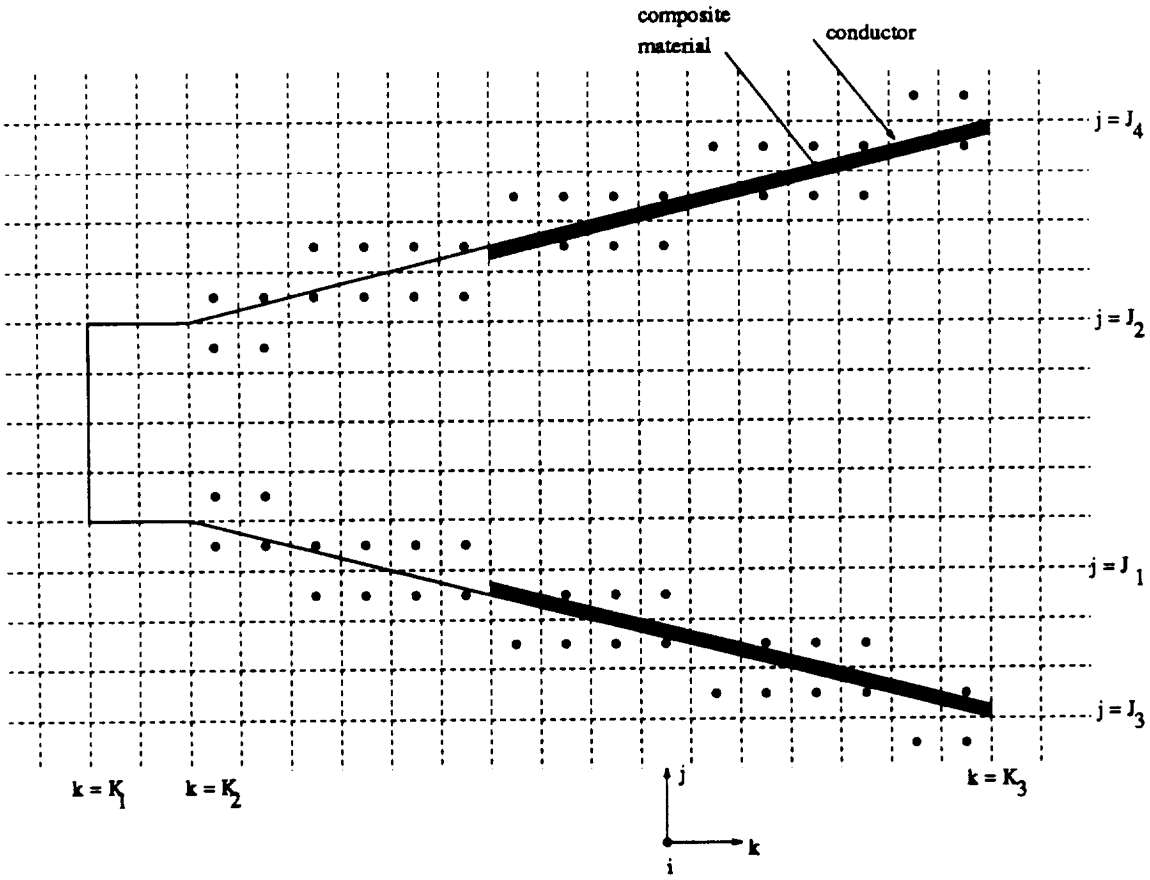

Fig. 4.2: Distorted Faraday's contours in the E-plane with the presence of a thin section of composite material.

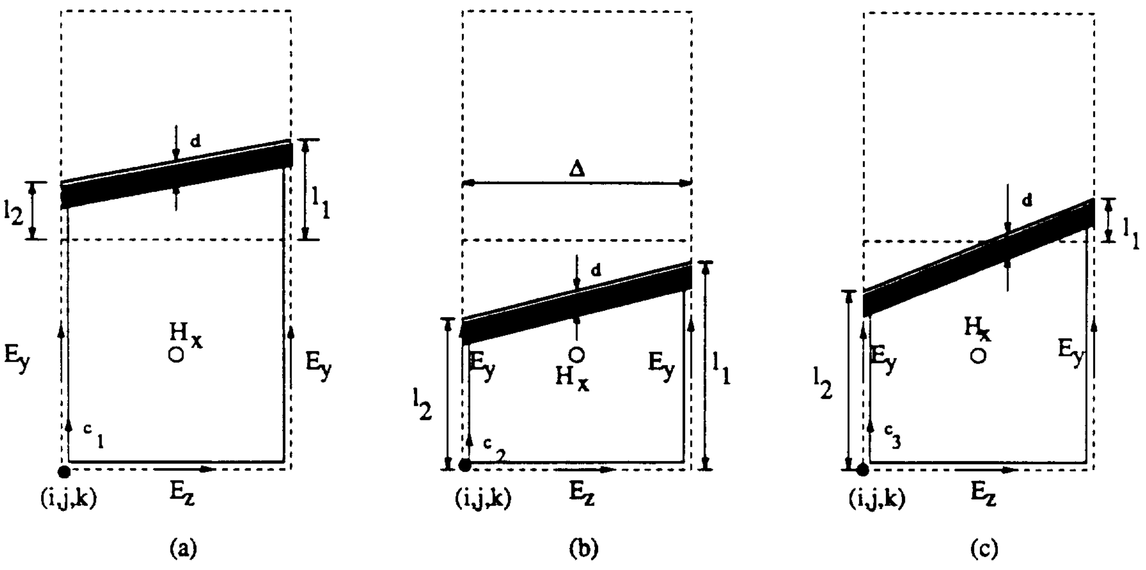

Fig. 4.3: Distorted Faraday's contours used to update H_x in the presence of a thin section of composite material.

The distorted contours shown in Fig. 4.3 are partly-filled with lossy material and partly-filled with free space. The derivation of the modified equations for this case will involve applying Maxwell's integral equations within the distorted contours. Since the contours are partly-filled with material and partly-filled with free space, care must be taken to ensure that the physics of the problem is not violated.

Consider first deriving the equation for updating the magnetic field component in case (a) of Fig. 4.3. Applying (3.2) over the distorted contour results in:

$$\oint_{c_1} \mathbf{E} \cdot d\mathbf{l} = -\frac{\partial}{\partial t} \int\int_{s_1} \mu \mathbf{H} \cdot d\mathbf{s} - \int\int_{s_1} \rho \mathbf{H} \cdot d\mathbf{s} \tag{4.1}$$

where c_1 is the contour shown in Fig. 4.3(a) and s_1 is the total area enclosed by the contour c_1. Splitting the integrations over the material part and free-space part of the cell and taking the partial derivative with respect to time within the integral, the following equation is obtained:

$$\oint_{c_1} \mathbf{E} \cdot d\mathbf{l} = -\int\int_{s_1 - s_{m_1}} \mu \frac{\partial \mathbf{H}}{\partial t} \cdot d\mathbf{s} - \int\int_{s_1 - s_{m_1}} \rho \mathbf{H} \cdot d\mathbf{s}$$

$$- \iint_{s_{m_1}} \mu \frac{\partial \mathbf{H}}{\partial t} \cdot ds - \iint_{s_{m_1}} \rho \mathbf{H} \cdot ds \tag{4.2}$$

where $s_1 - s_{m_1}$ denotes the free-space part of the cell and s_{m_1} the material part. The next step is to perform the integrations in (4.2) based on the assumptions of the contour path method.

First, consider normalizing distances l_1, l_2 and d with respect to the cell size Δ and the total distorted area s_1 and material area s_{m_1} with respect to the square cell area Δ^2. This normalization results into corresponding primed variables l'_1, l'_2, d', s'_1 and s'_{m_1}. Using these normalizations, the total normalized area of the cell is given by:

$$s'_1 = 1 + \frac{l'_1 + l'_2}{2} \tag{4.3}$$

whereas, the composite material area is given by:

$$s'_{m_1} = d' \tag{4.4}$$

Assuming constant magnetic field distribution for H_x within the distorted cell and integrating the right-hand side of (4.2) results in:

$$\begin{aligned} \oint_{c_1} \mathbf{E} \cdot d\mathbf{l} &= -\mu_0 \left(1 + \frac{l'_1 + l'_2}{2} - d'\right) \Delta^2 \frac{\partial H_x}{\partial t} - \mu_0 \mu_r d' \Delta^2 \frac{\partial H_x}{\partial t} - \rho d' \Delta^2 H_x \\ &= -\mu_0 \left(1 + \frac{l'_1 + l'_2}{2} - d' + \mu_r d'\right) \Delta^2 \frac{\partial H_x}{\partial t} - \rho d' \Delta^2 H_x \end{aligned} \tag{4.5}$$

where μ_r and ρ are the relative dielectric permeability and magnetic resistivity, respectively, of the composite material. Introducing the parameters

$$\overline{\mu_r} = 1 + \frac{l'_1 + l'_2}{2} - d' + \mu_r d' \tag{4.6}$$

$$\overline{\rho} = \rho d' \tag{4.7}$$

simplifies (4.5) into the following:

$$\oint_{c_1} \mathbf{E} \cdot d\mathbf{l} = -\mu_0 \overline{\mu_r} \Delta^2 \frac{\partial H_x}{\partial t} - \overline{\rho} \Delta^2 H_x \tag{4.8}$$

To perform the line integral of the electric field on the left-hand side of the above equation, assumptions must be made about the distribution of the y component of electric field in the free-space part and material part of the distorted contour. Since E_y is not a tangential field, at the air/material interface its value undergoes a discontinuity. This discontinuity must be included in the model.

The assumed distribution of the y component of electric field on the right-side of contour c_1 is shown in Fig. 4.4. The discontinuity of the field at the air/material interface is shown in this figure. E_{yin} represents the value of the field within the material and E_{yout} the corresponding value in the free-space part of the cell.

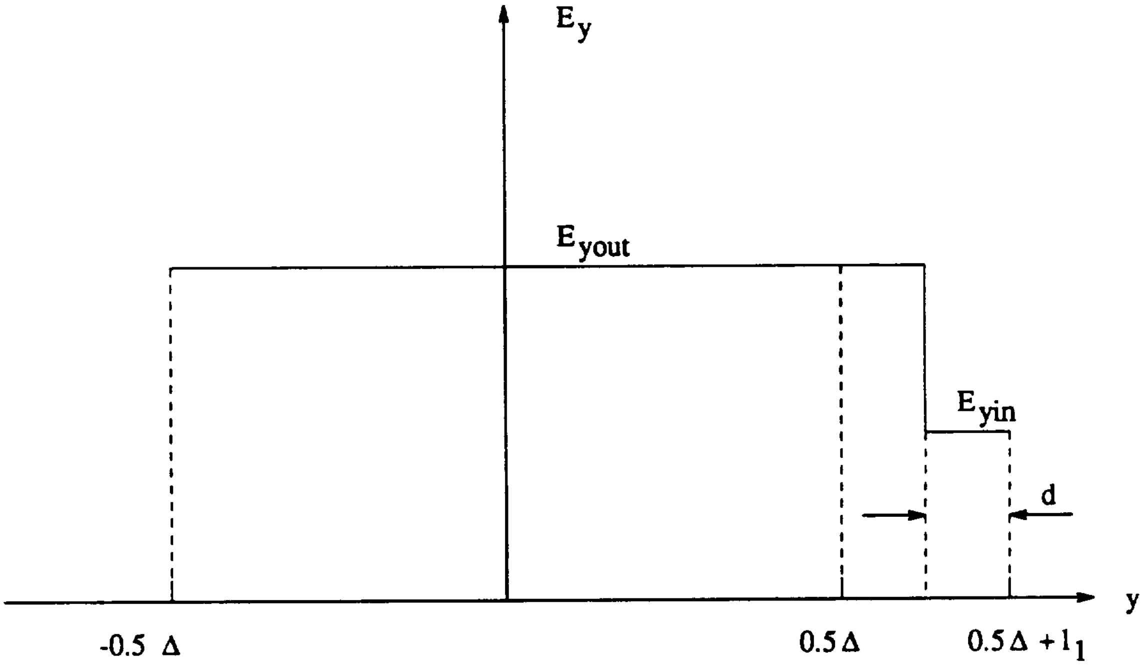

Fig. 4.4: Assumed distribution for E_y on the right side of contour c_1.

To perform the line integral of the y component of electric field over the right side of the cell, E_{yin} and E_{yout} must be integrated over the material section and free-space section of the right side of contour c_1, respectively. A similar treatment must be made for the left side of the contour c_1. The line integral of the electric field around contour c_1 can be expressed as:

$$\begin{aligned}\oint_{c_1} \mathbf{E} \cdot d\mathbf{l} &= \left[E_{yout}\left(1.0 + l_2' - d'\right)\Delta + E_{yin} d'\Delta\right]_{left} \\ &- \left[E_{yout}\left(1.0 + l_1' - d'\right)\Delta + E_{yin} d'\Delta\right]_{right} - \left[E_z\Delta\right]_{bottom} \qquad (4.9)\end{aligned}$$

This formulation requires two values for the y-directed electric field component, one in the free-space part of the distorted cell and one in the material part. The FDTD algorithm however, updates only one value for the y-directed electric field on each side of the distorted contour. This updated field component is either assumed in free space and hence the free space parameters are used in updating it or in the material and hence the material parameters are used in updating it. To alleviate the problem of having to estimate two electric field values for the y component of electric field in the distorted part of the contour, the value of the electric field inside the material is related by the corresponding value in free space using a boundary condition relation at the air/material interface.

The additional expression required to relate E_{yin} and E_{yout} is obtained by applying the boundary condition for E_{yin} and E_{yout} at the air/material interface. Note that in applying the boundary condition, the inclination of the interface must be accounted for. The additional expression from applying the boundary condition for E_y at the air/material interface can shown to be:

$$E_{yin} = \frac{\sqrt{\epsilon_r^2 \sin^2\theta_e + \cos^2\theta_e}}{\epsilon_r} E_{yout} \qquad (4.10)$$

where ϵ_r is the relative dielectric permittivity of the material and θ_e is the E-plane flare angle of the antenna.

Assuming that both the y-directed electric field components in contour c_1 are updated in free-space medium, the line integral of the electric field is evaluated by replacing the value of E_{yin} in terms of the E_{yout} in (4.9). This substitution results in the following expression for the line integral:

$$\oint_{C_1} \mathbf{E}\cdot d\mathbf{l} = \left[E_y l'_{2eff}\Delta\right]_{left} - \left[E_y l'_{1eff}\Delta\right]_{right} - \left[E_z\Delta\right]_{bottom} \tag{4.11}$$

where E_{yout} was replaced by E_y and l'_{1eff} and l'_{2eff} are given by the following expressions:

$$l'_{1eff} = (1.0 + l'_1 - d') + \frac{d'\sqrt{\epsilon_r^2 \sin^2\theta_e + \cos^2\theta_e}}{\epsilon_r} \tag{4.12}$$

$$l'_{2eff} = (1.0 + l'_2 - d') + \frac{d'\sqrt{\epsilon_r^2 \sin^2\theta_e + \cos^2\theta_e}}{\epsilon_r} \tag{4.13}$$

Replacing the derived expression for the line integral (4.11) into (4.8) results in the following simplified expression:

$$\left[E_y l'_{2eff}\Delta\right]_{left} - \left[E_y l'_{1eff}\Delta\right]_{right} - \left[E_z\Delta\right]_{bottom} = -\mu_0\overline{\mu_r}\Delta^2\frac{\partial H_x}{\partial t} - \overline{\rho}\Delta^2 H_x \tag{4.14}$$

The above equation can now be discretized by following the standard procedure of the FDTD method. The final expression for updating the x component of the magnetic field in the distorted contour of Fig. 4.3(a) is:

$$\begin{aligned} H_x^{n+\frac{1}{2}}\left(i,j+\tfrac{1}{2},k+\tfrac{1}{2}\right) &= \frac{1-\frac{\overline{\rho}\Delta t}{2\mu_0\overline{\mu_r}}}{1+\frac{\overline{\rho}\Delta t}{2\mu_0\overline{\mu_r}}}\cdot H_x^{n-\frac{1}{2}}\left(i,j+\tfrac{1}{2},k+\tfrac{1}{2}\right) \\ &+ \frac{\frac{\Delta t}{\mu_0\overline{\mu_r}}\frac{1}{\Delta}}{1+\frac{\overline{\rho}\Delta t}{2\mu_0\overline{\mu_r}}} \\ &\cdot \left[E_y^n\left(i,j+\frac{1}{2},k+1\right)l'_{1eff} - E_y^n\left(i,j+\frac{1}{2},k\right)l'_{2eff}\right. \\ &+ \left. E_z^n\left(i,j,k+\frac{1}{2}\right)\right] \end{aligned} \tag{4.15}$$

where

$$\overline{\mu_r} = 1 + \frac{l'_1 + l'_2}{2} - d' + \mu_r d' \tag{4.16}$$

$$\overline{\rho} = \rho d' \tag{4.17}$$

$$l'_{1eff} = (1.0 + l'_1 - d') + \frac{d'\sqrt{\epsilon_r^2 \sin^2\theta_e + \cos^2\theta_e}}{\epsilon_r} \tag{4.18}$$

$$l'_{2eff} = (1.0 + l'_2 - d') + \frac{d'\sqrt{\epsilon_r^2 \sin^2\theta_e + \cos^2\theta_e}}{\epsilon_r} \tag{4.19}$$

Following a similar procedure, equations for updating the x component of the magnetic field in contours c_2 and c_3 of Fig. 4.3(b) and (c), respectively, can be derived. For contours c_2 and c_3, (4.15) applies also, but with different effective electrical parameters and effective lengths.

The expressions of effective electrical parameters and lengths for updating the x component of the magnetic field in the distorted contour of Fig. 4.3(b) are given by:

$$\overline{\mu_r} = \frac{l'_1 + l'_2}{2} - d' + \mu_r d' \tag{4.20}$$

$$\overline{\rho} = \rho d' \tag{4.21}$$

$$l'_{1eff} = (l'_1 - d') + \frac{d'\sqrt{\epsilon_r^2 \sin^2\theta_e + \cos^2\theta_e}}{\epsilon_r} \tag{4.22}$$

$$l'_{2eff} = (l'_2 - d') + \frac{d'\sqrt{\epsilon_r^2 \sin^2\theta_e + \cos^2\theta_e}}{\epsilon_r} \tag{4.23}$$

The expressions for updating the x component of the magnetic field in the distorted contour of Fig. 4.3(c) are:

$$\overline{\mu_r} = \frac{1.0 + l'_1 + l'_2}{2} - d' + \mu_r d' \tag{4.24}$$

$$\overline{\rho} = \rho d' \tag{4.25}$$

$$l'_{1eff} = (1.0 + l'_1 - d') + \frac{d'\sqrt{\epsilon_r^2 \sin^2\theta_e + \cos^2\theta_e}}{\epsilon_r} \tag{4.26}$$

$$l'_{2eff} \;=\; (l'_2 - d') + \frac{d'\sqrt{\epsilon_r^2 \sin^2\theta_e + \cos^2\theta_e}}{\epsilon_r} \tag{4.27}$$

Slightly different modifications are required for the z component of the magnetic field in the E-plane cross section, compared to those applied for the x component of the magnetic field. Fig. 4.5 illustrates how the grid can be distorted to model the pyramidal horn in the xy plane. The dots in this figure represent the locations of the magnetic field points whose contours are affected by the presence of the antenna conducting surface and composite material. In this case, the distorted contours are normal to the air/material interface. Thus, the boundary condition for E_{yin} and E_{yout} at the air/material interface can be obtained by setting $\theta_e = 0°$ in (4.10). The equations for updating H_z are then obtained by following a similar procedure as the one applied to the x component of magnetic field.

Consider the upper surface of the antenna shown in Fig. 4.5. There are two possible ways that the antenna surface can cut the grid. First, the antenna surface can cut the grid below the magnetic field point and second, above the magnetic field point. These two cases are illustrated in Fig. 4.6. The equations for updating H_z in each case must be modified by applying the contour path method over the distorted contours. Normalizing the distance l_1, shown in Fig. 4.6, with respect to the cell size and applying (3.2) over the distorted contour c_1 results in:

$$\begin{aligned} H_z^{n+\frac{1}{2}}\left(i+\tfrac{1}{2}, j+\tfrac{1}{2}, k\right) \;=\;& \frac{1-\frac{\overline{\rho}\Delta t}{2\mu_0\overline{\overline{\mu_r}}}}{1+\frac{\overline{\rho}\Delta t}{2\mu_0\overline{\overline{\mu_r}}}} \cdot H_z^{n-\frac{1}{2}}\left(i+\tfrac{1}{2}, j+\tfrac{1}{2}, k\right) \\ &+ \frac{\frac{\Delta t}{\mu_0\overline{\overline{\mu_r}}}\frac{1}{\Delta}}{1+\frac{\overline{\rho}\Delta t}{2\mu_0\overline{\overline{\mu_r}}}} \\ &\cdot \left[E_y^n\left(i, j+\frac{1}{2}, k\right) l'_{1eff} - E_y^n\left(i+1, j+\frac{1}{2}, k\right) l'_{1eff}\right. \\ &- \left.E_x^n\left(i+\frac{1}{2}, j, k\right)\right] \end{aligned} \tag{4.28}$$

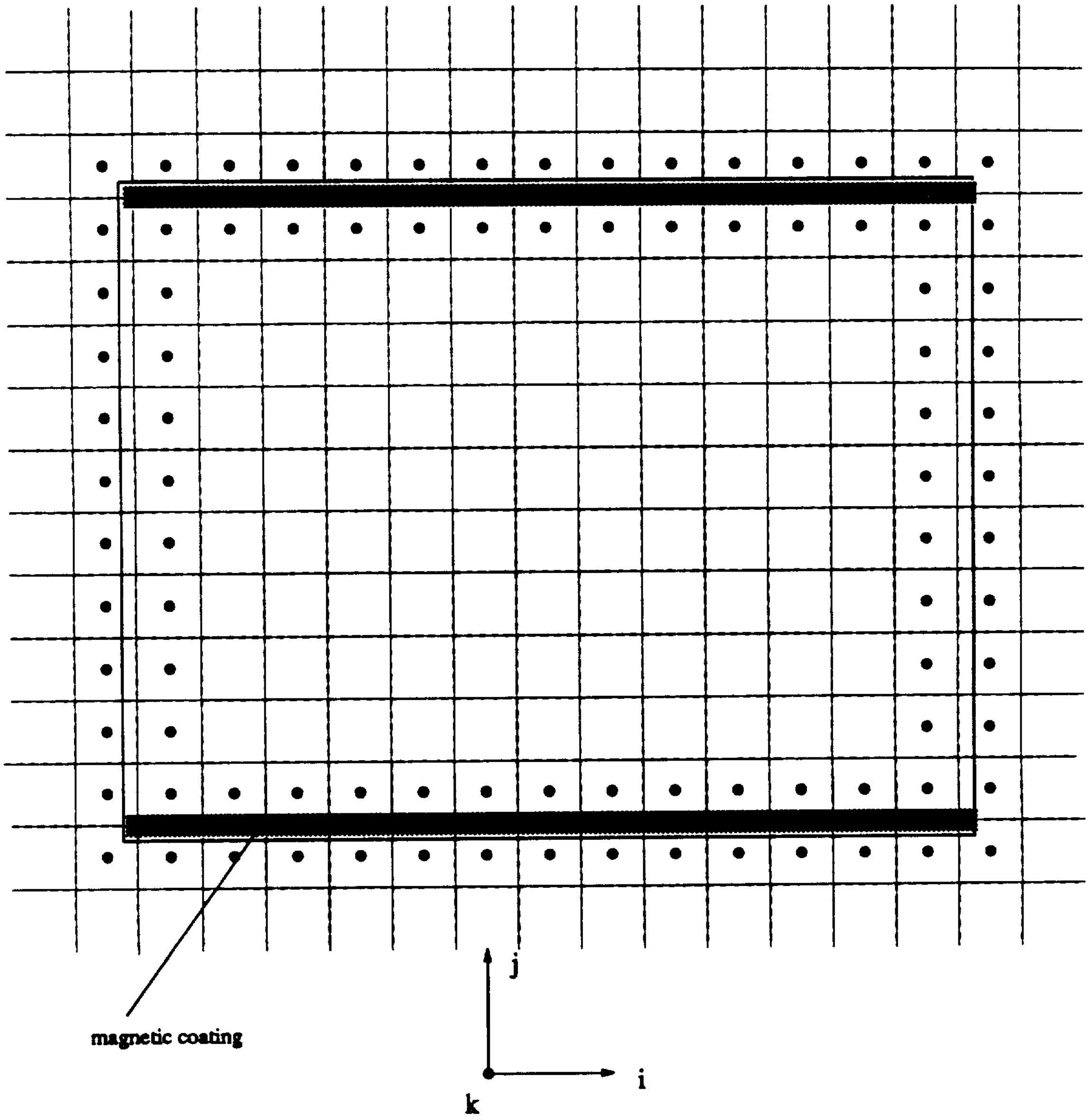

Fig. 4.5: Distorted Faraday's contours at the antenna surface in the xy plane with the presence of composite material.

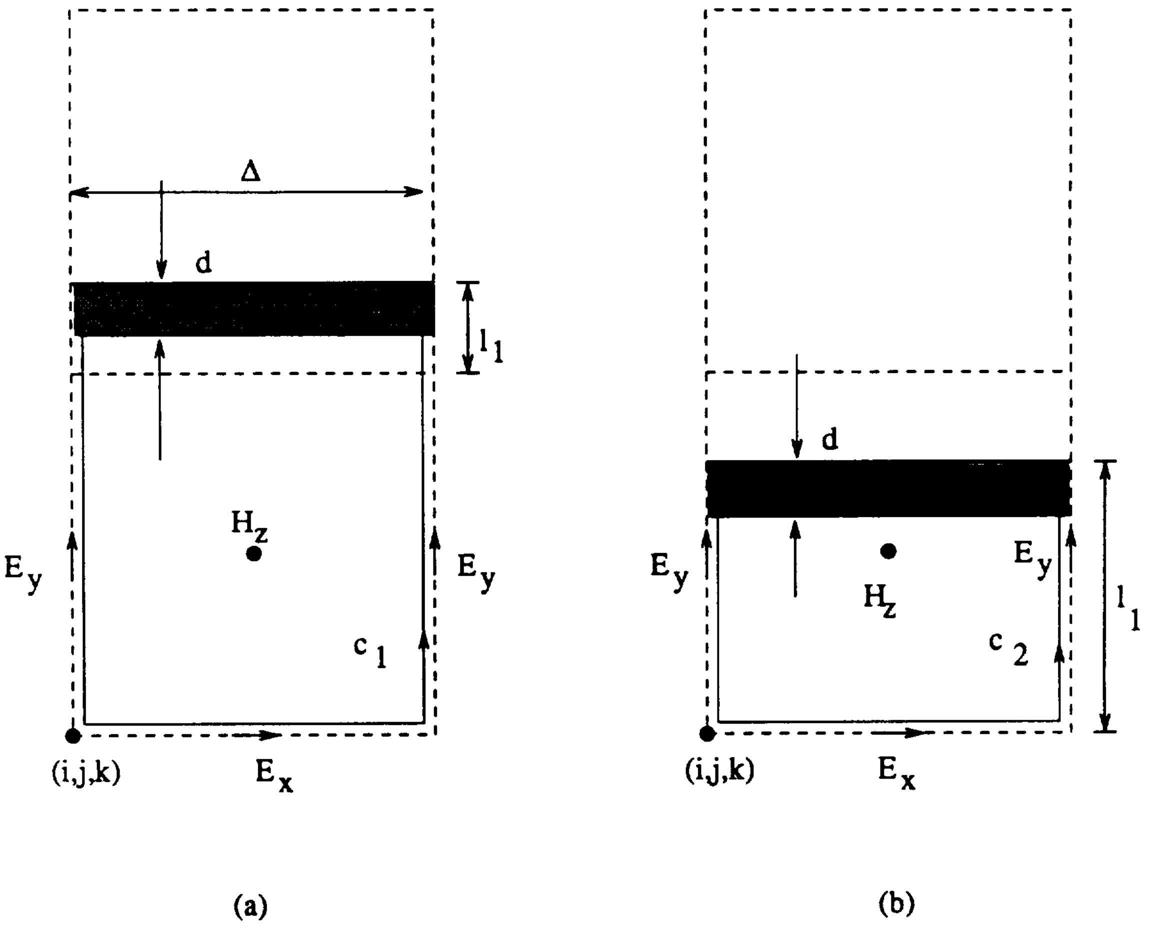

Fig. 4.6: Distorted Faraday's contours used to update H_z near the upper surface of the horn in the xy plane with the presence of composite material.

where

$$\overline{\mu_r} = 1 + l_1' - d' + \mu_r d' \tag{4.29}$$

$$\overline{\rho} = \rho d' \tag{4.30}$$

$$l'_{1eff} = (1 + l_1' - d') + \frac{d'}{\epsilon_r} \tag{4.31}$$

For contour c_2 of Fig. 4.6(b), (4.28) also applies. The effective electrical parameters and effective length in this case are slightly different. The parameters for contour c_2 are

$$\overline{\mu_r} = l_1' - d' + \mu_r d' \tag{4.32}$$

$$\overline{\rho} = \rho d' \tag{4.33}$$

$$l'_{1eff} = (l_1' - d') + \frac{d'}{\epsilon_r} \tag{4.34}$$

The modifications for H_x and H_z were derived based on the assumption that the material thickness was much smaller than the distorted FDTD cells near the antenna surface. By increasing the material thickness but still keeping it less than the FDTD cell some slight modifications must be made. For example, consider the three distorted contour shown in Fig. 4.7. The evaluation of the electric field line integral in this case depends on whether the y-directed electric field is updated using free-space parameters or composite material parameters. If the FDTD updated value for E_y used material parameters the value of E_{yout} in (4.9) is substituted by E_{yin} using the air/material boundary condition (4.10).

In Fig. 4.7(a) the y-directed electric field components on the left and right sides of contour c_1 are updated using free-space parameters. Hence the expressions derived in the previous case with thin material also apply in this case. For Fig. 4.7(b) both

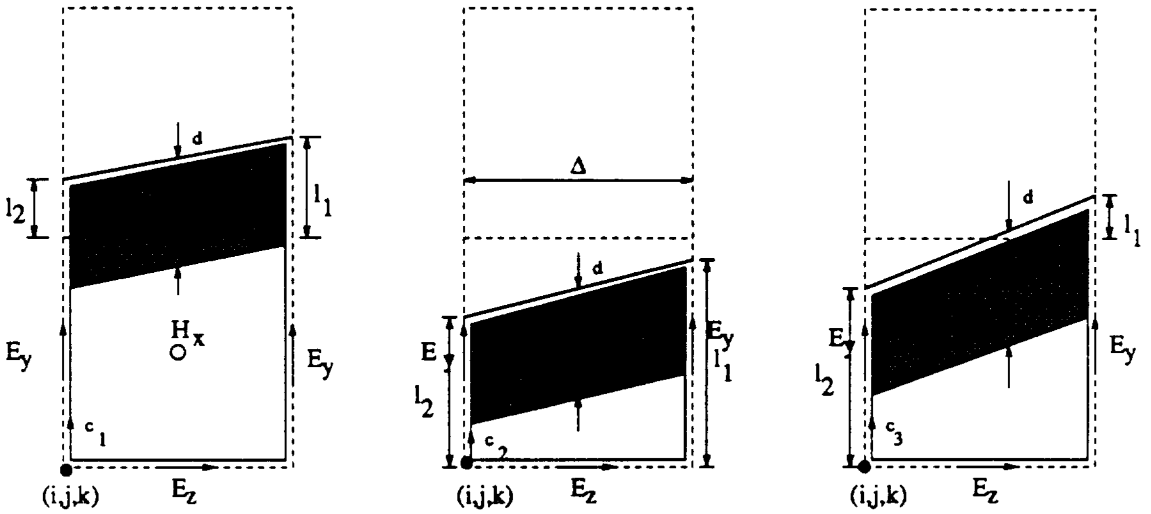

(a) (b) (c)

Fig. 4.7: Distorted Faraday's contours used to update H_x in the presence of a thick section of composite material.

y-directed electric field components are updated using material parameters. Hence, the following expressions for the effective electrical parameters and lengths are used:

$$\overline{\mu_r} = \frac{l_1' + l_2'}{2} - d' + \mu_r d' \tag{4.35}$$

$$\overline{\rho} = \rho d' \tag{4.36}$$

$$l'_{1eff} = (l_1' - d')\frac{\epsilon_r}{\sqrt{\epsilon_r^2 \sin^2\theta_e + \cos^2\theta_e}} + d' \tag{4.37}$$

$$l'_{2eff} = (l_2' - d')\frac{\epsilon_r}{\sqrt{\epsilon_r^2 \sin^2\theta_e + \cos^2\theta_e}} + d' \tag{4.38}$$

For Fig. 4.7(c) the y-directed electric field component on the left side of contour c_3 is updated using material parameters, and the corresponding commponent on the right side using free-space parameters. Hence, the following expressions for the effective electrical parameters and lengths are used:

$$\overline{\mu_r} = \frac{l'_1 + l'_2}{2} - d' + \mu_r d' \tag{4.39}$$

$$\overline{\rho} = \rho d' \tag{4.40}$$

$$l'_{1eff} = (1.0 + l'_1 - d') + \frac{d'\sqrt{\epsilon_r^2 \sin^2\theta_e + \cos^2\theta_e}}{\epsilon_r} \tag{4.41}$$

$$l'_{2eff} = (l'_2 - d')\frac{\epsilon_r}{\sqrt{\epsilon_r^2 \sin^2\theta_e + \cos^2\theta_e}} + d' \tag{4.42}$$

The above modifications constitute the basis of modeling pyramidal horns with composite E-plane walls using the contour path FDTD method. The assumptions made to derive these modified equations were based on the contour path FDTD method. For making possible such an implementation, certain assumptions concerning the field distribution of electric and magnetic fields in the distorted grid were made. Because of these assumptions, the above algorithm would produce accurate results under certain conditions. The limitations of the contour path FDTD method, when applied in the analysis of pyramidal horn antennas with and without composite E-plane walls, is the subject of the following section.

4.3 Limitations of the Contour Path FDTD Method for the Analysis of Radiation by Pyramidal Horns

The flared surface of pyramidal horns was modeled by distorting the FDTD grid near the antenna surface. The integral form of Maxwell's equations was applied over the distorted grid to obtain modified update equations for the magnetic field components within the distorted grid. The field distribution over the distorted grid was assumed constant. This assumption reduces the FDTD method from a second-order accurate method in space to a first-order accurate method. The method, however, remains second-order accurate in time.

The decrease of one order of accuracy in space is expected to have some effect on the accuracy of the computations. The reduced accuracy is expected to affect more the modeling of pyramidal horns with composite E-plane walls. Because of the presence of the composite material (with high dielectric permittivity and magnetic permeability constants and high magnetic loss), the field distribution is expected to vary significantly within the material. However, when the thickness of the composite material is electrically small (less than $\lambda/20$), the constant field assumption over the cell will be more accurate because of the presence of the conducting surface. The slope of normal electric field components, for example, is zero near a perfectly conducting surface.

The implemented contour path FDTD method is valid for the analysis of composite materials with thickness smaller than the FDTD cell. Should the composite material thickness become larger than a unit cell, a different implementation would be required.

Another assumption made in implementing the contour path approach was that the antenna flare angles in the E-plane and H-plane cross sections, were smaller than 45°. With flare angles larger than 45° a more complex algorithm has to be implemented. The three distinctive contours in Fig. 3.4 were identified based on the assumption that the flare angles were less than 45°. More possible contours could be identified, with the angle being larger than 45°. Hence, the algorithm complexity would increase.

4.4 Numerical Results

In this section the developed FDTD computer program is applied for the analysis of pyramidal horn antennas with composite E-plane inner walls. The numerical results are validated by comparing with available experimental data. The effect of composite material on the gain pattern of the antenna is examined and illustrated through a number of computed patterns. Radiation efficiencies and design curves for the variation of the broadside gain loss as a function of material thickness and length are also presented.

The standard 20-dB gain horn antenna is analyzed first. For pattern control purposes sections of ECCOSORB GDS composite material with measured electrical parameters $\epsilon_r = 14.9 - j0.25$ and $\mu_r = 1.55 - j1.45$ at 10 GHz were placed on the inner E-plane walls of the horn as illustrated in Fig. 4.1. The nominal thickness of the composite material section was 30 mil (0.0762cm). The material thickness however, was measured to be t = 33 mil (0.08382cm). Two different material lengths l_m were used for this case. The first case corresponds to $l_m = 2''$ (5.08cm) and the second case to $l_m = 4''$ (10.16cm).

For the FDTD simulations a grid size of 0.1″ was used. The material thickness was about a third of the FDTD grid. The composite material sections influence mainly the E-plane pattern. Thus, only results from the E-plane gain pattern calculation of the coated 20-dB standard gain horn are presented. Fig. 4.8 compares the FDTD computed E-plane gain of the antenna with measurements, when sections of 2″ composite material are used. The agreement between computed and measured results is good. As illustrated in the figure the first sidelobe of the pattern is elliminated. Because of the presence of magnetic material in the inner walls, the broadside antenna gain was reduced by 2.69 dB. The antenna radiation efficiency for this horn was found to be $\eta = 0.76315 \simeq 76.3\%$.

The composite material is more effective in terms of reducing the antenna side lobe levels, when a larger section of composite material is used. Fig. 4.9 compares the FDTD computed results with measurements, when a 4″ section of composite material was used. The agreement between the computed and measured results is good. As illustrated in the figure, the second side lobe is now almost eliminated. The side lobe levels in the back side of the antenna are reduced to levels below -10 dB. The reduction in the broadside antenna gain in this case was close to 5.0 dB. The radiation efficiency was reduced to $\eta = 0.63870 \simeq 63.9\%$. In this case a significant amount of power is dissipated in the lossy magnetic material.

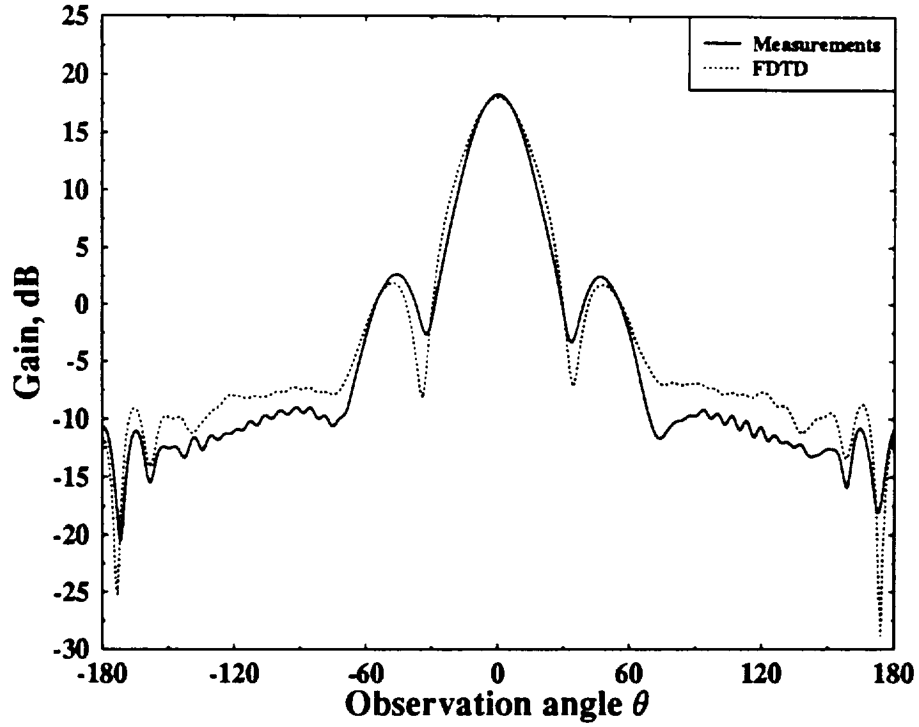

Fig. 4.8: E-plane gain of a 20-dB standard gain pyramidal horn at 10.0 GHz, partially coated with GDS magnetic material ($\epsilon_r = 14.9 - j0.25$ and $\mu_r = 1.55 - j1.45$, t = 33 mil and $l_m = 2''$).

To examine the effect of material thickness and length on the antenna radiation pattern, the broadside gain loss of the 20-dB standard gain horn was calculated for different GDS material thicknesses and lengths. The variation of the broadside antenna gain loss versus the GDS material thickness, for different material lengths, is illustrated in Fig. 4.10. As illustrated in the figure, the broadside antenna gain loss is largest for thickness in the range of 25 - 30 mil and decreases for larger material thickness. For the larger thickness range the gain loss is not strongly influenced by the material length.

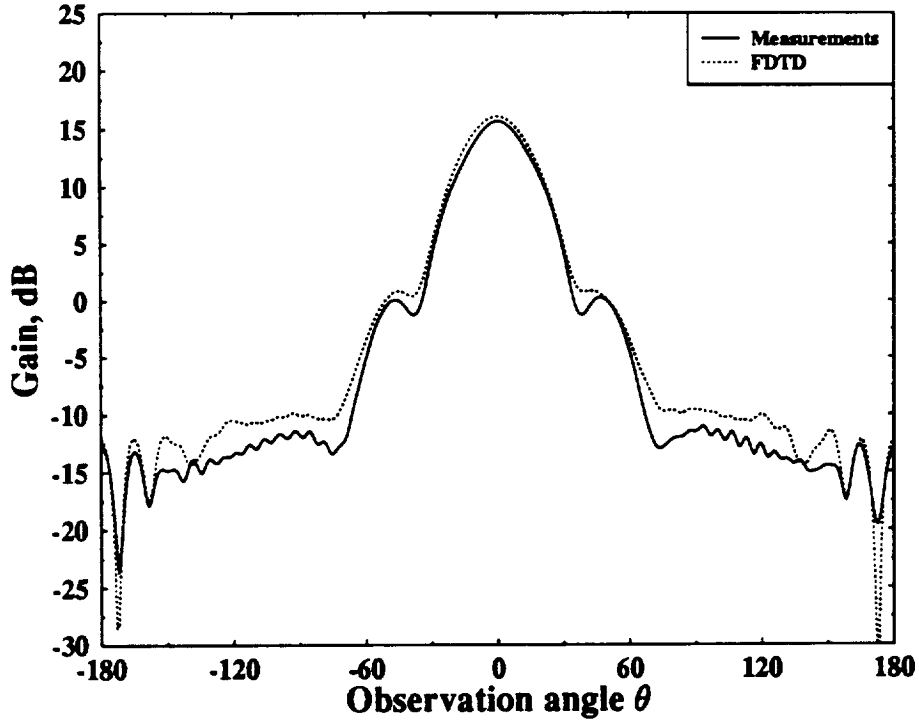

Fig. 4.9: E-plane gain of a 20-dB standard gain pyramidal horn at 10.0 GHz, partially coated with GDS magnetic material ($\epsilon_r = 14.9 - j0.25$ and $\mu_r = 1.55 - j1.45$, t = 33 mil and $l_m = 4''$).

The effectiveness of the thicker material was demonstrated by two examples. Two sections of 33 mil GDS material were combined to form a 66 mil thickness. The 66 mil thick material was then applied to the 20-dB standard gain horn antenna. Two different lengths of material were used in this case. In the first case the material length was 2″ and in the second case 4″.

The computed E-plane gain pattern of the 20-dB standard gain horn antenna, with a 2″ long and 66 mil thick GDS material on the inner E-plane walls, is compared with measurements in Fig. 4.11. As illustrated in the figure, there are some differences between the computed and measured antenna gain patterns. These differences are attributed to the larger thickness of the composite material. With a thicker section of composite material on the antenna inner E-plane walls, the assumption of constant field distribution in the vicinity of the distorted contours is no longer accurate. However, both the FDTD computed results and the measurements demonstrate in this case that the 66 mil thick material case is more effective in shaping the antenna pattern, with out considerable broadside gain loss and reduction in the antenna efficiency. The broadside gain loss for this case was about 2.6 dB, and the antenna efficiency $\eta = 0.70 \simeq 70.0\%$.

The results of the second case with 4″ length and 66 mil GDS material are exhibited in Fig. 4.12. In this case also there are differences between the computed and measured antenna gain patterns. The reduction in the broadside gain for this case was about 2.8 dB, and the antenna efficiency was $\eta = 0.78559 \simeq 78.56\%$.

4.5 Conclusions

The contour path FDTD method was used to analyze pyramidal horns with or without composite E-plane walls. For the metallic horns accurate gain patterns were computed and compared to available measurements. When the inner E-plane walls were coated with lossy materials, for gain pattern control, the contour path FDTD method yields acceptable gain patterns compared to measured ones. For this imple-

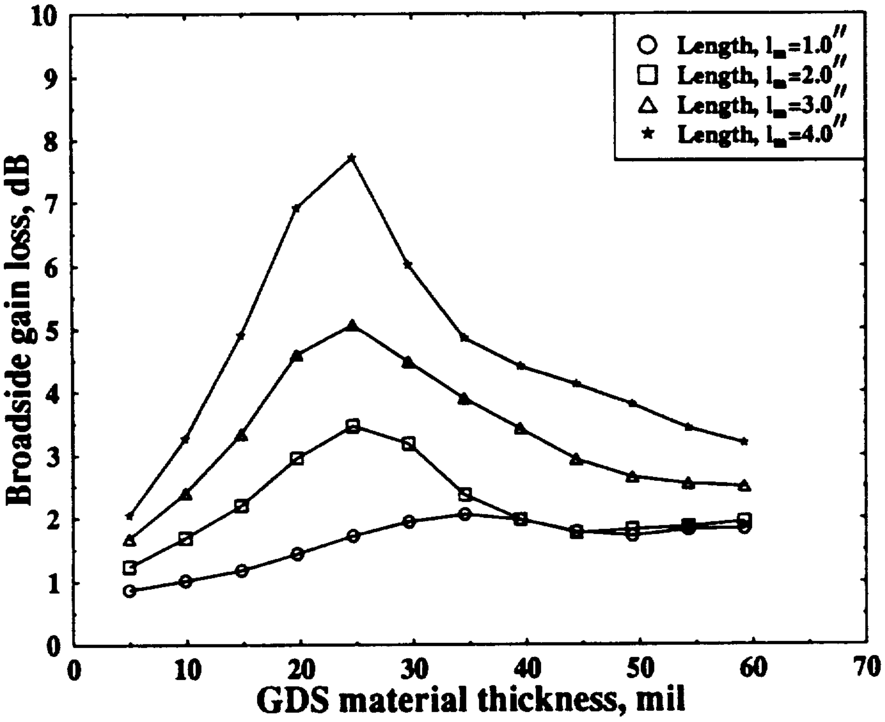

Fig. 4.10: Broadside antenna gain loss of a 20-dB standard gain pyramidal horn at 10.0 GHz, partially coated with GDS magnetic material ($\epsilon_r = 14.9 - j0.25$ and $\mu_r = 1.55 - j1.45$).

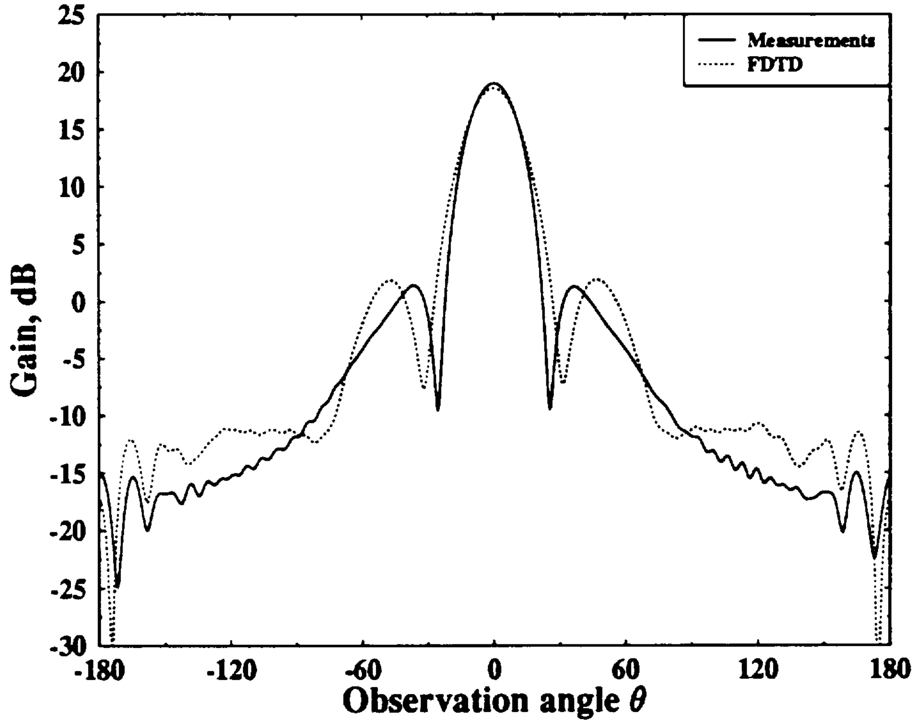

Fig. 4.11: E-plane gain of a 20-dB standard gain pyramidal horn at 10.0 GHz, partially coated with GDS magnetic material ($\epsilon_r = 14.9 - j0.25$ and $\mu_r = 1.55 - j1.45$, t = 66 mil and $l_m = 2''$).

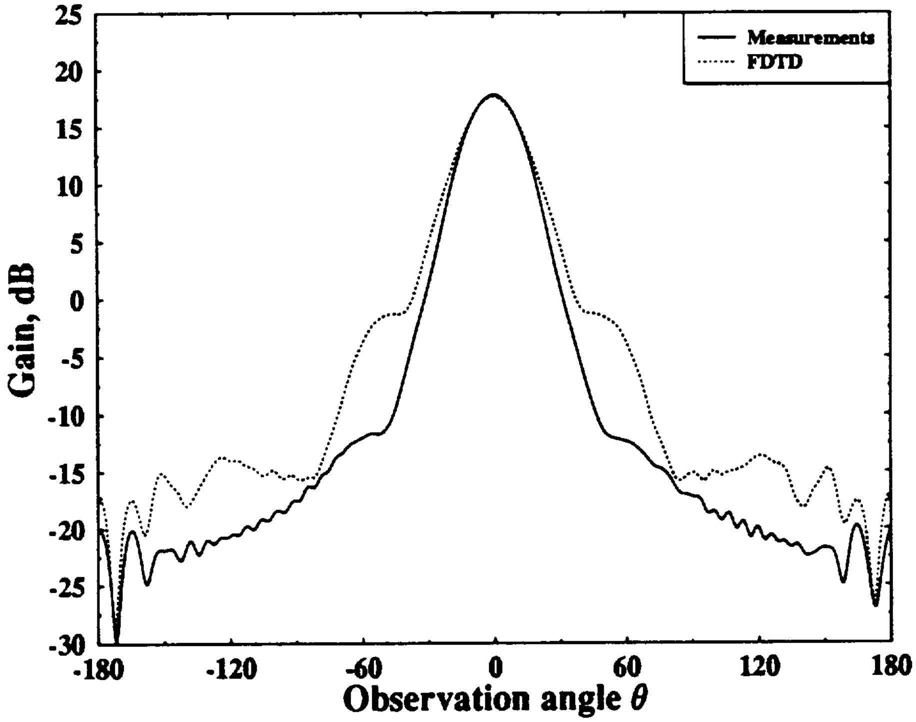

Fig. 4.12: E-plane gain of a 20-dB standard gain pyramidal horn at 10.0 GHz, partially coated with GDS magnetic material ($\epsilon_r = 14.9 - j0.25$ and $\mu_r = 1.55 - j1.45$, t = 66 mil and $l_m = 4''$).

mentation some limitations were imposed.

One approach to design horn antennas with low side lobes and rotationally symmetric patterns is by using lossy materials. This approach was investigated during this project using the FDTD method. Depending on the electrical properties, length and thickness of the material used, nearly symmetric antenna patterns can be designed. Due to the presence of the lossy material, the broadside gain of the horn is reduced by few dB's. However this loss of gain can be minimized by properly selecting the material dimensions, especially the thickness. Design of antenna gain patterns based on the developed computer program is now possible. Such computer-aided designs produce a desired pattern with minimum reduction in the antenna broadside gain.

REFERENCES

[1] A. W. Love, *Electromagnetic Horn Antennas.* IEEE Press Selected Reprint Series: IEEE Press, 1976.

[2] H. Jasik, *Antenna Engineering Handbook.* New York: McGraw-Hill, 1961.

[3] R. S. Elliot, *Antenna Theory and Design.* New York: Prentice Hall, 1981.

[4] C. A. Balanis, *Antenna Theory: Analysis and Design.* New York: John Wiley and Sons, 1982.

[5] P. M. Russo, R. C. Rudduck, and L. J. Peters, "A method for computing E-plane patterns of horn antennas," *IEEE Transactions on Antennas and Propagation*, vol. 13, pp. 219–224, March 1965.

[6] J. S. Yu, C. R. Rudduck, and L. J. Peters, "Comprehensive analysis for E-plane of horn antennas by edge diffraction theory," *IEEE Transactions on Antennas and Propagation*, vol. 14, pp. 138–149, March 1966.

[7] L. Botha and D. A. McNamara, "Examination of antenna patterns of profiled horns using the method of moments," *IEEE Antennas and Propagation Society International Symposium*, vol. I, pp. 293–296, June 1985.

[8] R. F. Harrington, *Field Computation by Moment Methods.* New York: Macmillan Publishing Company, 1968.

[9] J. R. Mautz and R. F. Harrington, "Transmission from a rectangular waveguide into half-space through a rectangular aperture," Technical Report tr-76-5, Contract f19628-c-0047, Airforce Cambridge Res. Lab, May 1976.

[10] R. F. Harrington and J. R. Mautz, "A generalized network formulation for the aperture problems," *IEEE Transactions on Antennas and Propagation*, vol. 24, pp. 870–873, Nov. 1976.

[11] S. N. Sinha, D. K. Mehra, and R. P. Agarwal, "Radiation from a waveguide-backed aperture in an infinite ground plane in the presence of a thin conducting plate," *IEEE Transactions on Antennas and Propagation*, vol. 34, pp. 539–545, Apr. 1986.

[12] J. A. Encinar and J. M. Rebollar, "A hybrid technique for analyzing corrugated and noncorrugated rectangular horns," *IEEE Transactions on Antennas and Propagation*, vol. 34, pp. 961–968, Aug. 1986.

[13] T. Wriedt, K. H. Wolff, F. Arndt, and U. Tucholke, "Rigorous hybrid field theoretic design of stepped rectangular waveguide mode converters including the horn transitions into half-space," *IEEE Transactions on Antennas and Propagation*, vol. 37, pp. 780–790, June 1989.

[14] H. Moheb and L. Shafai, "Applications of integral equations to numerical solution of radiation from horns," *Program and Abstracts of North American Radio Science Meeting in London, Ontario, Canada*, p. 285, June 1991.

[15] D. S. Kats, M. J. Picket-May, A. Taflove, and K. R. Umashankar, "FDTD analysis of electromagnetic radiation from systems containing horn antennas," *IEEE Transactions on Antennas and Propagation*, vol. 39, pp. 1203–1212, Aug. 1991.

[16] P. A. Tirkas and C. A. Balanis, "Finite-difference time-domain method for antenna radiation," *IEEE Transactions on Antennas and Propagation*, vol. 40, pp. 334–340, March 1992.

[17] T. Wang, R. R. Harrington, and J. R. Mautz, "Electromagnetic scattering from and transmission through arbitrary apertures in conducting bodies," *IEEE Transactions on Antennas and Propagation*, vol. 38, pp. 1805–1814, Nov. 1990.

[18] E. Kühn and V. Hombach, "Computer-aided analysis of corrugated horns with axial or ring-loaded radial slots," *Proc. ICAP 83 part 1*, pp. 127–131, 1983.

[19] K. Liu, C. A. Balanis, and G. C. Barber, "Analysis of pyramidal horn antennas using moment methods," *IEEE Transactions on Antennas and Propagation*, Oct. 1993.

[20] J. H. Richmond, "An integral-euation solution for TE radiation and scattering from conducting cylinders," Technical Report, NASA Contractor Rep. CR-2245, National Technical Information Services, Springfield, VA 22161, Apr. 1973.

[21] K. Liu and C. A. Balanis, "Analysis of horn antennas with impedance walls," *Digest of IEEE Antennas and Propagation Society Symposium*, vol. 3, pp. 1184–1187, May 1990.

[22] C. A. Balanis, *Advanced Engineering Electromagnetics.* New York: John Wiley and Sons, 1989.

[23] H. Patzelt and F. Arndt, "Double-plane steps in rectangular waveguides and their application for transformers, irises, and filters," *IEEE Transactions on Microwave Theory and Techniques*, vol. MTT-30, pp. 771–776, May 1982.

[24] S. S. Saad, J. B. Davies, and O. J. Davies, "Computer analysis of gradually tapered waveguide with arbitrary cross-sections," *IEEE Transactions on Microwave Theory and Techniques*, vol. MTT-25, pp. 437–440, May 1977.

[25] F. Sporleder and U. G. Unger, *Waveguide tapers transitions and couplers.* London: Peter Peregrinus Ltd., 1979.

[26] W. A. Huting and K. J. Webb, "Numerical solution of the continuous waveguide transition problem," *IEEE Transactions on Microwave Theory and Techniques*, vol. 37, pp. 1802–1808, Nov. 1989.

[27] H. Flügel and E. Kühn, "Computer-aided analysis and design of circular waveguide tapers," *IEEE Transactions on Microwave Theory and Techniques*, vol. 36, pp. 332–336, 1988.

[28] J. T. Williams, H. J. Delgado, and S. A. Long, "An antenna pattern measurement technique for eliminating the fields scattered from the edges of a finite ground plane," *IEEE Transactions on Antennas and Propagation*, vol. 38, pp. 1815–1822, Nov. 1990.

[29] G. H. Golub and C. F. Van Loan, *Matrix Computations.* John Hopkins University Press, 1989.

[30] F. X. Canning, "Direct solution of the EFIE with half computation," *IEEE Transactions on Antennas and Propagation*, vol. 39, pp. 118–119, Jan. 1991.

[31] R. E. Lawrie and L. Peters, "Modifications of horn antennas for low sidelobe levels," *IEEE Transactions on Antennas and Propagation*, vol. 14, pp. 605–610, Sep. 1966.

[32] C. A. Mentzer and L. Peters, "Pattern analysis of corrugated horn antennas," *IEEE Transactions on Antennas and Propagation*, vol. 24, pp. 304–309, May 1976.

[33] C. M. Knop, , E. L. Osterlag, E. L. Matz, and Y. B. Cheng, "Reflector-type microwave antennas with absorber lined conical feeds," *U.S. Patent 4,410,892*, Oct. 1983.

[34] S. Rodrigues, P. Monahan, and K. G. Nair, "A strip-loaded feed-horn antenna," *IEEE Microwave Guided Wave Letters*, vol. 1, pp. 318–319, Nov. 1991.

[35] C. S. Lee, S. W. Lee, and S. L. Chuang, "Normal modes in an overmoded circular waveguide coated with lossy material," *IEEE Transactions on Microwave Theory and Techniques*, vol. 34, pp. 773–785, July 1986.

[36] C. S. Lee, S. W. Lee, and D. W. Justice, "A simple circular-polarized antenna: Circular waveguide horn with lossy magnetic material," *IEEE Transactions on Antennas and Propagation*, vol. 36, pp. 297–300, Nov. 1990.

[37] C. M. Knop, Y. B. Cheng, and E. L. Ostertag, "An absorber-wall parallel-plate waveguide," *IEEE Transactions on Microwave Theory and Techniques*, vol. 34, pp. 761–766, July 1986.

[38] C. M. Knop, Y. B. Cheng, and E. L. Ostertag, "On the fields in a conical horn having arbitrary wall impedance," *IEEE Transactions on Antennas and Propagation*, vol. 34, pp. 1092–1098, Sep. 1986.

[39] J. J. H. Wang, V. K. Trip, and R. P. Zimmer, "Magnetically coated horn for low sidelobes and low cross-polarization," *IEE Proceedings*, vol. 136, pp. 132–138, Apr. 1989.

[40] J. J. H. Wang, V. K. Trip, and J. E. Tehan, "The magnetically coated conducting surface as a dual conductor and its application to antennas and microwaves," *IEEE Transactions on Antennas and Propagation*, vol. 38, pp. 1069–1077, July 1990.

[41] S. I. Ghobrial and H. R. Sharobim, "Radiation patterns of paraboloidal reflector fed by a pyramidal horn with lossy walls," *IEEE Transactions on Antennas and Propagation*, vol. 37, pp. 1316–1317, Oct. 1989.

[42] K. Liu, C. A. Balanis, and G. C. Barber, "Low-loss material coating for horn antenna beam shaping," *Digest of IEEE Antennas and Propagation Society Symposium*, vol. 3, pp. 1664–1667, June 1991.

[43] A. Taflove, K. Umashankar, B. Beker, F. Harfoush, and K. Yee, "Detailed FD-TD analysis of electromagnetic fields penetrating narrow slots and lapped joints in thick conducting screens," *IEEE Transactions on Antennas and Propagation*, vol. 36, pp. 247-257, Feb. 1988.

[44] T. G. Jurgens, A. Taflove, K. R. Umashankar, and T. G. Moore, "Finite-difference time-domain modeling of curved surfaces," *IEEE Transactions on Antennas and Propagation*, vol. 40, pp. 357–366, Apr. 1992.

[45] A. C. Cangellaris, L. Chung-Chi, and K. K. Mei, "Point-matched time domain finite element methods for electromagnetic radiation and scattering," *IEEE Transactions on Antennas and Propagation*, vol. 35, pp. 1160–1173, Oct. 1987.

[46] E. H. Newman and M. R. Schrote, "An open surface integral formulation for electromagnetic scattering by material plates," *IEEE Transactions on Antennas and Propagation*, vol. 32, pp. 672–678, July 1984.

[47] X. Min, W. Sun, W. Gesang, and K. M. Chen, "An efficient formulation to determine the scattering characteristics of a conducting body with thin magnetic coatings," *IEEE Transactions on Antennas and Propagation*, vol. 39, pp. 448–454, Apr. 1991.

[48] J. M. Jin and V. V. Liepa, "Application of hybrid finite element method to electromagnetic scattering from coated cylinders," *IEEE Transactions on Antennas and Propagation*, vol. 36, pp. 43–50, Jan. 1988.

[49] J. D. Collins, J. L. Volakis, and J. M. Jin, "A combined finite element-boundary integral formulation for solution of two-dimensional scattering problems via CGFFT," *IEEE Transactions on Antennas and Propagation*, vol. 38, pp. 1852–1858, Nov. 1990.

[50] A. Taflove and M. E. Brodwin, "Numerical solution of steady-state electromagnetic scattering problems using the time-dependent Maxwell's equations," *IEEE Transactions on Microwave Theory and Techniques*, vol. 23, pp. 623–630, Aug. 1975.

[51] P. A. Tirkas and K. R. Demarest, "Modeling of thin dielectric structures using the finite-difference time-domain technique," *IEEE Transactions on Antennas and Propagation*, vol. 39, pp. 1338–1344, Sep. 1991.

[52] J. G. Maloney and G. S. Smith, "The efficient modeling of thin material sheets in the finite-difference time-domain (FDTD) method," *IEEE Transactions on Antennas and Propagation*, vol. 40, pp. 323–330, March 1992.

APPENDIX A

EVALUATION OF THE IMPEDANCE MATRIX ELEMENTS IN MOMENT METHOD

The electric fields due to surface electric and magnetic current distribution needed in (1.48) and (1.49) can be written as

$$\mathbf{E}(\mathbf{J}) = -j\beta\eta\int_{S'}(\mathbf{J}(\mathbf{s}') + \frac{1}{\beta^2}\nabla\nabla'\cdot\mathbf{J}(\mathbf{s}'))\Phi ds' \tag{A.1}$$

$$\mathbf{E}(\mathbf{M}) = -\int_{S'}\mathbf{M}(s')\times\nabla\Phi ds' \tag{A.2}$$

where primed coordinate represents the source coordinate and $\Phi = e^{-j\beta R}/4\pi R$ is the free-space Green's function; $\mathbf{J}(s')$ and $\mathbf{M}(s')$ are surface electric and magnetic current density on S', respectively. Substituting (A.1) and (A.2) into (1.48) and (1.49), respectively, using the current continuity condition, the impedance matrix elements can be expressed in the form of

$$Z_{ij} = j\beta\int_{S_i}\int_{S_j'}[(\mathbf{P}_i^J\cdot\mathbf{P}_j^J) - \frac{1}{\beta^2}(\nabla\cdot\mathbf{P}_i^J)(\nabla'\cdot\mathbf{P}_j^J)]\Phi ds_j' ds_i \tag{A.3}$$

$$Q_{kl} = \beta\int_{S_k}\int_{S_l'}\frac{\mathbf{n}\cdot\mathbf{R}}{R^2}P_k^J(s_k)P_l^M(s_l')(1+j\beta R)\Phi ds_l' ds_k \tag{A.4}$$

where $\mathbf{n}$ is the unit directional vector of $(\mathbf{P}_k^J\times\mathbf{P}_l^M)$. Evaluations of (A.3) and (A.4) can be efficiently carried out by using Taylor's expansions of the kernel functions Φ and $e^{-j\beta R}$ at the center of the two patches and analytical integrations can be found for individual terms of the Taylor's expansions. Therefore, only one of the surface integrals needs to be evaluated numerically.